IN MEMORIAM ACADEMICIAN SVEATOSLAV A. MOSKALENKO

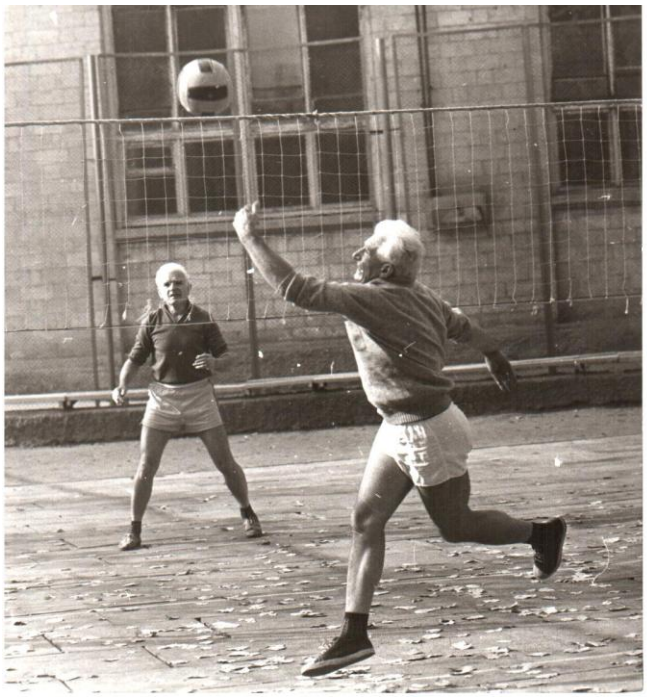

Life is short and science is long.
Lucian of Samosata

I do not know any other pleasure than to cognize.
Francesco Petrarca

Moskalenko Sveatoslav Anatol (Anatolievich) is the physicist of note, doctor habilitate in physico-mathematical sciences, professor, and academician kept in the memory and hearts of many men of science of the world as a talented scientist, the founder—together with his twin brother—of the school of theoretical physics in Moldova, teacher, administrator, head of Theoretical Physics Department of the Institute of Applied Physics in the Chisinau city, Republic of Moldova.

Moskalenko Sveatoslav (26.09.1928–29.01.2022) was born in the village Bravicea from the Orhei district of the Bessarabia, at that time being a part of Romania. His father—Moskalenko Anatoly Emelianovich—was a recording official. He was born in 1900; presumably he served in the ranks of the White Army; he was repressed after joining Bessarabia to the USSR in 1940 and died in the concentration camp in Kotlas in 1942. Mother—Moskalenko Natalya Karabetovna (Karpovna)—was a manager's daughter, housewife, seamstress (1906–1999).

Sveatoslav and his brother Vsevolod Moskalenko successfully studied and finished school in Orhei city. In 1946 they entered the first year of the Faculty of Physics and Mathematics of Moldova State University. Yuliya Stanislavovna Boyarskaya, who later became the wife of Sveatoslav, entered the same course.

Moskalenko S.A. was the author of numerous scientific works. He worked in the field of exciton and biexciton physics. His best-known monographs in the international scientific community are as follows: S.A. Moskalenko and D.W. Snoke, Bose-Einstein Condensation of

Excitons and Biexcitons and Coherent Nonlinear Optics with Excitons, Cambridge University Press, Cambridge, New York, 415, 2000; S.A. Moskalenko, Introduction in the theory of high density excitons, Chisinau, Shtiintsa, 304, 1983 (in Russian). They were expected and highly appreciated by the specialists. The writings by M.S.A. have left a significant trace in the history of scientific thought and have immortalized the memory of the genius of physics among the geniuses who glorify Moldova.

The physicist by education, he possessed human qualities and streaks that attracted people to him and allowed him to solve complex problems of current importance together in the laboratory entrusted to him.

He was a kind person. This is not about family relationships. Yes, he loved and kindly treated his wife, daughter, and son and adored grandchildren. We are talking about kindness in a wide, universal sense common to all mankind. How many young talents has he helped to take a step on the professional road and find their own direction!

Being the head of the Department of Theoretical Physics, he always met both young and experienced foreign scientists, personally took care of their accomplishment, if time allowed, showed them the city, the sights of Moldova.

Sveatoslav Moskalenko was not an ordinary chief: he always skilfully rallied the team he led, planned the work for the future, and introduced new things into the activities of the laboratory. Weekly seminars, reports popularizing the science, and summer schools were always interesting.

In this environment, the training of students, laboratory staff, and future philosophy doctors and doctors habilitate took place. Sveatoslav Anatol introduced meetings-seminars of the collective, where the results of work for a certain period were summed up and unresolved issues were clarified, conference reports were analysed, and future trends were outlined.

The post-Soviet time proved difficult for the department: the premises were not heated, the experimental part of the laboratory was not being equipped with modern equipment, the sending of young people to study in special educational institutions in Russia and Ukraine stopped. Participation of the laboratory in the international projects contributed to its further development, and the laboratory staff was able to continue doing what they love. Sveatoslav Moskalenko, through the leadership, sought to increase the subsidy for the laboratory and personal bonuses to salaries.

The laboratory continued and is now continuing its activities!

According to Anton Kiselyov's reminiscences, about his trip to Russia and about Sveatoslav Anatol's trip to Tiraspol, accompanying the following story with his own poem (dated August 8, 2018, in the original).

Every summer I came to my native Chisinau; at the end of August I travelled by train to St. Petersburg. Grandfather walked me to the train and handed a box of fruit and other delicious food to me. Of course, he went into the carriage and sat on an empty berth. I studied at the magistracy of the Faculty of Physics, and, of course, my grandfather was very interested in what exactly I was doing. The conductor repeated several times that the train was about to leave, but my grandfather continued to ask me about the spectrum of the helium atom. At that time, there were no neighbours in the compartment: apparently, they were supposed to call in Bendery or Tiraspol (that year the train did not drive all over Transnistria through Balti and Ocnita). That's why the conductor mistook grandfather for a passenger and did not try to send on his way out of the carriage. I did not remember exactly when the train was leaving, and I did not have time to warn my grandfather either. The train slowly drove off the platform.

Grandfather soon took notice of this and asked me what it meant. I told him that we were

leaving. He was a little bit surprised, but then he asked me about quantum numbers. I began to answer something, at the same time painfully thinking, what I should do now. Thank God, I found the phone number of my grandfather's closest colleague, Piotr Ivanovich Khadzhi, who worked in both Chisinau and Tiraspol. I, having left my grandfather in the compartment, jumped out with the phone to the vestibule train and called up Piotr Ivanovich. He got in Chisinau, but said that he would now call to Tiraspol and try to think something out. I came back, continued the conversation I had interrupted with my grandfather, and in half an hour more Piotr Ivanovich called me and cheerfully announced: "The physicists-friends of mine will meet Sveatoslav Anatolievich at the Tiraspol railway station". Soon I told my grandfather that we were approaching Tiraspol, and he needed to get off there. It was already close to midnight. "When will I be back?" – asked my grandfather. "Probably tomorrow", – I answered. After accompanying him to the vestibule, I saw several people approaching the carriage, one of whom declared: "Physicists of Pridnestrovie in my person welcome the academician from Chisinau! We are very glad that you have decided to come to us." Grandfather was obviously confused, but they took him by the hands and led him somewhere—apparently, to someone's car, since public transport did not run so late.

И 90 лет прошло...

Проходит день, проходит год,
Он на работу всё идёт.

Неспешно двери отворяет,
Неспешно почту проверяет.

Глядит на записи свои,
Готовит новые статьи.

Глаза смыкает, видит сон,
Где всех главней биэкситон.

Кто как несёт земное бремя,
Ему гласит программа "Время".

Торшер бумаги освещает,
Он снова пишет, исправляет.

Почти все близкие ушли:
Нет сына, брата, нет Хаджи...

Проходит день, проходит год,
Он на работу всё идёт.

The time moves forward, and the plans and dreams by Sveatoslav Moskalenko will always inspire his continuers and followers, will awaken undertakings and aspirations for accomplishments, and this will be the best memory of this great scientist, teacher, and leader.

I 90 let proshlo...

Prokhodit den', prokhodit god,
On na rabotu vse idet.

Nespeshno dveri otvoryaet,
Nespeshno pochtu proveryaet.

Glyadit na zapisi svoi,
Gotovit novye stat'i.

Glaza smykaet, vidit son,
Gde vsekh glavnei bieksiton.

Kto kak neset zemnoe bremya,
Emu glasit programma “Vremya”.

Torsher bumagi osveshchaet,
On snova pishet, ispravlyaet.

Pochti vse blizkie ushli:
Net syna, brata, net Khadzhi...

Prokhodit den', prokhodit god,
On na rabotu vse idet.

I.V. Podlesny[1] and A.A. Kiselyov[2]

[1]*Institute of Applied Physics, str. Academiei 5, Chisinau, MD-2028 Republic of Moldova*
[2]*State University of Civil Aviation, ul. Pilotov 38, St. Petersburg, 196210, Russia*

IN MEMORIAM OF PROFESSOR TEODOR MUNTEANU

(15 August 1942 – 22 May 2022)

December 17, 2018 was my first day as a trainee researcher in the Cryogenics laboratory at Ghițu Institute of Microelectronics and Nanotechnologies. I was greeted by a gray-haired man with a quiet voice and a cordial look; he was calm and benevolent. That man was university professor, doctor habilitated Teodor Maftei Munteanu. Our first discussion about science began with his question, “What is your subject of research, young man?” I proudly answered, “It is superconductivity!!!” Whereat he exclaimed, “What a coincidence, I also study superconductivity, except that I do it at a theoretical level, rather than at a practical level!" From that discussion, I understood that I was talking to a person who was highly skilled in the fundamentals of crystallography, superconductivity of bicrystals, magnetoresistive effects, semiconductor–semimetal electronic phase transitions, quantum oscillations, and thermomagnetic effects. In addition, he told me about the growth of glass-insulated thin wires and magnetothermoelectromotive oscillations in electron-irradiated AsSb alloys in detail.

Teodor Maftei Munteanu was born on August 15, 1942 in Hârbovăț commune of the Anenii Noi district of the Republic of Moldova. He attended primary school in his native village and continued his studies at Pedagogical Institute in Tiraspol (1958–1964).

He defended his doctorate thesis in 1972 and became a doctor of physics and mathematics in 1987. After that, on June 21, 2001, the didactic title of university professor was conferred to

him.

He contributed to the writing of 250 scientific papers; two of the books were published here, in the Republic of Moldova. He participated with 96 reports at various international scientific conferences and symposiums, such as International Conference on Low-Temperature Physics, European Conference on Physics of Magnetism, and Balkan Physics Conference.

He cooperated with many institutions from the former Soviet Union, Poland, Romania, Bulgaria, Germany, and other countries.

A special field of activities of Teodor Maftei Munteanu was his research at the International Laboratory of Low Temperatures and Strong Fields in Wroclaw, where researchers used to study the behavior of semimetals, narrow-band-gap semiconductors, and superconductors at low temperatures and in extremely strong stationary magnetic fields of 18 T at a pulse of up to 45 T.

Teodor Maftei Munteanu made a quite interesting discovery: he discovered two superconducting phases at nanometric bicrystalline interfaces, which do not exhibit superconductivity under normal conditions. He emphasized that, at these interfaces, superconductivity coexists with weak ferromagnetism.

He was a scientific supervisor of six postgraduate students who defended their doctorate theses.

He worked as editor-in-chief of the Encyclopedia at the Academy of Sciences of the Republic of Moldova in the period of 1972–1974; after that, he was a senior researcher, an interim head of laboratory, and later—in 1986–2004—head of the Laboratory of Physics of Semimetals of Institute of Applied Physics of the Academy of Sciences of the Republic of Moldova. Since 2004, he was the head of the Transport Phenomena Laboratory of the International Laboratory of Superconductivity and Solid State Electronics.

By decisions of the Government of the Republic of Moldova no. 53 of January 27, 1999 and no. 1437 of November 11, 2002, Teodor Maftei Munteanu was appointed as a vice-president of the Higher Attestation Commission of the Republic of Moldova. Since 2005, he was the head of the General Attestation Directorate of the National Council for Accreditation and Attestation.

On March, 2002, by order of the Government of the Republic of Moldova no. 22, the degree of qualification of public official—Counselor of State of rank I, class III—was conferred to Teodor Maftei Munteanu.

In 2012, Teodor Maftei Munteanu was awarded the Glory of Labor order for outstanding merits in research.

He was a personality worthy of admiration and scientific honors.

Vladimir Boian
Ghitu Institute of Electronic Engineering and Nanotechnologies, Chisinau, MD-2028 Republic of Moldova

IN MEMORIAM DOCTOR EFIM ALEKSEEVICH ZASAVITSKII

(19 September 1958 – 14 April 2022)

On April 14, 2022, at the age of 63, after a long severe illness, Efim Alekseevich Zasavitskii—a wonderful person, scientist (Laureate of the State Prizes of the Republic of Moldova), Doctor of Physics and Mathematics—passed away.

Efim Alekseevich Zasavitsky, being a versatile researcher and talented administrator, was one of the key persons in the team of Academician Valerii Kantser, which worked on INTAS projects on low-dimensional A^4B^6 structures for thermoelectric converters in the late 1990s and the early 2000s.

Academician Valerii Kantser and dr. Efim Zasavitsky

Later, he joined the activities on STCU projects on studying the atomically precise design of complex oxide materials (2011) and developing thermochromic coatings for energy efficient windows (2017). However, the real subject of his interest was the construction of a laboratory aerodynamic full-size rocket system for studying the efficiency of antihail rocket agents. This system, which was unique not only for Moldova, but also for the region, met the urgent needs of the economy of Moldova. The system was used not only to accomplish the objectives of a large number of important economic projects, in particular, with partners from Bulgaria, Russia, Romania, and Ukraine, but also to conduct research activities and experiments, in particular, within the framework of the STCU project led by Dr. Zasavitskii.

Significant achievements in increasing the efficiency of antihail protection in the country and in improving the antihail protection methodology at the Special Service for Active Influences on Hydrometeorological Processes of the Republic of Moldova are associated with the name of Efim Alekseevich Zasavitskii.

Efim Alekseevich was one of the originators and developers of a specialized laboratory on testing ice-forming reagents at blowing speeds of their generators (antihail rockets, etc.) under

conditions similar to real atmospheric conditions at Ghitu Institute of Electronic Engineering and Nanotechnology. Up to the present, the results obtained are unique in terms of practice and research. The results were published in world-class international journals and reported at many conferences.

Efim Zasavitsky among participants of a conference

There are few laboratories of this type on the European continent; it is not by chance that the organized laboratory has gained international fame. Representatives of many countries, where activities on active influences aimed at suppressing hailstorms and providing additional precipitation are conducted, apply to the Institute for testing their reagents for active influences.

Specialized laboratory at Gitsu Institute of Electronic Engineering and Nanotechnologies

Efim Alekseevich left good memories behind for all the employees of the Institute for many years. His special friend was Dmitrii Karagenov. They have carried their friendship through decades. His close friend and colleague Dmitrii Karagenov shared his memories of their friendship.

We have known Efim Zasavitskii since 1984. In those years, he was a young postgraduate student; he began his career in the scientific and experimental laboratory for studying the properties of semiconductor compounds in the field of ultralow temperatures at Institute of Applied Physics of the Academy of Sciences of the MSSR. In his research work, he proved himself to be a scrupulous and thoughtful researcher with an excellent university theoretical background, who deeply understood the subject of the study.

In solving a problem, Efim Zasavitskii found extraordinary solutions using the latest scientific achievements in the field of semiconductor compounds. His special personal characteristic was the ability to listen to an alternative opinion of his colleagues, quietly discuss everything, and make a right decision. In personal relationships and in everyday life, he always acted honestly and decently.

In my memory, he remains a good comrade and true friend.

He behaved inconspicuously and never showed off. He wholeheartedly shared his experience and knowledge with his friends and unobtrusively rendered his opinion.

The staff of our Institute and the staff of the Special Service for Active Influences on Hydrometeorological Processes of the Republic of Moldova believe that the continuation of activities of the specialized laboratory in the organization of which Efim Zasavitskii took an active part will be the best memory of Efim Alekseevich.

Cherished memory to dear friend, scientist, and excellent person!

Tatiana Gutul[1],
Vladimir Feodorov[1]

[1]*Ghitu Institute of Electronic Engineering and Nanotechnologies, Chisinau, MD-2028 Republic of Moldova*

LUMINESCENCE OF YTTRIUM TANTALATE DOUBLY ACTIVATED WITH EUROPIUM AND TERBIUM UNDER X-RAY AND ELECTRON BEAM EXCITATIONS

Mihail Nazarov[1] and Maria Zamoryanskaya[2]

[1]Institute of Applied Physics, str. Academiei 5, Chisinau, MD-2028 Republic of Moldova
[2]Ioffe Physical-Technical Institute, ul. Politekhnicheskaya 26, St-Petersburg, 194021 Russia

E-mail: mvnazarov@mail.ru

(Received January 28, 2022)

https://doi.org/10.53081/mjps.2022.21-1.01

Abstract

This paper reports the luminescence spectra of $YTaO_4$ activated with rare-earth ions, such as Eu^{3+} and Tb^{3+}. The effect of these rare-earth ions on the luminescence of yttrium tantalate phosphors is studied. The luminescent properties are studied under X-ray and electron beam excitations. It is found that, under these excitations, the emission centers of the rare-earth activators (Eu^{3+}, Tb^{3+}) efficiently contribute to the overall luminescence. Color cathodoluminescence images clearly show the dependence of chromaticity on the different activators. These rare-earth activated phosphors exhibiting various luminescence chromaticities are promising materials for optoelectronic applications and for X-ray intensifying screens in medical diagnosis, because they provide a broad variation of visible photoluminescence from blue to red.

Keywords: $YTaO_4$, $YTaO_4$:Eu^{3+},Tb^{3+}, cathodoluminescence.

Rezumat

În această lucrare sunt prezentate spectrele de luminescență ale cristalelor de $YTaO_4$ activate cu ioni de pământuri rare, cum ar fi Eu^{3+} și Tb^{3+}. A fost investigată influența acestor ioni de pământuri rare asupra luminescenței fosforilor de tantalat de ytriu. Proprietățile luminescente au fost studiate la escitare cu raze X și fascicule de electroni. S-a constatat că centrele de emisie ale activatorilor de pământuri rare (Eu^{3+}, Tb^{3+}) contribuie eficient la luminescența generală. Imaginile de catodolumeniscență color au arătat în mod clar dependența cromaticității de diferiți activatori. Datorită cromaticităților diferite de luminescență, acești fosfori activați cu pământuri rare sunt materiale promițătoare pentru aplicații optoelectronice, precum și pentru ecranele de intensificare a razelor X în diagnosticul medical, oferind o variație largă a fotoluminescenței vizibile de la albastru până la roșu.

Cuvinte cheie : $YTaO_4$, $YTaO_4$:Eu^{3+},Tb^{3+}, catodoluminiscență.

1. Introduction

Yttrium tantalate phosphors are of large interest for the manufacture of some medical imaging detectors, especially for conventional radiographic cassettes [1, 2]. These luminescent materials exhibit good X-ray absorption and emit in the ultraviolet and blue region of the electromagnetic spectrum [3]. Yttrium tantalate has three crystal structures: high-temperature tetragonal (scheelite, T-structure), low-temperature monoclinic (fergusonite, M-structure), and another monoclinic form, which is referred to as M' and can be synthesized at lower temperatures (below 1400ºC) [1, 4]. In the M'-$YTaO_4$ structure, tantalum atoms are in a distorted octahedral coordination with six Ta–O bonds, whereas in M-$YTaO_4$ tantalum atoms are in a tetrahedral coordination. In addition, the unit cell volume of the M' phase is approximately two times smaller than that of the M phase, and the average Ta–O distances are relatively smaller [5, 6]. As a result, the M' phase presents a more efficient charge transfer process that determines superior luminescent emission.

In this paper, rare-earth activators Eu^{3+} and Tb^{3+} were simultaneously incorporated into M'-$YTaO_4$ structures. The luminescent properties of these phosphors under electron beam and X-ray excitation were studied. Color cathodoluminescence (CCL) images clearly showed the dependence of chromaticity on the different activators.

2. Experimental

2.1. Sample preparation

Samples of $YTaO_4$ doubly activated with Eu^{3+} and Tb^{3+} were prepared by the solid-state reaction method from a homogeneous mixture consisting of Y_2O_3 and Ta_2O_5. Europium oxide Eu_2O_3 and/or terbium oxide Tb_4O_7 were used in the activator system and Na_2SO_4 as a flux. The mixtures were homogenized in a ball mill in an acetone medium and dried at 70°C. The phosphor samples were baked at 1200°C for 4 h and slowly cooled to room temperature. Finally, the samples were water washed, dried, and then sieved.

2.2. X-ray excited luminescence (XEL) measurements

To study luminescence under X-ray excitation, the powder phosphor samples were illuminated with broadband X-ray radiation. Figure 1 shows that the samples were placed at a position of 45^o from the incident X-rays and close to the exit of the Be X-ray window to minimize the loss of X-ray flux by scattering in air. Since the luminescence light spread out to all directions, a collimating lens system was used to effectively collect the light. The emission spectrum was recorded with a spectrometer (SM240, Spectral Products) in a wavelength range of 200–1200 nm.

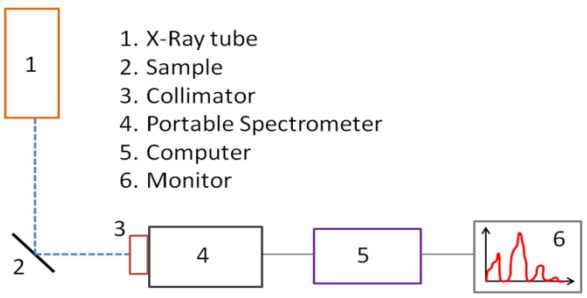

Fig. 1. Schematic diagram of the experimental configuration to study the luminescence of phosphors under X-ray excitation.

2.3. Cathodoluminescence (CL) studies

Sample characterization in CL under electron beam excitation was performed using a special spectrometer [7] installed on the optical microscope port of a standard Camebax electron microprobe. The samples in a powder form were pressed in indium. The CL spectra were recorded at an accelerating voltage of 15 kV and room temperature. The diameter of the beam on the samples was 1 μm. The beam current was 1.5 nA. The color images were recorded with a camera through an optical microscope with a defocused electron beam of about 200 μm.

3. Results and Discussion

3.1. X-ray excited luminescence characterization

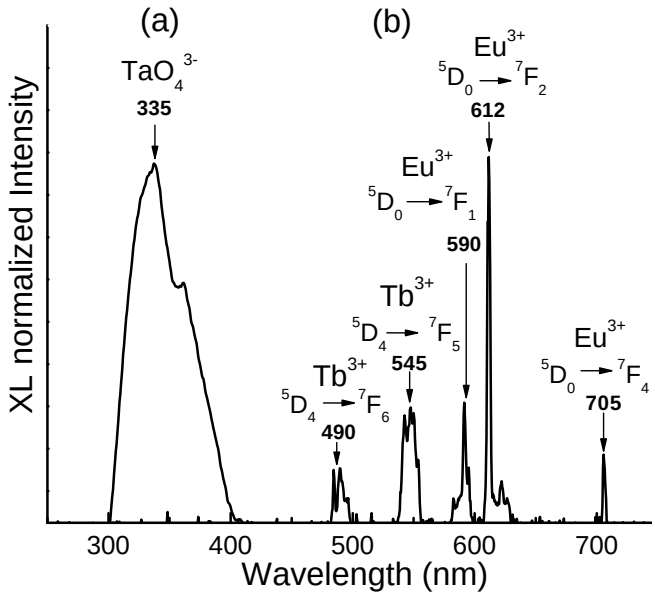

Fig. 2. X-ray emission spectra of the TaO_4^{3-} group in (a) the $YTaO_4$ and (b) $YTaO_4$:Eu^{3+},Tb^{3+} host lattices.

The XEL spectra of the host lattice doubly activated with Eu^{3+} and Tb^{3+} and without activators are shown in Fig. 2. Figure 2a shows the XEL of the $YTaO_4$ host lattice without activators. The emission peak is localized at 335 nm for $YTaO_4$. Figure 2b shows the luminescence spectrum of the host lattices doubly doped with the rare-earth ions. The emission spectra were measured in a range of 200–1200 nm; the peaks were mostly detected in a range of 450–725 nm. The first two peaks at 490 and 545 nm correspond to Tb^{3+}, and the peaks at 590, 612, and 705 nm are the Eu^{3+} contribution to the luminescence.

Figures 2a and 2b ($YTaO_4$ and $YTaO_4$:Eu^{3+},Tb^{3+}, respectively) clearly show that the simultaneous incorporation of rare-earth ions, such as Eu^{3+} and Tb^{3+}, which partly substitute the Y ions from the host crystalline lattice, leads to the formation of Eu^{3+} and Tb^{3+} emission centers (Fig. 3).

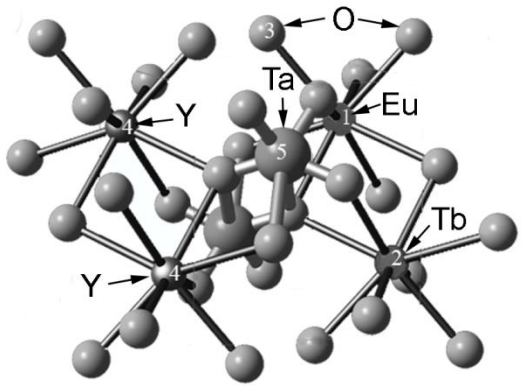

Fig. 3. Crystal structure of $YTaO_4$ with double activation with Eu^{3+} and Tb^{3+}.

In this case, the excitation energy is first absorbed by the host lattices; the process involves the transition between the 4d-like states of Y and the 2p-like states of O. The absorbed energy can be further transferred to the TaO_4^{3-} groups and at last transferred to the Eu^{3+} or Tb^{3+} centers. It is also possible that, under certain energy conditions, energy transfer between the activators takes place because of the proximity of the $^5D_4$ (Tb^{3+}) and $^5D_1$ (Eu^{3+}) energy levels [8]. In this case, the Eu–Tb activator couple can act as a donor–acceptor pair (Fig. 4).

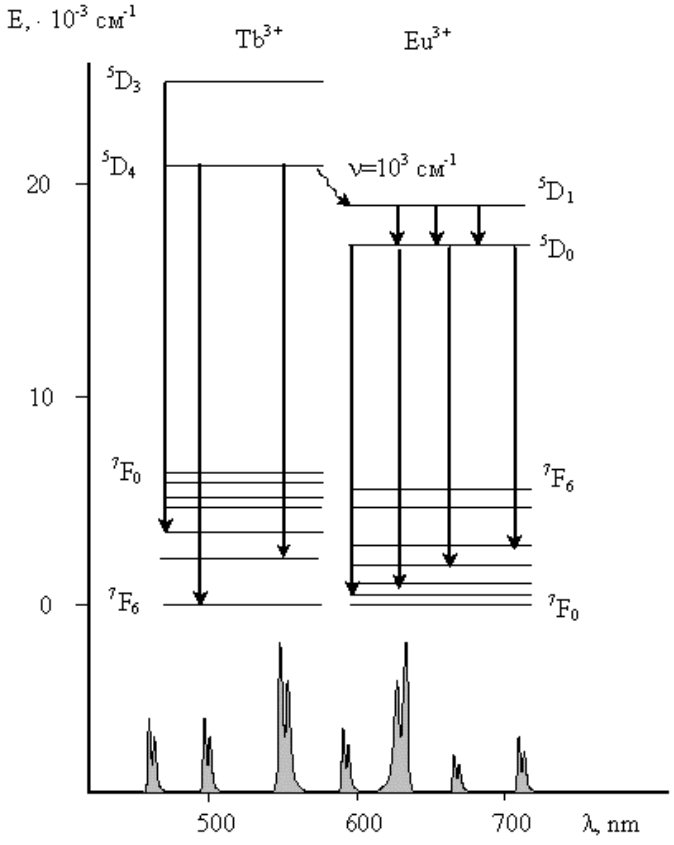

Fig. 4. Schematic representation of energy transfer in $YTaO_4$ double activated with Tb^{3+} and Eu^{3+} ions.

The molar concentration of the incorporated activators (Eu^{3+} and Tb^{3+}) can be varied to obtain a broad variation of visible photoluminescence.

3.2. Cathodoluminescence spectroscopy and CCL characterization

Under electron beam excitation (CL), the $^5D_0 \rightarrow {}^7F_j$ (j = 1,2,3,4) and $^5D_1 \rightarrow {}^7F_1$ emission peaks are observed (Fig. 5). Comparison of Fig. 2b and Fig. 5 shows that the CL and XEL spectra are similar.

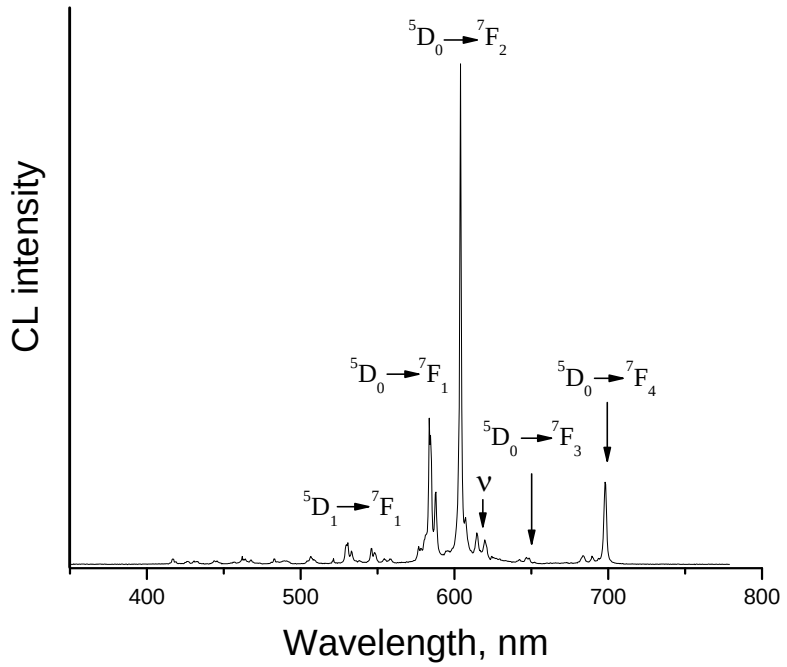

Fig. 5. Emission CL spectra under electron beam excitation of M'-type $Y_{0.95}Eu_{0.05}TaO_4$ (ν-vibronic transitions).

For the phosphors activated with Eu^{3+} and Tb^{3+} (Figs. 2 and 5), the magnetic dipole transitions are weaker in intensity ($^5D_0 \rightarrow {}^7F_1$ and $^5D_4 \rightarrow {}^7F_6$, respectively). The $^5D_0 \rightarrow {}^7F_4$ transition intensity is clearly seen under X-ray and electron beam excitation. Typically, this emission is extremely weak and cannot be seen under UV excitation [9]. Under X-ray and electron beam excitation, the empty upper levels of $^5D_0 \rightarrow {}^7F_4$ emission can be readily filled. This factor is responsible for the appearance of a visible $^5D_0 \rightarrow {}^7F_4$ transition and the increment of the luminescence intensity of Eu^{3+} and Tb^{3+} emission centers under these high-energy excitations.

Figure 6 shows CCL images (top) of the $YTaO_4$ host lattice due to the incorporation of europium and terbium activators and their CL spectra (bottom). The CCL image of the host ($YTaO_4$) lattice without activators is shown in Fig. 6a. A weak blue-violet color is seen due to the small tail of the spectrum after 400 nm in the XEL and CL spectra (Figs. 2a and 6e). Some green spots or speckles are also seen in this image; they suggest the presence of Tb^{3+}-containing particles in the sample. In the case of a heterogeneous material, the local cathodoluminescence

method can be used to avoid these admixtures. By choosing one or more spots in the sample and averaging them, it is possible to elude these undesired peaks, in our case, the $^5D_4 \rightarrow {}^7F_5$ and $^5D_4 \rightarrow {}^7F_6$ transitions (Fig. 2).

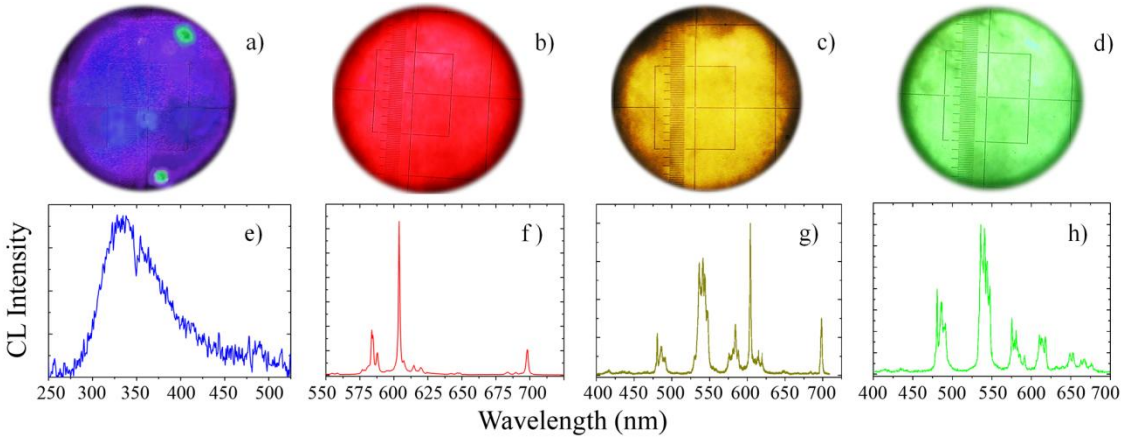

Fig. 6. Color cathodoluminescence images and CL spectra: (a, e) $YTaO_4$; (b, f) $YTaO_4:Eu^{3+}$; (c, g) $YTaO_4:Eu^{3+},Tb^{3+}$; and (d, h) $YTaO_4:Tb^{3+}$ (in original colors).

Figures 6b and 6d show the manifestation of bright red and green color chromaticity, which is the contribution of the Eu^{3+} and Tb^{3+} rare-earth activators, respectively. In the case of similar molar concentrations of Eu^{3+} and Tb^{3+} (Eu^{3+} = 2.5 mol %, Tb^{3+} = 2.5 mol %), the photoluminescence of the phosphor from the rare-earth ions exhibits a yellowish color in the CL image (Fig. 6c), which results from the mixing of green and red. The proportion of Eu^{3+} and Tb^{3+} in the host lattice can be varied from 0 to 5 mol % to obtain a broad range of different colors between red and green.

4. Conclusions

Owing to the partial substitution of Eu^{3+} and Tb^{3+} activators for Y ions, the emission centers are red-shifted toward longer wavelengths and both activators contribute to the overall luminescence. The molar concentration of the incorporated activators can be varied to obtain a broad variation of visible photoluminescence. This dependence of chromaticity on the concentration of incorporated activators is clearly seen in CCL.

These double activated phosphors can be applied in the X-ray intensifying screens for medical diagnosis with variable photoluminescence colors and in other optoelectronic devices.

Acknowledgments. This work was supported by the ANCD National Research Program (project no. 20.80009.5007.19).

References

[1] L. H. Brixner, Mater. Chem. Phys. 16, 253 (1987).
[2] M. Nazarov and D. Y. Noh, New Generation of Europium and Terbium Activated Phosphors, Pan Stanford, New York, 2011.
[3] G. Blasse and B.C. Grabmaier, Luminescent Materials, Springer Verlag, Berlin, 1994.
[4] G. M. Wolten, Acta Crystallogr. 23, 939 (1967).
[5] L. H. Brixner and H. Chen, J. Electrochem. Soc. 130, 2435 (1983).
[6] G. Blasse and L. H. Brixner, J. Solid State Chem. 82, 115 (1989).
[7] M. V. Zamoryanskaya, S. G. Konnikov, and A. N. Zamoryanskii, Instrum. Exp. Tech. 47, 4, 477 (2004).
[8] M. V. Nazarov, D. Y. Jeon, J. H. Kang, E. J. Popovici, L.-E. Muresan, M. V. Zamoryanskaya, and B. S. Tsukerblat, Solid State Commun. 131, 307 (2004).
[9] E. J. Popovici, M. Nazarov, F. I. Lucaci, Do Young Noh, Maria Stefan, and Emil Indrea, 15th International Conference on luminescence and optical spectroscopy of condensed matter, Lyon, July 7–11, 2008, France, p. 219.

A STUDY OF WIDE BAND $Zn_{1-x}Mg_xO$ AND $(Ga_xIn_{1-x})_2O_3$ THIN FILMS PREPARED BY THE SPIN COATING METHOD

Vadim Morari[1*], Veaceslav Ursaki[2,3], Lidia Ghimpu[1], Emil Rusu[1], and Ion Tiginyanu[2,3]

[1]Ghitu Institute of Electronic Engineering and Nanotechnologies, Chisinau, MD-2028 Republic of Moldova
[2]National Center for Materials Study and Testing, Technical University of Moldova, Chisinau, MD-2004 Republic of Moldova
[3]Academy of Sciences of Moldova, Chisinau, MD-2001 Republic of Moldova.
**E-mail:vadimmorari2018@gmail.com*

https://doi.org/10.53081/mjps.2022.21-1.02

Abstract

This study presents a brief analysis of $Zn_{1-x}Mg_xO$ and $(Ga_xIn_{1-x})_2O_3$ thin films deposited on Si substrates by the spin coating method. The morphology and chemical composition of the prepared thin films were studied by scanning electron microscopy (SEM) and energy dispersive X-ray (EDX) analysis. The evolution of the crystal structure with a change in the film composition and the technological conditions for annealing after spin coating was studied by X-ray diffraction (XRD) analysis. The annealing atmosphere and temperature were optimized in terms of producing films with a stoichiometric composition and a high crystalline quality.

Keywords: thin films, SEM, EDX, XRD, spin coating, stoichiometry, crystal structure.

Rezumat

Acest studiu prezintă o scurtă analiză a filmelor subțiri de $Zn_{1-x}Mg_xO$ și $(Ga_xIn_{1-x})_2O_3$ depuse pe substraturi de Si prin metoda spin coating. Morfologia și compoziția chimică a filmelor subțiri obținute au fost studiate prin microscopie electronică cu scanare (SEM) și analiză cu raze X cu dispersie de energie (EDX). Evoluția structurii cristaline odată cu modificarea compoziției filmului și a condițiilor tehnologice de recoacere după depunerea prin metoda spin coating, a fost investigată prin analiza de difracție cu raze X (XRD). Atmosfera de recoacere și temperatura au fost optimizate din punct de vedere al obținerii filmelor cu compoziție stoichimetrică și structură cristalină de calitate înaltă.

Cuvinte cheie: filme subțiri, SEM, EDX, XRD, spin coating, stoichiometrie, structură cristalină.

1. Introduction

In the last years, a lot of emphasis has been placed on wide band gap optoelectronic devices, particularly those based on SnO_2 films with high electrical conductivity properties combined with excellent transparency and thermal stability [1, 2]. Tin oxide SnO_2, being a wide

band gap semiconductor, has a band gap of 3.6 eV at room temperature. At the same time, indium tin oxide (ITO) with the band gap in a range of 3.5–4.3 eV is also a thoroughly studied material due to its high conductivity and optical transparency [3]. Zinc oxide (ZnO) with a band gap of 3.4 eV is also used in optoelectronic devices due to its advantages over gallium nitride (GaN) in terms of technological aspects [4]. Thin films of zinc oxide with different Mg concentrations in the precursor solutions for obtaining a $Zn_{1-x}Mg_xO$ solid solution offer the possibility of modeling the optical, luminescent, and photoelectric properties in a fairly wide range to reach a band gap of up to 7.8 eV [5–8]. Typically, these thin films are prepared by atomic layer deposition [9, 10], molecular beam epitaxy [11, 12], pulsed laser deposition [13, 14], and magneton sputtering [15]. Thin films of $(Ga_xIn_{1-x})_2O_3$ represent another attractive oxide semiconductor due to possibilities of tuning the material bandgap in a wide range of 3.5–5 eV by changing the alloy composition. In particular, this material system is promising for short-wavelength optical applications, such as solar-blind UV detectors [16–20]. Thin films of In_2O_3 and Ga_2O_3 have been previously obtained by different growth methods, such as metal-organic chemical vapor deposition (MOCVD) [21], halide vapor phase epitaxy (HVPE) [22], molecular beam epitaxy (MBE) [23], and pulsed laser deposition (PLD) [24]. Little attention has been given to films obtained by the spin coating method, despite the fact that it is one of the cheapest techniques. This paper presents a summary of our research on the change in film morphology using different annealing atmospheres for $Zn_{1-x}Mg_xO$ and the change in crystal structure depending on the Ga content for $(Ga_xIn_{1-x})_2O_3$ deposited on Si substrates by the spin coating method.

2. Sample Preparation Experimental Details

Solutions of zinc acetate ($Zn(CH_3CO_2)_2 \times 2H_2O$) and magnesium acetate ($Mg(CH_3COO)_2 \times 4H_2O$) (0.5 M) were dissolved in 2-methoxyethanol and diethanolamine (DEA), an organic compound with the formula $HN(CH_2CH_2OH)_2$ as a stabilizer, to obtain $Zn_{1-x}Mg_xO$ thin films by the spin coating method. The ZnO solutions with different Mg concentrations were mixed in an ultrasonic bath at a temperature of 50–60°C for 30 min. Spin coating was performed at room temperature on Si substrates in multiple coating cycles (5, 10, 15) at a rotational speed of 3000 rpm with 30-s rotation followed by drying the coated layer at 180°C for 10 min. After depositing a number of layers, which determine film thickness, some samples were analyzed by SEM and EDX without heat treatment, while other samples were analyzed after annealing in air and an argon atmosphere at a temperature of 500°C for 1 h.

For the deposition of $(Ga_xIn_{1-x})_2O_3$ thin films on Si substrates by the spin coating method, solutions of indium chloride ($InCl_3$) and gallium nitrate ($Ga(NO_3)_2$) (0.5M) were dissolved in 2-methoxyethanol and DEA as a stabilizer. The In_2O_3solutions with different Ga concentrations were mixed in an ultrasonic bath at a temperature of 50–60°C during 30 min before the deposition process. Spin coating was performed at room temperature on Si substrates in five coating cycles at a rotational speed of 3000 rpm with 30-s rotation followed by drying the coated layer at 180°C for 10 min. Similarly to $Zn_{1-x}Mg_xO$ films, after depositing a number of layers, the samples were treated at a temperature of 500°C in air for 1 h.

The morphology and chemical composition of the prepared films were studied by scanning electron microscopy (SEM) on a FEI Helios Nanolab 600 (SEM/FIB) combined instrument with a gallium focused ion beam equipped with a built-in X-ray detector with a sensor area of 30 mm^2 (Ametek, model ELECT PLUS) for energy dispersive X-ray (EDX) analysis. Analysis of the crystal structure and phases content in the thin films was performed using a Bruker AXS D8

DISCOVER X-ray diffractometer using monochromatic Cu$K_{\alpha 1}$ radiation (λ = 0.15406 Å) operating at a 40-kV beam voltage and a 40-mA beam current. Diffraction pattern data were collected for 2θ diffraction angles of 20°–80°.

3. Characterization of the Prepared Thin Films

One of the most thoroughly studied oxide semiconductor films is ZnO, which has a high exciton binding energy of 60 meV, which makes the excitons stable even at room temperature. The band gap of the material can be controlled by adding Mg in a certain concentration into the precursor solution of ZnO films to shift the spectral range of sensitivity to shorter wavelengths. Figure 1 shows the morphology of $Zn_{0.8}Mg_{0.2}O$/Si thin films prepared by the spin coating method and annealed in the different atmospheres at 500°C.

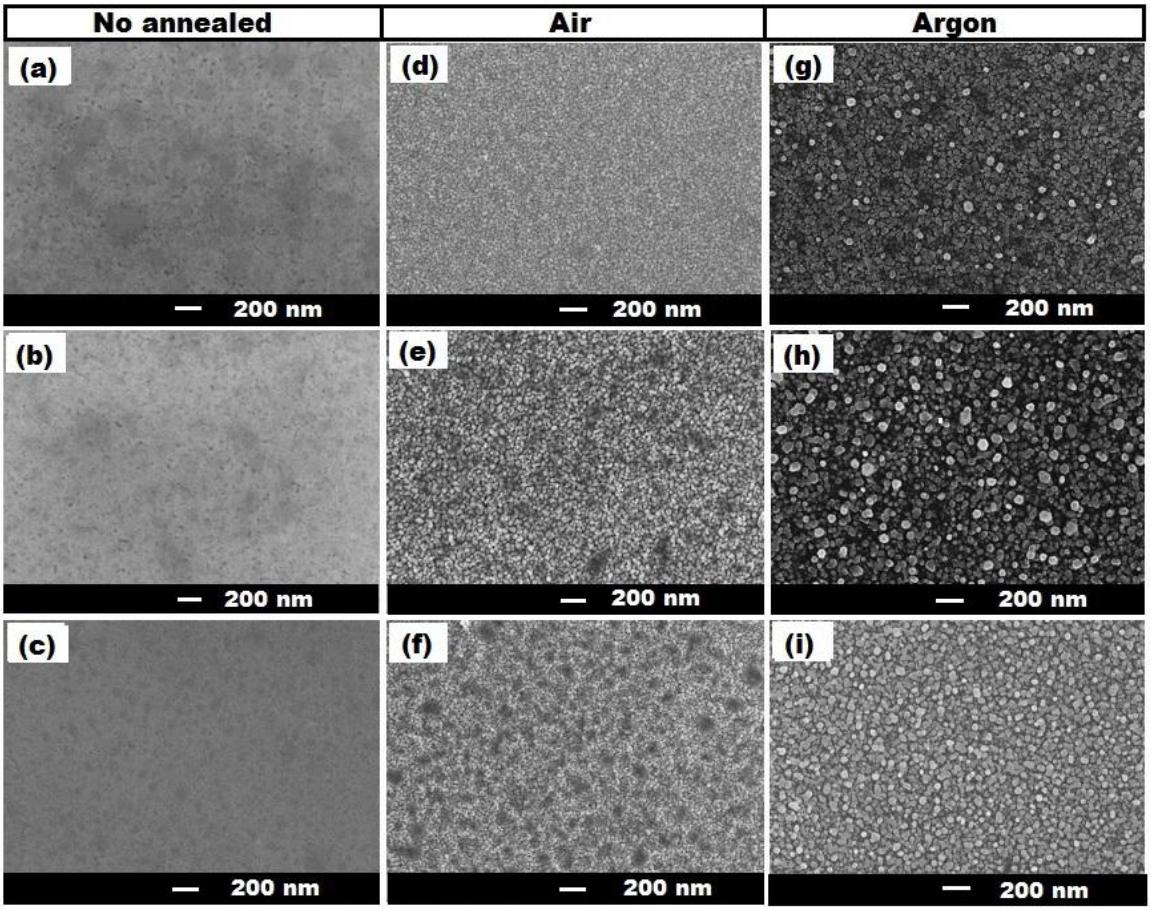

Fig. 1. Scanning electron microscopy images: top view of $Zn_{0.8}Mg_{0.2}O$/Si thin films prepared by the spin coating method and annealed in the different atmospheres: the first column shows samples with 15, 10, and 5 layers without annealing (a–c); the second column shows samples with 15, 10, and 5 layers, which were annealed in air (d–f); the third column shows samples with 15, 10, and 5 layers, which were annealed in argon (g–i).

It is evident from the images that the films without annealing are amorphous and do not contain any nanograins, regardless of their thickness (Figs. 1a–1c). In the case of annealing in air, nanograins are evident (Figs. 1d–1f). Annealing in argon shows the best results in terms of

nanograin size and quality (Figs. 1g–1i). The largest nanograins are detected in the samples with 10 deposited layers (Figs. 1e, 1h), which were annealed in air or argon; the crystallite size in them is about 20 and 50 nm, respectively.

Figure 2 summarizes the dependence of film thickness on the number of deposition cycles for $Zn_{0.8}Mg_{0.2}O$/Si thin films prepared by the spin coating method and annealed in the different atmospheres. It is evident that the film thickness increases with an increase in the number of layers. The film thickness increases from 50 to 90 and 155 nm with an increase in the number of deposited layers from 5 to 10 and 15, respectively. Analysis of the results suggests that the film composition is non-stoichiometric, especially for the non-annealed films. This fact can be attributed to a large amount of carbon coming from the organic compound used as a precursor. However, the stoichiometry is improved after annealing due to a decrease in the amount of carbon. The samples treated in argon at 500°C are closer to stoichiometry; the best result in terms of stoichiometry and morphology is achieved for the 10-layer sample. Table 1 shows results of EDX analysis of $Zn_{0.8}Mg_{0.2}O$ thin films with different thicknesses prepared by the spin coating method and annealed in the different atmospheres.

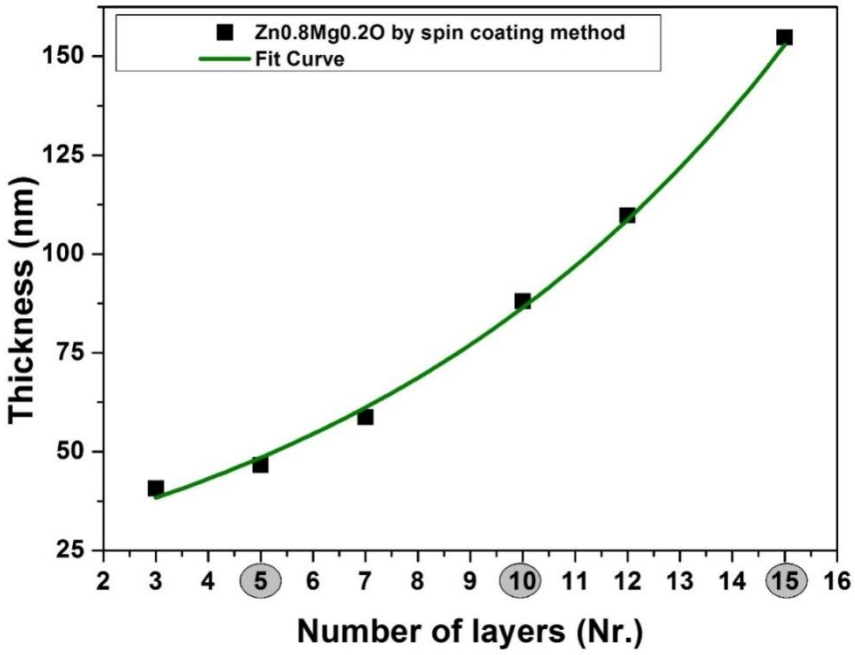

Fig. 2. Dependence of film thickness on the number of deposition cycles for $Zn_{0.8}Mg_{0.2}O$/Si thin films prepared by the spin coating method and annealed in an argon atmosphere.

The XRD analysis (Fig. 3) revealed a single-phase wurtzite structure of the $Zn_{0.8}Mg_{0.2}O$ thin film [5, 25]. The non-annealed films are amorphous. Reflections from the wurtzite phase of the ZnMgO films (PDF card no. 01-078-3032) appear after annealing in air, while the best crystalline quality is obtained in the case of annealing in an argon atmosphere, as evidenced by the higher intensity of XRD reflections.

Table 1. Results of EDX analysis of $Zn_{0.8}Mg_{0.2}O$ thin films with different thicknesses prepared by the spin coating method and annealed in the different atmospheres

	No annealed			Air			Argon		
15 – layers	Elements	Weight %	Atomic %	Elements	Weight %	Atomic %	Elements	Weight %	Atomic %
	Mg	39.89	28.52	Mg	47.49	25.68	Mg	42.90	22.91
	Zn	60.11	71.48	Zn	52.51	74.32	Zn	57.10	77.09
	Total	100.00	100.00	Total	100.00	100.00	Total	100.00	100.00
10 – layers	Elements	Weight %	Atomic %	Elements	Weight %	Atomic %	Elements	Weight %	Atomic %
	Mg	41.63	31.22	Mg	35.30	27.23	Mg	42.53	23.50
	Zn	58.37	68.78	Zn	64.70	72.77	Zn	57.47	76.50
	Total	100.00	100.00	Total	100.00	100.00	Total	100.00	100.00
5 – layers	Elements	Weight %	Atomic %	Elements	Weight %	Atomic %	Elements	Weight %	Atomic %
	Mg	43.58	32.78	Mg	45.10	28.15	Mg	49.02	25.60
	Zn	56.42	67.22	Zn	54.90	71.85	Zn	50.98	74.40
	Total	100.00	100.00	Total	100.00	100.00	Total	100.00	100.00

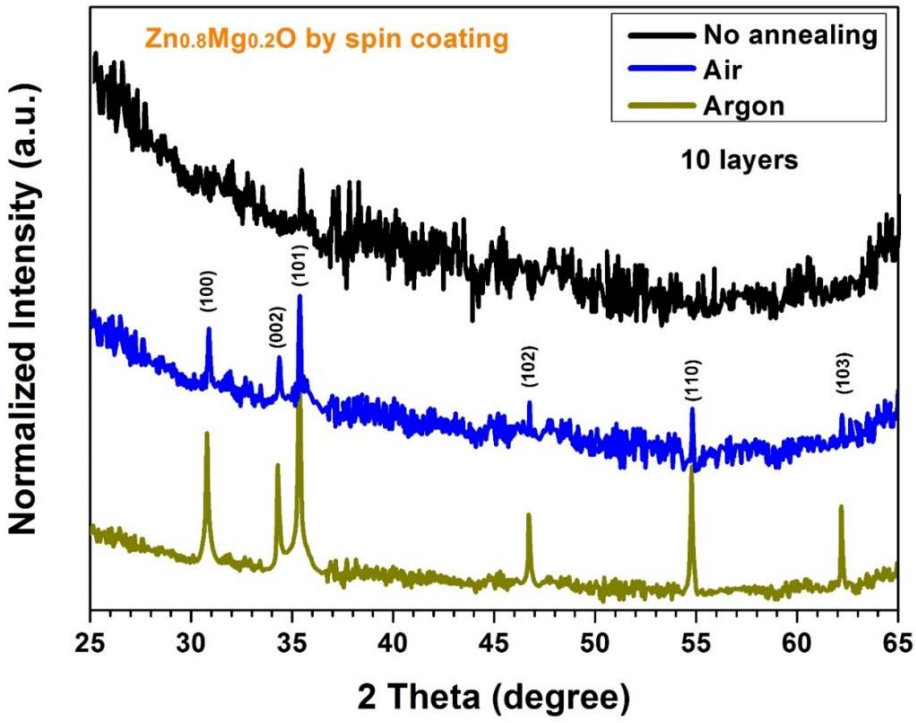

Fig. 3. X-ray diffraction pattern of $Zn_{0.8}Mg_{0.2}O$/Si thin films (10 layers) prepared by the spin coating method and annealed in the different atmospheres.

Semiconductor oxide $(Ga_xIn_{1-x})_2O_3$ films, the band gap of which changes from 3.5 to 5 eV with a change in the alloy composition, are another material system studied in this work. Figure 4 compares the XRD patterns of $(Ga_xIn_{1-x})_2O_3$ thin films prepared by the spin coating method with a variation in the Ga concentration (x).

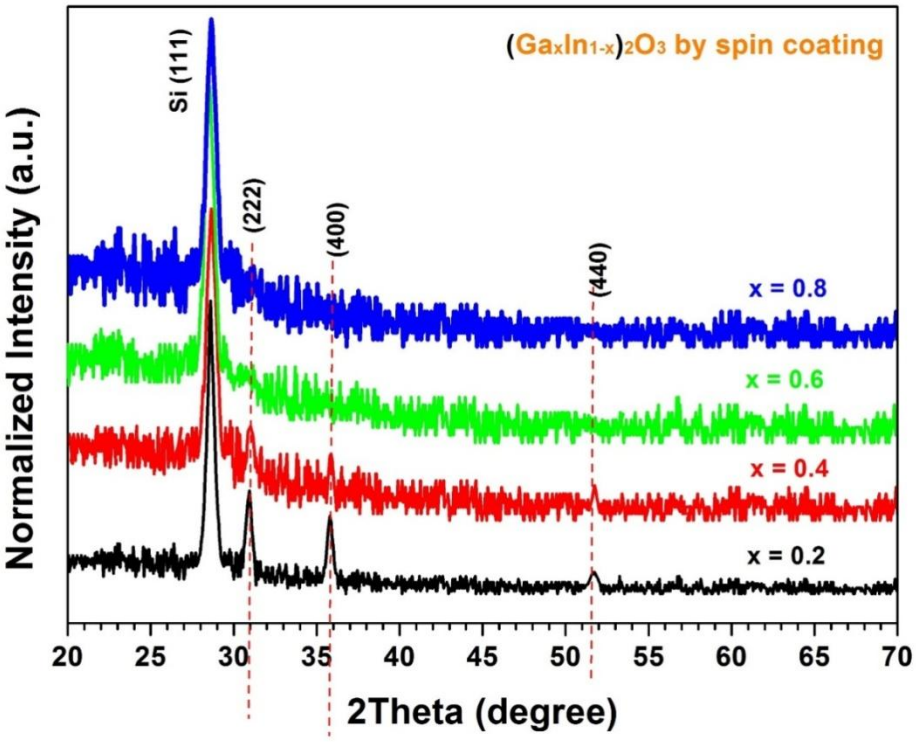

Fig. 5. X-ray diffraction pattern of $(Ga_xIn_{1-x})_2O_3$/Si thin films prepared by the spin coating method with a variation the Ga concentration (x).

The intensity of the reflections decreases with an increase in the x value up to 0.8; this fact indicates the loss of crystallinity and amorphization of the films.

Figure 4 compares the morphology of $(Ga_xIn_{1-x})_2O_3$ thin films prepared by the spin coating method with a variation in the Ga concentration (x).

The SEM images suggest that the thin film with $In_{0.8}Ga_{0.2}O$ composition are formed from small nanograins. However, the morphology evolves to amorphous formations with increasing the Ga content in films, which become more evident for the film with $In_{0.2}Ga_{0.8}O$ compostion. This siggestion is also corroboratoed by the results of the XRD analysis as discussed above.

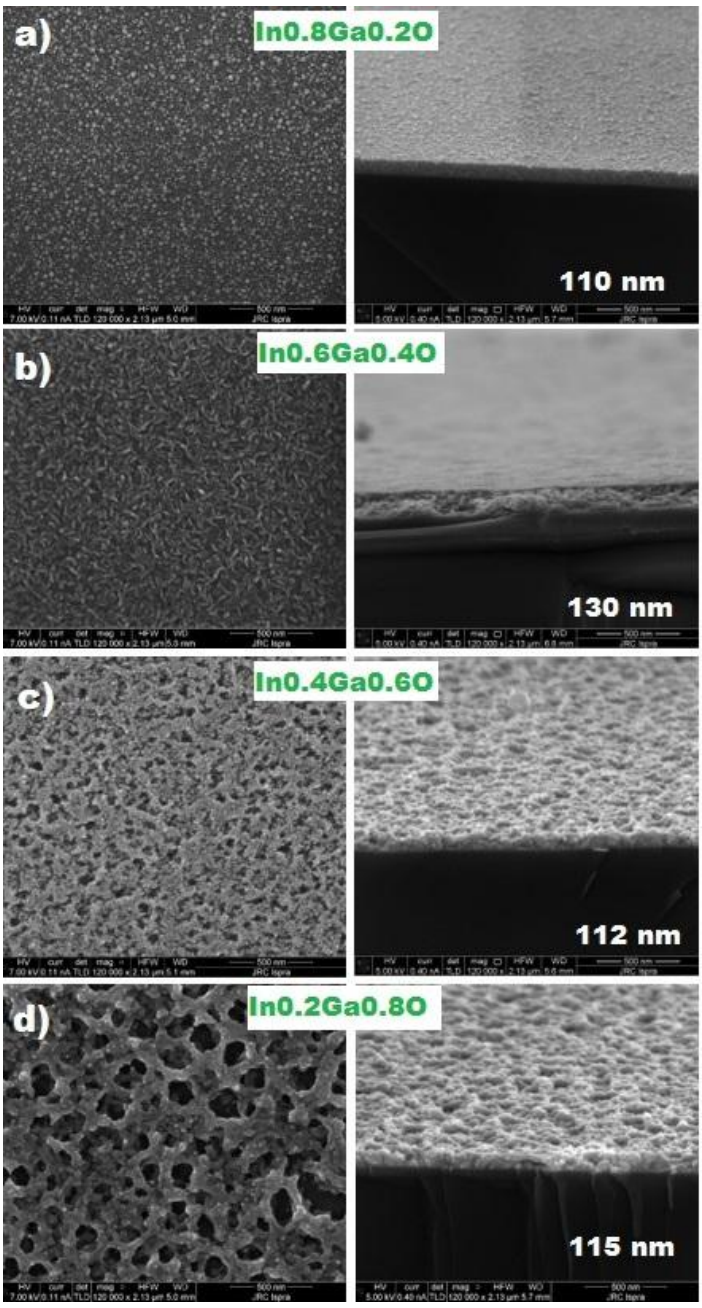

Fig. 4. Scanning electron microscopy images: top view (left column) and cross section view (right column) of $(Ga_xIn_{1-x})_2O_3$/Si thin films prepared by the spin coating method with a variation in the Ga concentration (x).

Table 2 shows results of EDX analysis of $(Ga_xIn_{1-x})_2O_3$ thin films with a variation in the Ga concentration (x). The quantitative EDX analysis suggests that a deficiency of Ga is characteristic of all the films.

Table 2. Results of EDX analysis of $(Ga_xIn_{1-x})_2O_3$ thin films prepared by the spin coating method

$In_{0.8}Ga_{0.2}O$			$In_{0.6}Ga_{0.4}O$		
Elements	**Weight %**	**Atomic %**	**Elements**	**Weight %**	**Atomic %**
Ga	14.69	**17.08**	**Ga**	27.43	**31.36**
In	85.31	**82.92**	**In**	72.57	**68.64**
Total	**100.00**	**100.00**	**Total**	**100.00**	**100.00**
$In_{0.4}Ga_{0.6}O$			$In_{0.2}Ga_{0.8}O$		
Elements	**Weight %**	**Atomic %**	**Elements**	**Weight %**	**Atomic %**
Ga	42.58	**47.43**	**Ga**	70.98	**61.89**
In	57.42	**52.57**	**In**	31.02	**38.11**
Total	**100.00**	**100.00**	**Total**	**100.00**	**100.00**

5. Conclusions

The obtained results show that the quality of $Zn_{1-x}Mg_xO$ and $(Ga_xIn_{1-x})_2O_3$ thin films deposited by the spin coating method on silicon substrates is significantly affected by the technological conditions of preparation. Annealing atmosphere is extremely important for obtaining ZnMgO films with a high-quality crystalline structure. To prepare high-quality films, it is desirable that annealing should be performed in an argon atmosphere at a temperature of 500°C. The concentration of precursor solutions for the preparation of GaInO films also significantly affects the morphology and crystalline structure of the material. With an increase in the Ga content, the films become amorphous and the morphology changes considerably. To prepare GaInO films with a stoichiometric composition, it is necessary to provide the presence of excess Ga in the precursor solutions.

Acknowledgments. This work was financially supported by the National Agency for Research and Development of the Republic of Moldova under the grants #20.80009.5007.02 “Advanced Nanostructured Materials for Thermoelectric and Sensor Applications” and by the Horizon-2020 research and innovation programme of the European Union (grant no. 810652, NanoMedTwin project).

References

[1] M. Karmaoui, A. B. Jorge, P. F. McMillan, A. E. Aliev, R. C. Pullar, J. A. Labrincha, and D. M. Tobaldi, ACS Omega 3 (10), 13227 (2018). https://doi:10.1021/acsomega.8b02122

[2] O. Mounkachi, E. Salmani, M. Lakhal, H. Ez-Zahraouy, M. Hamedoun, M. Benaissa, and A. Benyoussef, Sol. Energy Mater. Sol. Cells 148, 34 (2016). https://doi:10.1016/j.solmat.2015.09.062

[3] M. Thirumoorthi and J. Thomas Joseph Prakash, J. Asian Ceram. Soc. 4 (1), 124 (2016). https://doi:10.1016/j.jascer.2016.01.001

[4] H. Qiu, C. Cao, and H. Zhu, Mater. Sci. Eng. B 136 (1), 33 (2007). https://doi:10.1016/j.mseb.2006.08.062
[5] V. Morari, E. V. Rusu, V. V. Ursaki, K. Nielsch, and I. M. Tiginyanu. IFMBE Proc., Springer Nature Switzerland AG 87, 32 (2022). https://doi.org/10.1007/978-3-030-92328-0_5
[6] V. Morari, E. V. Rusu, V. Postolache, V. V. Ursaki, I. M. Tiginyanu, A. V. Rogachev, and A. V. Semchenko, Rom. J. Phys. 66 (7–8), Article no. 609, 1 (2021). ONLINE: ISSN 1221-146X.
[7] V. Morari, A. Pantazi, N. Curmei, V. Postolache, E. V. Rusu, M. Enachescu, I. M. Tighineanu, and V. V. Ursaki, Beilstein J. Nanotechnol. 11, 899 (2020). https://doi.org/10.3762/bjnano.11.75
[8] V. Morari, V. Postolache, G. Mihai, E. Rusu, Ed. Monaico, V. V. Ursachi, K. Nielsch, and I. M. Tiginyanu, IFMBE Proc., Springer 77, 105 (2020). Print ISSN 1680-0737, Online 1433-9277. https://doi.org/10.1007/978-3-030-31866-6
[9] H.-Y. Lee, W.-H.Tsai, and Y.-C. Lin, J. Vac. Sci. Technol. B 34, 051207 (2016).
[10] J. S. Wrench, I. F. Brunell, P. R. Chalker, J. D. Jin, and A. Shaw, Appl. Phys. Lett. 105, 202109 (2014).
[11] Y. N. Hou, Z. X. Mei, H. L. Liang, D. Q. Ye,and C. Z. Gu, Appl. Phys. Lett. 102, 153510 (2013).
[12] M. M. Morshed, M. Suja, Z. Zuo, and J. Liu, Appl. Phys. Lett. 105, 211107 (2014).
[13] S. Choopun, R. D. Vispute, W. Yang, R. P. Sharma, and T. Venkatesan, Appl. Phys. Lett. 80, 1529 (2002).
[14] X. Wang, K. Saito,T. Tanaka, M. Nishio, and Q. Guo, J. Alloys Compd. 627, 383 (2015).
[15] J.-S. Shiau, S. Brahma, C.-P. Liu,and J.-L.Huang, Thin Solid Films 620, 170 (2016).
[16] Y. G. Kim, T. Kim, C. Avis, S.-H. Lee, and J. Jang, IEEE Trans. Electron Devices 63, 1078 (2016).
[17] G. Gonçalves, P. Barquinha, L. Pereira, N. Franco, E. Alves, et al., Electrochem. Solid-State Lett. 13, H20 (2010).
[18] S. I. Stepanov, V. I. Nikolaev, V. E. Bougrov, and A. E. Romanov, Rev. Adv. Mater. Sci. 44, 63 (2016).
[19] W.-L. Huang, M.-H. Hsu, S.-P. Chang, S.-J. Chang, and Y.-Z. Chiou, ECS J. Solid State Sci. Technol. 8, Q3140 (2019).
[20] S. J. Pearton, J. Yang, P. H. Cary, F. Ren, J. Kim, M. J. Tadjer, and M. A. Mastro, Appl. Phys. Rev. 5, 011301 (2018). https://doi.org/10.1063/1.5006941
[21] C. Y. Wang, I. Kirste, F. M. Morales, J. M. Mánuel, et al., J. Appl. Phys. 110 (9), 093712 (2011). https://doi:10.1063/1.3658217
[22] S. Stepanov, V. Nikolaev, A. Pechnikov, M. Scheglov, A. Chikiryaka, A. Chernykh, and A. Y. Polyakov, Phys. Status Solidi A, 218 (3), 2000442 (2020). https://doi:10.1002/pssa.202000442
[23] E. J. Tarsa, J. H. English, J. S. Speck, et al., Appl. Phys. Lett. 62 (19), 2332 (1993). https://doi:10.1063/1.109408
[24] A. Papadogianni, T. Nagata, and O. Bierwagen, Jpn. J. Appl. Phys. 61, 045502 (2022). https://doi.org/10.35848/1347-4065/ac4ec7
[25] V. Morari, V. Postolache, E. Rusu, K. Leistner, K. Nielsch, V. V. Ursaki, and I. M. Tiginyanu, Int. Conf. ATOM-N 2022, 11th edition, August 20–23, Contanta, Romania, Proc. SPIE-Int. Soc. Opt. Eng., Bellingham, USA, vol. 11718, 2020. https://doi.org/10.1117/12.2571189

COPPER-RELATED DEFECTS IN ZnTe THIN FILMS GROWN BY THE CLOSE SPACE SUBLIMATION METHOD

Ion Lungu [1*], Lidia Ghimpu [2], Dumitru Untila [1], and Tamara Potlog [1]

[1] Physics Department and Engineering, Moldova State University, MD-2009, Chisinau, Republic of Moldova
[2] Institute of Electronic Engineering and Nanotechnologies, Academy of Sciences of Moldova, MD-2028, Chisinau, Republic of Moldova
[*]E-mail: ionlungu.usm@gmail.com

https://doi.org/10.53081/mjps.2022.21-1.03

Abstract

Low-temperature photoluminescence (PL) is used to study defects evolution via immersion technique and annealing in vacuum of ZnTe thin films. In this paper we studied how copper doping from solutions of different molar concentrations affects PL of ZnTe thin films grown by close space sublimation (CSS) method. Undoped ZnTe thin films showed PL emission in the (520-680) nm wavelength region. The incorporation of copper in ZnTe produce a number of broad emission bands that correspond to an electron transition from the conduction band to spin-orbit states of the localized level of Cu^{2+} ions. All the studied samples had variable concentrations of oxygen and the possibility of the formation of auxiliary oxides is discussed.

Keywords: ZnTe thin films, ion-exchange doping, polymorph structure, Cu^{2+} defect level.

Rezumat

Fotoluminiscența (FL) la temperaturi joase este utilizată pentru a studia evoluția defectelor prin tehnica de imersie și tratare în vid a straturilor subțiri de ZnTe. În această lucrare am studiat modul în care doparea din soluții de diferite concentrații molare ale cuprului afectează FL straturilor subțiri de ZnTe crescute prin metoda sublimării în spațiu inchis (CSS). Staturile subțiri de ZnTe nedopate au prezentat emisie de FL în regiunea lungimilor de undă (520-680) nm. Încorporarea cuprului în ZnTe produce un număr de benzi largi de emisie care corespund unei tranziții de electroni de la banda de conducție la stările de spin-orbita a nivelului localizat al ionilor Cu2+. Toate probele studiate au avut concentrații variabile de oxigen și se discută posibilitatea formării de oxizi auxiliari.

Cuvinte cheie: straturi subțiri deZnTe, dopare cu schimb de ioni, structură polimorfă, nivel de defect Cu^{2+}.

1. Introduction

Zinc telluride (ZnTe) is a chemically stable and non-hygroscopic group II–VI metal chalcogenide semiconductor exhibiting many useful electrical and optical properties. It has a direct wide bandgap of 2.26 eV (300 K) and *p*-type conductivity [1, 2]. The main reason for the increased interest in the ZnTe semiconductor is its wide application in optoelectronic and microelectronic devices.

Zinc telluride thin films are used in tandem solar cell structures [3] and for synthesizing $Cd_xZn_{1-x}Te/ZnTe$ quantum-well structures [4]. Zinc telluride epitaxial layers are applied as a substrate for various heterojunctions and superlattices [5], γ-ray detectors [6], photodiodes [7], and light-emitting diodes [8]. To tune the optical and electrical properties of ZnTe thin films, some transition elements should be added as a dopant to ZnTe. Doping of ZnTe with transition metals has been studied to improve the *p*-type conductivity and the photoluminescence (PL) and optoelectronic properties. There are a number of reports that describe the synthesis of ZnTe thin films by different methods and their structural and optical properties [9–11]. According to [12–14], copper has the ability to form stable cations partly filled with an incompletely filled *d* orbital that can decrease the electrical resistance of ZnTe. However, all the above-mentioned reports are not sufficient to systematize the obtained physical parameters for industrial applications. Therefore, to determine the optimum doping conditions for ZnTe thin films, systematic studies of their structural, compositional, and PL properties are required. Here, we report PL of the ZnTe thin films doped with Cu taken in different concentrations via immersion into a $Cu(NO_3)_2$ solution.

2. Experimental Details

Zinc telluride thin films were grown on glass substrates by the close spaced sublimation (CSS) method. The substrates were pre-treated in a solution of a mixture of chromium (7 g of $K_2Cr_2O_7$ + 10 mL of H_2O + 100 mL of H_2SO_4) at room temperature for 2–3 h; after that, they were thoroughly washed in distilled water and finally dried in a furnace with a hydrogen atmosphere at a temperature of 200 °C. The growing and doping conditions were described in paper [15]. We only mention here the molar concentrations of copper nitrate $Cu(NO_3)_2$ in solution. In 50 mL of methanol was dissolved $Cu(NO_3)_2$ with molar concentrations from $4{,}2\cdot10^{-3}$ mol/l to $10{,}5\cdot10^{-3}$ mol/l. Subsequently, the annealing of ZnTe thin films at 300 °C for 20 min was performed.

Photoluminescence (PL) spectra were measured at 80 K using a setup based on an MDR-2 high optical power monochromator (with a 600 mm^{-1} diffraction grating and a resolution of ~1 meV) and a multi-alkaline photomultiplier [$(Na_2K)Sb$-Cs]. Photoluminescence was excited using a MDL-III-405 CNI laser (λ = 405 nm) at an average emission power of 100 mW.

The structural parameters recorded with a Rigaku X-ray diffractometer using CuK_α radiation (λ = 1.54056 Å) and the elemental composition of the surface region studied by X-ray photoelectron spectroscopy (XPS) results presented in previous paper [15] will be used for interpretation of the PL data.

3. Results and Discussion

X-ray diffraction patterns (XRD) of undoped ZnTe thin films obtained by CSS at technological conditions mentioned above exhibits polycrystalline polymorph structure with

strong [111] preferred orientation of the crystallites along (111) plane belonging to cubic phase and weak hexagonal phase [15]. The lattice parameter of cubic phase equals to 6.17 Å agrees well with the bulk value of ZnTe (6.085 Å) [16]. For the hexagonal phase of 7.8% Cu-doped ZnTe thin films, the lattice parameters values yield a=3.99 Å and c = 9.43 Å. These values indicate that the hexagonal structure in Cu-doped ZnTe films is distorted in comparison with ideal hexagonal lattice structure. The internal stress induced by the excess volume at grain boundaries is suggested to be the main reason for the lattice distortion. An increase of Cu concentration causes a slightly shift towards lower diffraction angles, a decrease in the full width at half maximum (FWHM) of the peak and an increase in the lattice internal strain.

In Fig.1 are presented XPS spectra of undoped ZnTe (left) thin film and doped with 4.6 at. % Cu (right).

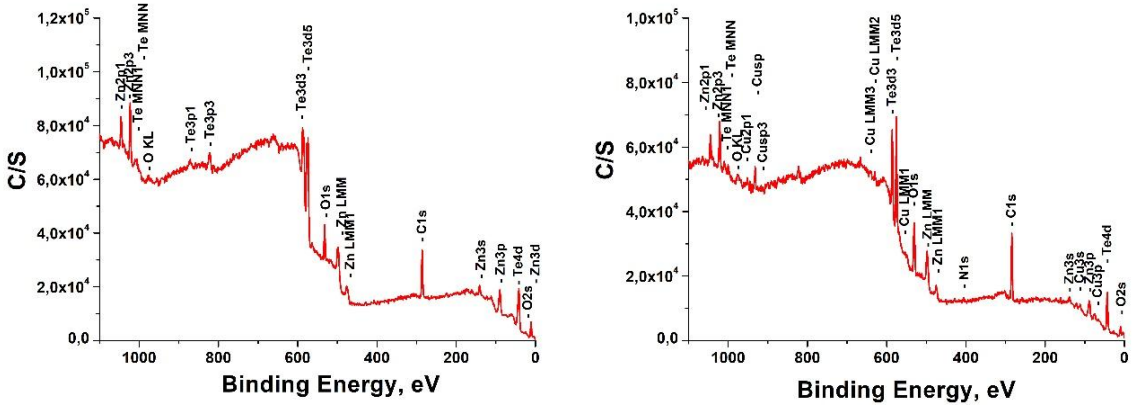

Fig. 1 XPS spectra of undoped ZnTe (left) thin film and doped with 4.6 at. % Cu (right).

XPS study show that undoped films are slightly Te rich and have shown the oxygen in composition. According to XPS measurements the Cu concentration in the ZnTe films was found to change from 1.4 at. % to 7.8 at. %. XPS also proved excessive of Zn atoms on the surfaces of samples after doping with Cu. After doping with copper, there may exist Cu_xTe, that is consistent with references [17,18].

All the studied samples had variable concentrations of O and therefore the possibility of the formation of auxiliary oxides exists.

The PL spectrum of undoped ZnTe thin films measured at 80 K is shown in Fig. 2.

The spectrum exhibit three bands and a shoulder: the more distinct green luminescence band at 535 nm, which becomes predominant in intensity in all studied Cu-doped ZnTe thin films. The broader less intensive band is situated at 580 nm and one another less intensive is located at 645 nm. The PL spectrum of ZnTe doped with $C_M = 4.2 \cdot 10^{-3}$ mol/L of $(CuNO_3)_2$ keep the most intensive peak at 535 nm, as in the case of undoped ZnTe (Fig. 3).

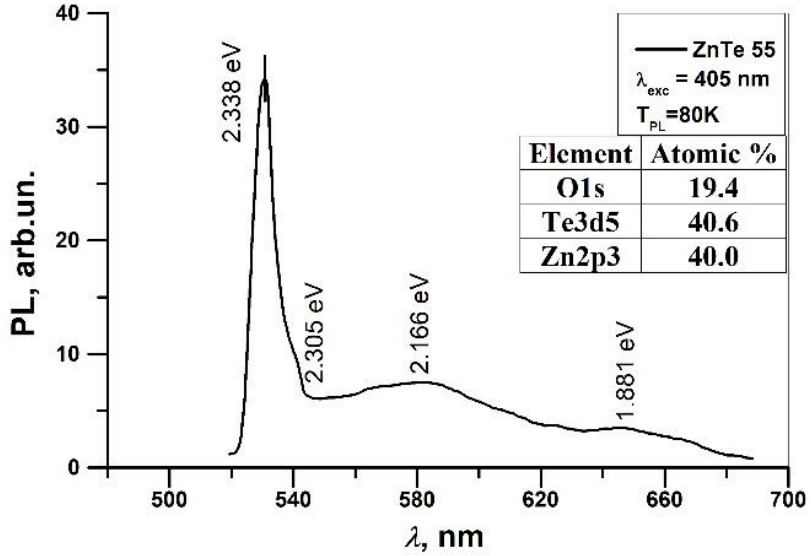

Fig. 2. Photoluminescence spectrum and XPS concentration of elements of undoped ZnTe thin film.

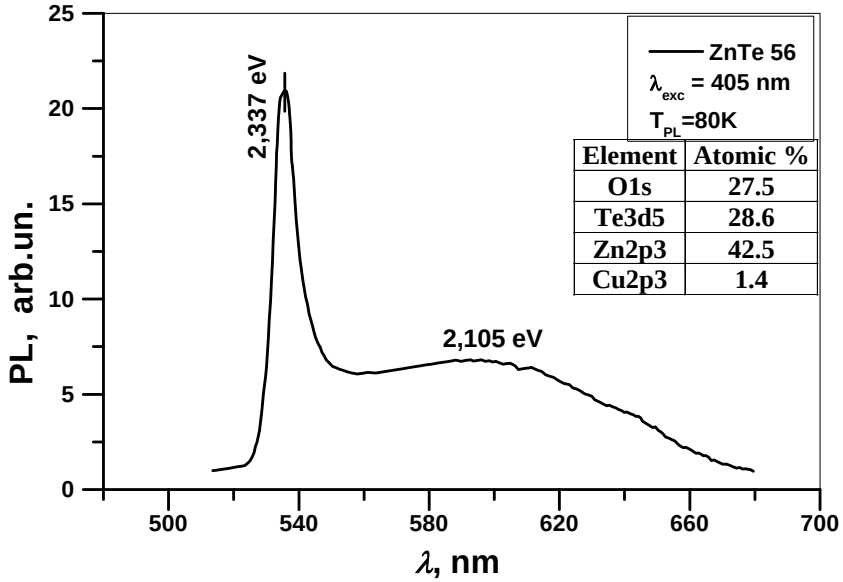

Fig. 3. Photoluminescence spectrum and XPS concentration of elements of 1.4 at% Cu-doped ZnTe thin film.

Deconvolution of a broad band show a maximum at 589 nm and the disappearance of the emission band observed in undoped ZnTe at 645 nm.

With an increase in the molar concentration of Cu(II) nitrate the PL spectrum of Cu-doped ZnTe (Fig. 4) exhibits the same most intensive band as that in the case of the undoped sample

slightly shifted to 528.5 nm.

Deconvolution fitted with a Gaussian distribution in the same intensive slightly shifted narrow band show a shoulder in the shorter wavelengths with maximum at 558 nm. With further increasing in the molar concentration of the Cu(II) nitrate solution $C_M = 8.4 \cdot 10^{-3}$ mol/L, the PL spectrum shown in Fig. 5 exhibits a single broad emission band with a maximum at 539.8 nm. Deconvolution fitted with a Gaussian distribution resulted in three bands: the most intensive bands at 534.1 nm, a less intensive band at 577 nm, and a weak band at 510.8 nm.

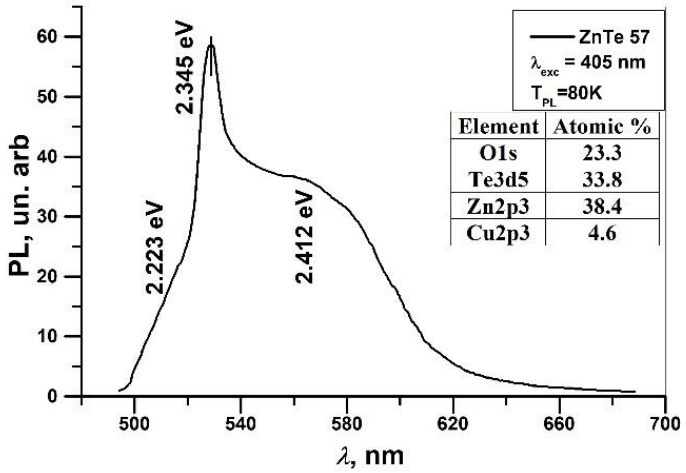

Fig. 4. Photoluminescence spectrum and XPS concentration of elements of 4.6 at% Cu-doped ZnTe thin films.

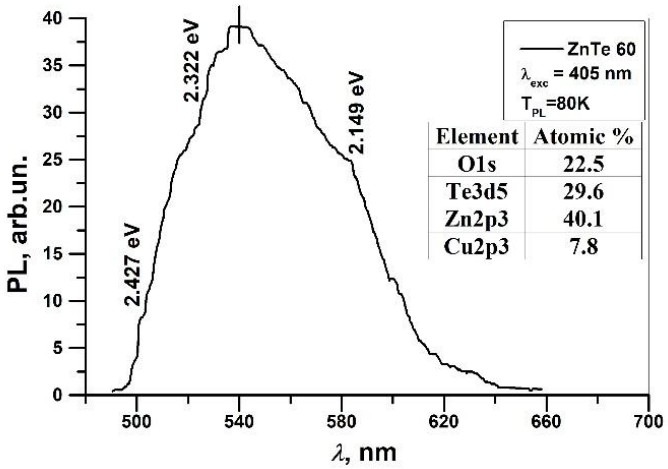

Fig. 5. Photoluminescence spectrum and XPS concentration of elements of 7.8 at% Cu-doped ZnTe thin films.

So, the PL spectra of undoped and doped ZnTe thin films with different molar concentration of Cu (1.4 at.%, 4.6 at.%, 7.8 at.%) are dominated by the narrow green luminescence band. Deconvolution of the most intensive band of undoped ZnTe thin film yielded

an intensive narrow band at 2.338 eV, which is attributed to the radiative recombination of bound excitons trapped at imperfections in ZnTe and a shoulder at 2.305 eV, which indicates a radiative recombination of donor–acceptor pairs. According to the XPS of Te3d and Zn2p3 regions in undoped sample presented in [15] publication, we suppose that PL spectrum consists of essentially bands due to the Zn-Te and Te-O bonds in ZnTe and TeO_2, respectively. A possible interpretation of the donor and the acceptor that contribute to this emission band is that the acceptor is a Zn-vacancy and the donor is a crystal imperfection, such as Te-vacancy or impurities. The emission in the PL spectrum at 2.166 eV is related to the recombination of excitons bound to some extended structural defects. The emission band revealed at 1.881 eV is associated with O_{Te} centers due to the contamination of the ZnTe thin films with oxygen. We agree with the authors of [19] that this most noticeable feature—emission around at 1.881 eV—is attributed to exciton emission bound to isoelectronic oxygen substituting Te atoms (O_{Te}).

The deconvolution of 1.4 at.% Cu-doped ZnTe revealed more intensive broad band with maximum at 589 nm and the disappearance of the emission band observed in undoped ZnTe at 1.881 eV. XPS analysis provides evidence that Cu acting as acceptor center in substitutional site for zinc as believed in [9] publication. According to the high-resolution of Cu2p region for Cu-doped ZnTe films presented in [15] binding energies situated at 931.5 ± 0.3 eV and 951.4 ± 0.3 eV correspond to Cu^+ and Cu^{2+} oxidation states. The binding energy of 951.4 eV is characteristics for Cu-O binding. Thus, coexistence of Cu^+ and Cu^{2+} ions in Cu-doped ZnTe can be concluded and the emission in the PL spectrum at 2.105 eV can be attributed to the presence of copper in ZnTe.

With increase in the molar concentration of Cu(II) nitrate, the interplanar distance (*d*) of the ZnTe phase decreases from 3.5183 Å for $C_M = 4.2 \cdot 10^{-3}$ mol/L to 3.5167 Å for $C_M = 6.3$ mol/L. This fact indicates that the Cu^{2+} ions replace the Zn^{2+} ions according to the reactions:

$$Zn \rightarrow Zn^{2+} + 2e, Cu^{2+} + 2e \rightarrow Cu.$$

The presented XPS of $Te3d_{5/2}$ and Te $3d_{3/2}$ region in [15] at a binding energy of 573.2 and 583.6 eV proves the Zn–Te bonding, while the other two peaks located at 575.3 and 587.2 eV show the co-existence of Te oxide forms in ZnTe that correspond to TeO_2. Ii is of interest that the intensity of the oxide phase of Te is more pronounced than that of the transition peaks of Te representing Zn–Te bonding.

The fact that the Cu-doped ZnTe samples contain excess Zn and the evidences obtained from XPS measurements [15] and in [13, 14] suggest involvement of Cu^{2+} ions in all doped samples. The PL spectrum of 7.8 at% Cu-doped ZnTe (Fig. 5) exhibits the same most intensive peak as that in the case of the undoped sample; it is slightly shifted to 528.5 nm. Deconvolution fitted with a Gaussian distribution resulted in the same intensive slightly shifted narrow band at 2.345 eV attributed to the radiative recombination of bound excitons trapped at the imperfections in ZnTe and a shoulder at 2.223 eV. It can be assumed that this band is attributed to the thermal dissociation of the bound exciton, which liberates the electrons. The intensive broad emission band at 2.412 eV could be assigned to ZnO:Cu.

According to the deconvolution of the O1*s* XPS region of Cu-doped ZnTe thin films presented in [15], its exhibits three peaks: the binding energy located at 531.3 eV corresponds to lattice oxygen (O^{2-}) bonded to the metal, the binding energy of the peak at 530.8 eV corresponds to ZnO, while the peaks at 532 and 532.3 eV are attributed to OH contamination on the surface, which can be due to chemisorption or dissociated oxygen [12].

Therefore, an increase in the PL intensity of the broad emission band at 2.412 eV is mostly attributed to the incorporation of Cu into the ZnO phase. To understand the mechanism, we can suggest that Zn ions are replaced by Cu atoms; the Cu atoms donate two electrons during the

formation of the band and will be in a neutral state with respect to the Cu^{2+} state. This copper related impurity rapidly increases the luminescence intensity.

With a further increase in the molar concentration of the Cu(II) nitrate, the interplanar distance (*d*) of the ZnTe phase decreases from 3.5183 Å for $C_M = 4.2 \cdot 10^{-3}$ mol/L to 3.5159 Å for $C_M = 8.4 \cdot 10^{-3}$ mol/L. The PL spectrum shown in Fig. 5 exhibits a single broad emission band with a maximum at 539.8 nm. The most intensive band at 2.322 eV (534.1 nm) is attributed to the radiative recombination of bound excitons trapped at imperfections in ZnTe; however, the less intensive band at 2.149 eV is attributed to the presence of copper in ZnTe. The PL weak band at 2.427 eV (510.8 nm) is associated with the incorporation of Cu in the ZnO phase. According to XPS analysis, a further increase in the molar concentration of the Cu(II) nitrate to $C_M = 10.5 \cdot 10^{-3}$ mol/L leads to a decrease in the atomic concentration of Cu and gives a Cu content of 1.4 at %. The percentage of the hexagonal phase in ZnTe thin films varies as a function of the $Cu(NO_3)_2$ solution concentration. The hexagonal phase appears only upon a decrease in the excess tellurium level. The PL spectrum of ZnTe with a molar concentration of the Cu(II) nitrate of $C_M = 10.5 \cdot 10^{-3}$ mol/L has the same form as that in the case of the sample with the molar concentration of Cu of $C_M = 4.2 \cdot 10^{-3}$ mol/L.

So, the incorporation of copper in ZnTe has been found to produce a number of broad emission bands that correspond to an electron transition from the conduction band to spin-orbit states of the localized level of Cu^{2+} ions.

4. Conclusions

Zinc telluride thin films have been grown by the CSS method. Copper-doped ZnTe thin films have been synthesized using a Cu(II) nitrate solution as the dopant via simple immersion and subsequently annealing in vacuum. The XRD published results in [15] show that the ZnTe phase in the films has a zinc blende and wurtzite structures. The XRD analysis of the Cu–doped ZnTe films has revealed an increase in the intensity with an increase in the Cu concentration. XPS studies [15] confirmed the presence of the Cu^{2+} oxidation state, and perhaps the Cu_2Te phase also exists but it's difficult to detect, because its three main peaks are located at the same diffraction angles as in ZnTe. The PL spectra are observed in a range of 520–580 nm. The PL spectrum of the undoped and all Cu-doped ZnTe films exhibits an intensive narrow band at 2.338 eV, which can be attributed to the radiative recombination of bound excitons trapped at imperfections in ZnTe. A shoulder at 2.305 eV can be assigned to radiative recombination of the donor–acceptor pairs. The emission in the PL spectrum at 2.166 eV may be associated with the recombination of excitons bound to some extended structural defects. The emission band revealed at 1.881 eV is attributed to O_{Te} centers due to the contamination of the ZnTe thin films with oxygen. All bands presented in PL spectra of Cu-doped ZnTe doped with different molar concentrations (1.4%, 4.6%, and 7.8 at %), outside the narrow band, are related to Cu^{2+} oxidation states.

Formatting of funding sources

Funding: This work was supported by the Ministry of Education, Culture, and Research of the Republic of Moldova, research grant [20.80009.5007.16]

References

[1]W. Mahmood, N.A. Shah, S. Akram, U. Mehboob. 2013. Investigation of substrate temperature effects on physical properties of ZnTe thin films by close spaced sublimation technique, Chalcogenide Lett. 10, 273–281.

[2]W. Wang, G. Xia, J. Zheng, L. Feng, R. Hao, 2007. Study of polycrystalline ZnTe (ZnTe:Cu) thin films for photovoltaic cells. J. Mater. Sci. Mater. Electron. 18, 427–431.

[3]P. Gashin, A.Focsha, T. Potlog, A. V. Simashkevich, V.Leondar. 1997. n-ZnSe/p-ZnTe/n-CdSe tandem solar cells. Solar Energy Materials and Solar Cells, 46(4) 323-331.

[4] A. Bosio, R. Ciprian, A.I. Lamperti, I. Rago, B. Ressel, G. Rosa, M. Stupar, E. Weschke, 2018. Interface phenomena between CdTe and ZnTe:Cu back contact. Solar Energy 176, 186–193.

[5]D. Wu et al. 2016. Construction of ZnTe nanowires/Si p-n heterojunctionsfor electronic and optoelectronic applications. J. Alloys Compd., 661, 231-236.

[6]U.N. Roy, G.S. Camarda, Y. Cui, Y. et al., 2021. Impact of selenium addition to the cadmium-zinc-telluride matrix for producing high energy resolution X-and gamma-ray detectors. Sci Rep., 11, 10338.

[7]L. Zhe, C. Gui, L. Bo, Y. Gang et al., 2013. Fabrication of high-quality ZnTe nanowires toward high-performance rigid/flexible visible light photodetectors. Optics Express 21, 6.

[8]T. Tanaka, Y. Kume, M. Nishio, Q. Guo, H. Ogawa, A. Yoshida, 2003. Fabrication of ZnTe Light-Emitting Diodes Using Bridgman-Grown Substrates. Japanese Journal of Applied Physics, 42(Part 2, No. 4A), L362–L364.

[9]K.Z. Yahiya, E.T. Salem et. al., 2008, Optical Constants of Zinc Telluride Thin Films in the Visible and Near-Infrared Regions, Eng. And Tech., 26, 5.

[10] J. Pattar, S.N. Sawant, et. al. 2009.Structural Optical and Electrical Properties of Vacuum Evaporated Indium Doped Zinc Telluride Thin Films, Int. J. Electrochem. Sci., 4, 369 – 376.

[11] A.K. Aqili, Z. Ali, A. Mazsood, et. Al., 2001. Properties of copper-doped ZnTe thin films by immersion in Cu solution. Appl. Surf. Sci., 180, 73–80.

[12] T.A. Gessert, J.N. Duenow, S. Ward, J.F. Geisz, B. To, 2014. Analysis of ZnTe:Cu/Ti contacts for crystalline CdTe. 2014 IEEE 40th Photovolt. Spec. Conf. PVSC 2014, 2329-2333.

[13] W.A. Syed, N.A. Shah, 2015. Cu-doped ZnTe thin films for potential energy applications Chalcogenide Lett., 12, 157.

[14] R. Amutha, 2013. Effect of copper on composition, structural and optical properties of copper doped ZnTe thin films. Adv. Mat. Lett. 4(3), 225-22.

[15] I. Lungu, 2021. Structural and composition of Cu-doped ZnTe thin films with different concentrations by immersion in $Cu(NO_3)_2$ solution. Proceedings of the International Semiconductor Conference (CAS), 155-158.

[16] B. Maiti, P. Gupta, S. Chaudhuri, A.K. Pal, 1994. Grain boundary effect in polycrystalline ZnTe films. Thin Solid Films, 239(1), 104–111.

[17] T. Gessert, T., T.C. RG. Dhere, A. Duda, D. Levi, 2003. ZnTe:Cu Contact Optimization Strategies for Single-Junction and Multijunction CdS/CdTe PV Device Designs. The National Center for Photovoltaics and Solar Program Review Meeting, 1-4.

[18] F. Hanus, M. Wautelet, 1989. Time-resolved temperature measurements during laser-induced synthesis of Cu-Te compounds. Applied Surface Science, 43(1-4), 271–276.

[19] S.W. Pak, D.U. Lee, E.K. Kim, 2014. Oxygen incorporation in ZnTe thin films grown by plasma-assisted pulsed laser deposition. Current Applied Physics, 14, S49–S52. doi:10.1016/j.cap.2013.11.043.

SYNTHESIS AND ELECTROPHYSICAL PROPERTIES OF CdS/ZnTe HETEROJUNCTIONS

Ion Lungu[1], Lidia Ghimpu[2], Lyudmila Gagara[1], and Tamara Potlog[1]

[1] *Moldova State University, str. A. Mateevici 60, Chisinau, MD-2009 Republic of Moldova*
[2] *Ghitu Institute of Electronic Engineering and Nanotechnologies, str. Academiei 3/3, Chisinau, MD-2028 Republic of Moldova*
**E-mail: ionlungu.usm@gmail.com*

(Received September 30, 2022)

https://doi.org/10.53081/mjps.2022.21-1.04

Abstract

In this paper results of studying CdS/ZnTe heterostructures synthesized by the quasi-closed space sublimation method on glass substrates coated with an ITO layer are described. The electrical and photoelectric properties of the structures are studied using current–voltage and capacitance–voltage characteristics in a temperature range of 30–100 °C. Analysis of the experimental data shows that the main specific feature of CdS/ZnTe structures is the formation of a high-resistance transition layer, which affects the separation of carriers at the barrier contact. The current carrier concentration in the space charge region, which is determined from the capacitance–voltage characteristics, is 1×10^{15} cm^{-3}; this fact suggests that one of the contacting materials—ZnTe—exhibits a high resistivity. Measurements of current–voltage characteristics in the solar cell mode give the following photoelectric parameters: open circuit voltage (U_{OC} = 0.53 V, J_{SC} = 27–30 μA/cm^2, and FF = 0.25.

Keywords: quasi-closed space sublimation method, diffraction patterns, current–voltage characteristics, capacitance–voltage characteristics, solar cells.

Rezumat

In aceasta lucrare sunt descrise rezultatele studierii heterostructurilor CdS/ZnTe sintetizate prin metoda sublimării în spațiu cvasi-închis pe substraturi de sticlă acoperite cu un strat de ITO. Proprietățile electrice și fotoelectrice ale structurilor au fost studiate folosind caracteristicile curent–tensiune și capacitate–tensiune în intervalul de temperatură de 30–100°C. Analiza datelor experimentale indică că principala caracteristică specifică a structurii CdS/ZnTe este formarea la interfață a unui strat de tranziție de înaltă rezistență, care afectează separarea purtătorilor de sarcină electrică. Concentrația impurităților purtătorilor ionizați în regiunea de sarcină determinată din caracteristicile capacitate–tensiune, constituie 1×10^{15} cm^{-3}; acest fapt sugerează că unul dintre materialele în contact, și anume ZnTe are o rezistivitate mai ridicată.

Măsurătorile caracteristicilor curent–tensiune în regim de celulă solară arată următorii parametri fotovoltaici: tensiunea de circuit deschis *(*U_{OC})= 0.53 V, densitatea curentului de scurt circuit (J_{SC}) = 27–30 μA/cm^2 și factorul de umplere (*FF)* = 0.25.
Cuvinte cheie: metoda volumului cvasi-închis, difracția de raze X, caracteristica curent–tensiune, caracteristica capacitate–tensiune, celulă solară

1. Introduction

A^2B^6 compounds are widely known as materials exhibiting fairly high photosensitivity for the entire visible spectrum of solar radiation; therefore, most of these compounds are commonly used for designing thin-film solar cells. A distinctive feature of these compounds is their pronounced monopolarity; therefore, these materials are used mostly in the form of heterojunctions. The best known thin-film heterojunction solar cells are those made of CdS/CdTe. However, the possibility of designing other pairs of heterojunction systems based on A^2B^6 compounds and solar cells based on these systems, in particular, CdS/ZnTe, is of interest [1, 3–7]. The theoretically calculated model of a CdS/ZnTe junction [2, 3] for an optimum ZnTe thickness of 2 μm gives an efficiency value of 10%, an open-circuit voltage (U_{OC}) of 1.81 V, and a short-circuit current density (J_{SC}) of up to 7 mA/cm^2 at a current–voltage characteristic (CVC) fill factor of 78.84%. The authors of [3] argue that, in terms of physical parameters, zinc telluride is one of the suitable semiconductors from A^2B^6 compounds for the development of low-cost and high-efficiency thin-film solar power engineering. Since the crystalline perfection of the semiconductor layers that form the structure is not mandatory, inexpensive synthesis techniques can be used. These layers can be formed at lower temperatures than those required for the formation of layered CdTe. Oxygen doping of zinc telluride layers leads to a decrease in the ZnTe band gap to 1.56 eV [7] and thereby makes it a fairly promising material for solar power engineering [8].

2. Synthesis Technique

A technology for synthesizing CdS layers by the quasi-closed space sublimation method was developed earlier for CdS/CdTe junctions. The required thicknesses were determined; the transmission and electrical parameters of the layers were measured [11].

The cadmium sulfide source was a CdS powder with a semiconductor grade purity of 99.9%. The evaporator temperature (T_E) of 590 ℃ provided the required density of the incident atomic flux. The substrate temperature (T_S) was varied in a range of 240–380 ºC; the thickness of the layers was controlled according to the time of formation of the layers and amounted to 0.5–0.7 μm. A CdS layer was deposited on a glass substrate with a thin indium tin oxide (ITO) layer by the quasi-closed space sublimation method. After that, the substrate was transferred to the zone of formation of a ZnTe layer, and a ZnTe layer was deposited also by the quasi-closed space sublimation method. The deposition temperatures for the ZnTe layer were chosen so that to hinder the reevaporation of the CdS layer. Thus, ZnTe layers were formed at T_S = 320 ℃ and T_E = 590 ℃. The thickness of the layer was controlled according to the time of formation, while providing the absence of visible violations of the layer continuity. The thickness of the layer was varied in a range of 4–8 μm. The ohmic contact to the ZnTe layer was made of thin layers of Ag, the work function of which is 4.7 eV; the Ag layers were deposited by vacuum evaporation.

3. Research Results

The crystal structure and phase composition of the films were studied at room temperature on a Bruker D8 X-ray diffractometer using CuK_α radiation (λ = 1.5406 Å, 40 mA, 40 kV) in a 2θ angular range of 10°–90°. The determined interplanar spacing values were compared with the reference values from the database [12]. X-ray diffraction patterns of thin CdS layers deposited on ITO/glass are shown in Fig. 1. The films have a polycrystalline structure, as evidenced by the reflection half-widths that are characteristic of polycrystalline substances. In the above specified range of diffraction angles, ITO peaks, in addition to the CdS peaks, were detected. X-ray diffraction analysis shows that an increase in T_S from 240 to 380 °C leads to a decrease in the intensity of the reflection of the (H102) plane, while the intensity of the line corresponding to the (H002) reflection plane increases. This relationship can indicate a reorientation of the crystals from the preferred (H102) plane to the (H002) plane. Thus, the CdS films are of a hexagonal modification and are textured in the [1002] direction.

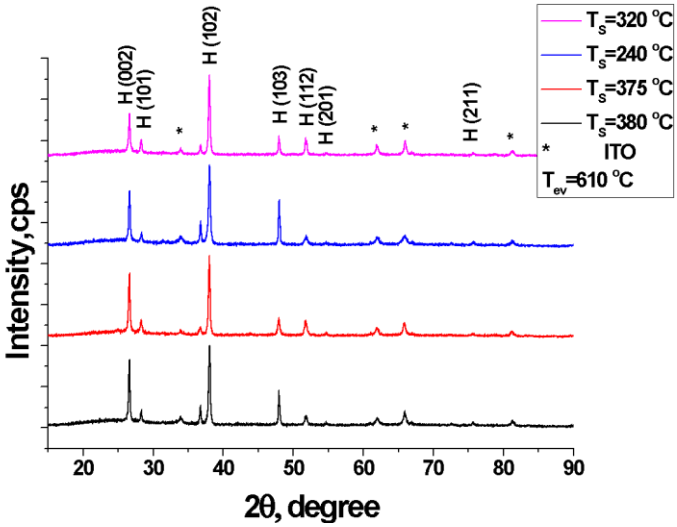

Fig. 1. X-ray diffraction patterns of the CdS/ITO layers.

Table 1 shows the structural characteristics of the CdS films deposited on ITO/glass, which were determined from the intense (H102) peak, and their dependence on T_S. According to the X-ray diffraction theory, the intensity of diffraction reflections is proportional to the square of the crystallite size; however, the reflection half-width is proportional to the first power of the crystallite size. Thus, the decrease in the intensity of the reflections with an increase in the T_S value of the films, to the first approximation, can be attributed to a decrease in the crystallite size, as evidenced by Table 1. The increase in the crystallite sizes slows down at T_S = 380 °C, while lattice strain increase. Lattice strain due to the imperfection and deformation of the crystal was calculated by the following formula:

$$\varepsilon = \frac{\beta_{hkl}}{tan\theta},$$

where β_{hkl} *is* full width at half maximum of diffraction peaks, θ is angle to the diffracting

planes.

The plane spacing equation for the hexagonal structure is:

$$\frac{1}{d^2} = \frac{4}{3}\left(\frac{h^2 + hk + k^2}{a^2}\right) + \frac{l^2}{c^2},$$

where a and c - lattice parameters of the unit cell and hkl - the Miller indices.

According to the published data, the parameters of the hexagonal crystal lattice of the CdS layers are as follows: a = 4.1307 Å, b = 4.1307 Å, and c = 6.7049 Å [2]; these values are in good agreement with the data in Table 1. The results of calculating the diffraction patterns are shown in Table 1.

Table 1. Microstructure parameters of CdS layers grown by the quasi-closed space sublimation method

Substrate temperature, °C	Intensity for the CdS peaks, cps	Crystallite size, Å	Lattice parameters			Lattice strain, ε
			a, Å	*b*, Å	*c*, Å	
240	554	436	4.1307	4.1307	6.7049	0,00413
320	502	329	4.1307	4.1307	6.7049	0,00357
375	413	349	4.1274	4.1274	6.7011	0,00362
380	365	307	4.1336	4.1336	6.7054	0,00377

The structure formed as a result of technological procedures is schematically shown in Fig. 2.

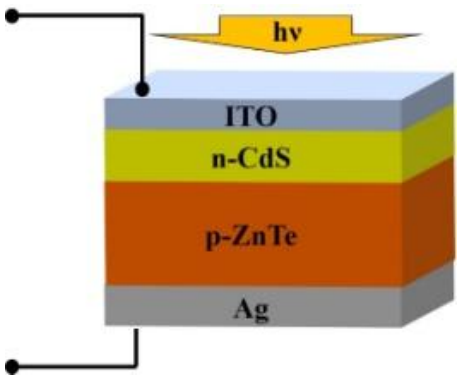

Fig. 2. Schematic representation of the synthesized ZnTe/CdS heterojunction.

The electrophysical properties of the structures formed in the described mode were studied. The CVC measurements in a temperature range of 30–100 °C showed that the current exhibits an exponential dependence on applied voltage in a region of up to 1.6 V (Fig. 3); it can be approximated by the following expression:

$$I = I_0\left(exp\left(\frac{eV}{nkT}\right) - 1\right). \quad (1)$$

where I_o is the reverse current of the *p*–*n* heterojunction, *q* is the electron charge ($q = 1.6 \times 10^{-19}$ C), *k* is the Boltzmann constant ($k = 1.38 \times 10^{-23}$ J deg), and *T* is the temperature (K),

n-ideality factor. A graphical representation of this dependence is shown in Fig. 3a. The CVC exhibits a pronounced nonlinearity, which is responsible for the dependence of the diode resistance on the operating-point position. Thus, a CdS/ZnTe barrier structure was formed. The empirically determined value of the barrier formed in this junction was 0.74–0.64 V for the given temperature range. The area of the measured samples was 0.25–0.4 cm^2.

The CVC was replotted in the ln*I* = *f*(*U*) coordinates (Fig. 3b) to determine the saturation currents in the studied temperature range, which are responsible for the quality of the heterojunction. The saturation current values for the given temperature interval and the change in the contact potential difference with a variation in temperature were empirically determined from ln*I* = *f*(*U*). All the data are summarized in Table 2.

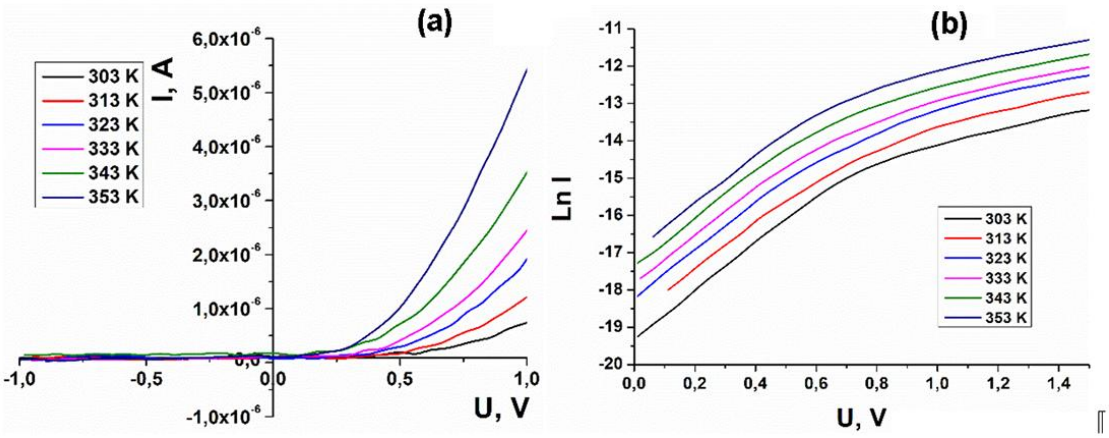

Fig. 3. Current–voltage characteristics of the CdS/ZnTe heterojunctions in a temperature range of 30–80 °C.

Table 2 summarizes the electrical parameters of the CdS/ZnTe structure calculated from the CVCs.

Table 2. Electrical parameters of the CdS/ZnTe structure

T_{meas}, K	I_0, A	U_d, V	*n* (Eq. (1))	R_s, kΩ
303	4.07×10^{-9}	0.74	7.27	560
313	6.98×10^{-9}	0.70	7.21	400
323	1.19×10^{-8}	0.69	6.61	250
333	1.82×10^{-8}	0.66	6.26	180
343	2.95×10^{-8}	0.65	6.22	180
353	4.18×10^{-8}	0.64	6.39	80

The capacitance–voltage methods for measuring the parameters of semiconductors were based on determining the dependence of the capacitance of a structure, which is attributed to the presence of a space charge in the near-surface region of the semiconductor, on the voltage applied to the structure. Capacitance–voltage (*C*–*V*) characteristics of the CdS/ZnTe

heterojunctions were studied in a temperature range of 30–80 °C. All measurements were conducted at a frequency of 1.5 MHz; the sample area was 0.25 cm^2. Figure 4 shows an equivalent circuit of a CdS/ZnTe heterojunction [10].

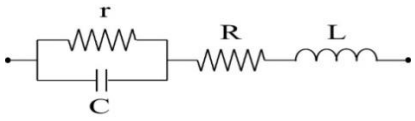

Fig. 4. Equivalent circuit of a CdS/ZnTe heterojunction; here, *r* is the internal resistance of the ZnTe layer; *R* is the series resistance of the entire CdS/ZnTe structure, which includes the contact resistance; *C* is the internal capacitance of the structure; and *L* is the inductance of the structure.

A characteristic feature of the *C–V* characteristics of CdS/ZnTe heterojunctions is the presence of a depletion region in a range of 0.80–0.55 V, after which the curves transit into a saturation region. The appearance of a saturation region in the *C–V* characteristic is typical for the presence of a high-resistance layer at the interface between two semiconductors [13]. The thickness of this transition layer was determined in accordance with the following expression:

$$d = \frac{\varepsilon_0 \varepsilon_{ZnTe} S}{C}, \tag{2}$$

where d is the thickness of the space charge region, ε_0 is the vacuum constant of 8.85×10^{-14} F/cm, $\varepsilon_{ZnTe} = 10.1$ is the dielectric permeability of ZnTe, and S (0.4 cm^2) is the area of the heterojunction. The thickness of this layer was 0.73–0.80 μm depending on measurement temperature. These layer thicknesses in the space charge region indicate the formation of a high-resistance region at the interface between the two semiconductors due to the mutual diffusion of the structure components or broken bonds of the atoms of the contacting materials. The thickness and properties of this layer depend on the technological parameters of the formation of a given structure, the doping level, and the choice of the doping component to decrease the resistance of ZnTe. It is difficult to determine parameters of this layer, because they can be states at the interface between two semiconductors and the resulting boundary states that fix the Fermi level at the interface in the heterojunction.

The replotting of these dependences in the $C^{-2} = f(U)$ coordinates (Fig. 5a) shows the presence of a wide region of a linear dependence of C^{-2} on applied voltage; for this region, a relationship for calculating the ionized impurity concentration in the space charge region can be used; in this case, it is true of the ZnTe component [9], because the calculation of the resistance of the CdS layers during formation showed that their resistivity is 2×10^{-3} to 4×10^{-3} Ω cm. The resistance of the ZnTe layers calculated from the direct CVCs was 2×10^5 to 4×10^5 Ω. This fact suggests that the space charge region is entirely localized in the ZnTe layer:

$$N_{ef} = \frac{2\Delta U}{q\varepsilon_0 \varepsilon_{ZnTe} S^2 \Delta\left(1/C^2\right)}. \tag{3}$$

Figure 5 shows $C^{-2} = f(U)$ dependences of the CdS/ZnTe structures measured at 40 °C (Fig. 5a) and in a temperature range of 30–80 °C (Fig. 5b).

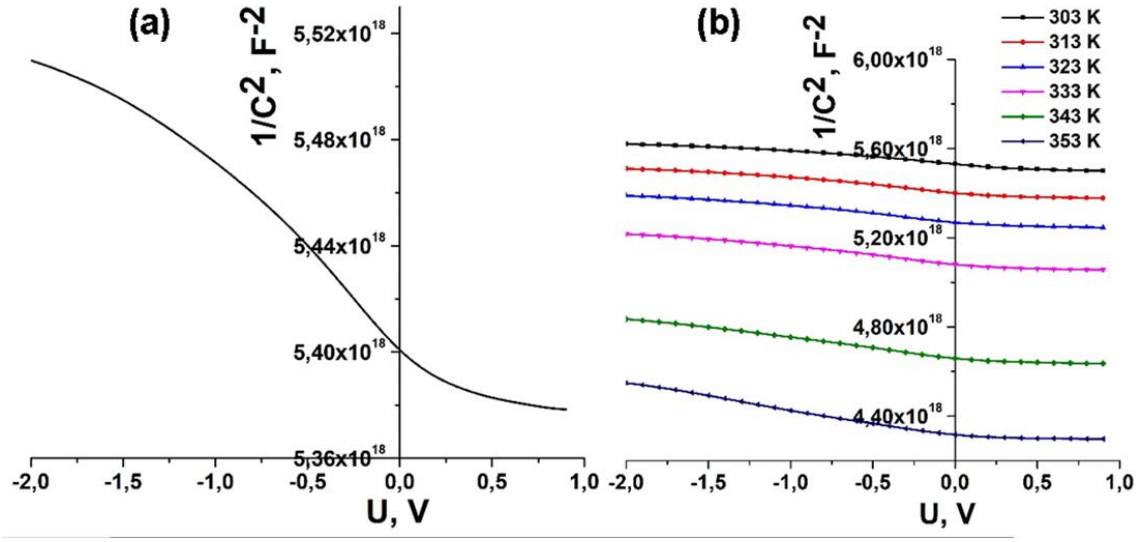

Fig. 5. $C^{-2} = f(U)$ dependences of the CdS/ZnTe heterojunction measured (a) at 40 °C and (b) in a temperature range of 30–80 °C.

According to the calculations, from the $C^{-2} = f(U)$ dependence for a temperature range of 30–80 °C, the ionized impurity concentration in the space charge region of the structure was determined to be 0.61×10^{14} to 1.0×10^{14} cm^{-3}. Low charge carrier concentrations suggest that the ZnTe component of the structure and the transition layer exhibit high resistivity. The contact potential difference value determined from the *C–V* characteristics in this structure was $U_d = 0.68$ V; this value is in good agreement with the values determined from the CVCs.

The structures were irradiated with integral light with an intensity of 100 mW/cm^2. Figure 6 shows that the open-circuit voltage is $U_{OC} = 0.53$ V, while the short circuit current density is $J_{SC} = 27–30$ μA/cm^2. The CVC fill factor is $FF = 0.25$. Low CVC fill factor values also support the conclusion that a high-resistance transition region is formed at the interface between two contacting semiconductors and, together with the high resistance of the heterojunction material, indicate a high series resistance of the entire structure, which, in turn, leads to low energy parameters of this barrier structure.

Table 3. Photoelectric parameters of the CdS/ZnTe heterojunction in the solar cell operating mode

Silver contact	I_{SC}, μA	U_{OC}, V	FF, %	R_S, kΩ	R_{sh}, MΩ
sprayed	12	0.44	14.3	54	80
paste	43	0.53	25.1	30	6

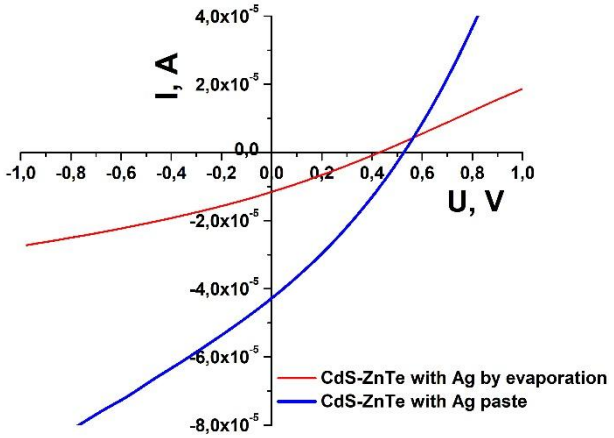

Fig. 6. Current–voltage characteristics of the CdS/ZnTe heterojunction in the solar cell mode.

Based on the results obtained, we assume that CdS/ZnTe is an anisotype heterojunction with an intermediate layer, because to provide the absence of defects in the crystal lattice of the two materials constituting the heterojunction, the materials should at least have an identical crystalline structure and similar lattice constants. Figure 7 shows the energy diagram of a CdS/ZnTe heterostructure in thermodynamic equilibrium, which was constructed in terms of the Donnelly and Milnes model [14].

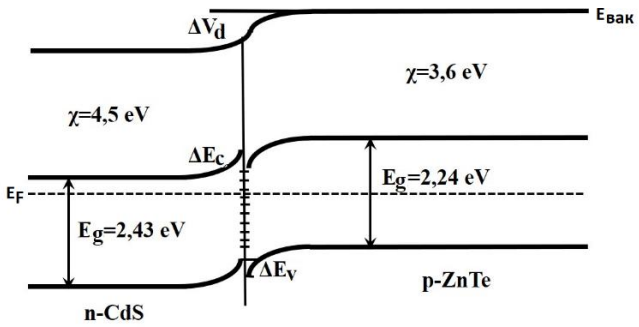

Fig. 7. Assumed energy diagram of a CdS/ZnTe heterojunction in thermodynamic equilibrium.

The composition of the metallurgical layer at the interface between two contacting semiconductors cannot be determined; it can be assumed that this layer is formed due to the diffusion of the ZnTe/CdS heterojunction components.

4. Conclusions

- CdS/ZnTe heterostructures have been synthesized by the quasi-closed space sublimation method.

- The electrical characteristics of the synthesized CdS/ZnTe heterojunction have been studied and their main electrical parameters U_{OC}, I_{SC}, and R_S have been calculated.
- According to the results of studying the *C–V* characteristics, it has been shown that a high-resistance layer is formed at the interface between the CdS and ZnTe layers; this layer, together with the fairly high resistance of ZnTe, is responsible for the low parameters of the structure in the solar conversion mode.
- The energy parameters of the CdS/ZnTe heterojunction have been measured. The low values of the energy parameters are characterized by a high series resistance, the determining role in which is played by both the intermediate layer and the high resistance of ZnTe as the main absorbing component.
- According to the experimental results, an energy diagram of the studied heterojunction has been proposed. Either the composition or the degree of interaction of the formed intermediate layer cannot yet be determined; the only assumption that has been made in this respect is that the thickness and properties of this layer depend on the technological parameters of the synthesis of this structure, the doping level, and the choice of the doping component to decrease the resistance of ZnTe.

Acknowledgments. This work was supported by the research project "Photosensitizers for Photodynamic and Photoelectric Therapy" no. 20.80009.5007.16 and "Advanced nanostructured materials for thermoelectric applications and sensors", no. 20.80009.5007.02.

References

[1] H. Bayad, A. EL Manouni, B. Mari, Y. H. Khattak, S. Ullah, and F. Baig, Opt. Quantum Electron. 50 (6), 1 (2018).
[2] A. Nazar, A. Nawaz, A. Kanwal, and W. Syedc, World Appl. Sci. J. 28 (4), 548 (2013).
[3] O. Skhouni, A. Maouni, B. Mari, and H. Ullah, Eur. Phys. J. App. Phys. 74, 24602p1 (2016).
[4] F. Fisterer and H. Schock, J. Cryst. Growth 59, 432 (1982).
[5] O. Skhouni, A. Manouni, M. Mollar, R. Schrebler, and B. Mari, Thin Solid Films 564, 195 (2014).
[6] W. Wang, A. Lin, and J. Phillips, Appl. Phys. Lett. 95 (1), 011103 (2009).
[7] B. E. Rekhovskaya, I. Nagibina, and A. Makarova, Molod. Uch. 2 (61), 248 (2014).
[8] A. Luque and A. Marti, in Handbook of Photovoltaic Science and Engineering, Ed. by A. Luque and S. Hegedus, John Wiley & Sons, second edition, 2011, pp. 130–168.
[9] A. G. Milnes and D. L. Feucht, Geteroperekhody i perekhody metal-poluprovodnik, Mir, Moscow, 1975 (Heterojunctions and Metal–Semiconductor Junctions, Academic Press, New York, 1972).
[10] J. H. Scofield, Sol. Energy Mater. Sol. Cells 37 (2), 217 (1995).
[11] P. Gashin, L. Gagara, P. Ketrush, I. Inculetz, V. Fiodorov, and Al. Q. Amjad, Mold. J. Phys. Sci. 15 (1–2), 54 (2016).
[12] Powder Diffraction File. Swarthmore: Joint Committee on Powder Diffraction Standards, 1996.
[13] S. M. Sze, Fizika poluprovodnikovykh priborov, Energiya, Moscow, 1973, p. 351 (Physics of Semiconductor Devices, John Wiley & Sons, New York, 1969).

[14] B. Klimov and N. Tsukerman, Geteroperekhody v poluprovodnikakh, Izd. Saratov Gos. Univ., Saratov, 1976.

Information about the authors:

Ion LUNGU, postgraduate student of the Doctoral School of Physical and Engineering Science, researcher at the Laboratory of Organic/Inorganic Materials in Optoelectronics; Moldova State University
E-mail: ionlungu.usm@gmail.com
ORCID: 0000-0002-7117-672X

Lydia GHIMPU, Dr., Director of the Institute of Electronic Engineering and Nanotechnologies of Moldova

Lyudmila GAGARA, Dr., Senior Researcher, Laboratory of Organic/Inorganic Materials in Optoelectronics; Moldova State University
E-mail: lgagara2019@mail.ru

Tamara POTLOG, Assoc. Prof., Dr., Head of the Laboratory of Organic/Inorganic Materials in Optoelectronics; Moldova State University
E-mail: tpotlog@gmail.com
ORCID: 0000-0003-1243-9371

ELECTRON TRANSPORT, TRANSVERSE AND LONGITUDINAL MAGNETORESISTANCE, AND SHUBNIKOV–DE HAAS OSCILLATIONS IN $Bi_{0.83}Sb_{0.17}$ TOPOLOGICAL INSULATOR SEMICONDUCTOR WIRES

Albina A. Nikolaeva[1]*, Leonid A. Konopko[1], Tito E. Huber[2], Ivan A. Popov[1], and Gheorghe Para[1]**

[1]Gitsu Institute of Electronic Engineering and Nanotechnologies, str. Academiei 3/3, Chisinau, MD-2028 Republic of Moldova
**E-mail: a.nikolaeva@nanotech.md*
[2]Howard University, Department of Chemistry, Washington, USA
***E-mail: titoehuber@gmail.com*

(Received June 07, 2022)

https://doi.org/10.53081/mjps.2022.21-1.05

Abstract

The paper describes results of experimental studies of the dependence of the resistance, transverse and longitudinal magnetoresistance, as well as the Shubnikov–de Haas (SdH) oscillations of $Bi_{0.83}Sb_{0.17}$ semiconductor single-crystal wires with diameters of (75–1100) nm, as a function of the thickness, in a temperature range of (3.1–300) K at magnetic fields of up to 14 T. The wires were prepared by liquid-phase casting. It has been found that the temperature dependences of the resistance of wires with d < 0.5 μm have two regions exhibiting a semiconductor and a metallic behavior of the resistance, the two regions being separated by a maximum, which is shifted to the high-temperature region with a decrease in the wire diameter d. It has been revealed that the energy gap ΔE increases by a factor of 2 with a decrease in wire diameter d, due to the occurrence of the quantum size effect. The "metallic" behavior of conductivity is attributed to surface states characteristic of topological insulators, which is most clearly evident in thin wires at temperatures of T < 50 K. It has been shown that, in the presence of a uniform magnetic field H, the field dependences of the longitudinal and transverse magnetoresistance in quasi-one-dimensional systems can undergo a significant change depending on the ratio of quantum wire radius to the magnetic length $R = (ch/eH)^{1/2}$, as well as on the decrease in the mean free path of carriers due to scattering on the wire surface. The SdH oscillation periods exhibit anomalies that are typical neither to bulk $Bi_{1-x}Sb_x$ samples nor to semimetallic wires based on $Bi_{1-x}Sb_x$ alloys. This fact points to the essential role of surface states of topological insulators in 1D-systems, which lead to the occurrence of new effects that are not characteristic of other systems.

Keywords: semiconductor nanowires, topological insulator, size effects, Shubnikov–de Haas oscillations, magnetoresistance

Rezumat

În lucrare sunt prezentate rezultatele studiilor experimentale ale dependențelor de grosime ale rezistenței, magnetoresistenței transversale și longitudinale, oscilațiile Shubnikov de Haas ale firelor monocristaline semiconductoare $Bi_{0.83}Sb_{0,17}$, obținute prin turnarea din fază lichidă cu diametre de (75-1100) nm în intervalul de temperaturi (3,1-300) K și câmpuri magnetice de până la 14T. S-a constatat, că dependențele de temperatură ale rezistenței firelor cu diametrul d < 0,5 μm au 2 zone (una cu comportament semiconductor și alta cu comportament metalic al rezistenței), ele fiind separate de un maximum, care se deplasează spre zona temperaturilor ridicate cu micșorarea diametrului firelor d. S-a stabilit, că gapul energetic ΔE crește de 2 ori odată cu micșorarea diametrului firelor d, ca urmare a apariției efectului de confinare cuantică, iar comportamentul „metalic" al conductivității se datorează stărilor de suprafață caracteristice pentru izolatorii topologici, care se manifestă cel mai clar în firele subțiri la temperaturi de T < 50K. Se arată, că dependențele de câmp ale magnetoresistenței longitudinale și transversale în sistemele cvasi-unidimensionale în prezența unui câmp magnetic uniform H se pot schimba semnificativ în funcție de raportul dintre raza firului cuantic către lungimea magnetică $R=(ch/eH)^{1/2}$, precum și de micșorarea parcursului liber al purtătorilor datorită împrăștierii pe suprafața firului. Perioadele oscilațiilor ShdH au anomalii, care nu sunt tipice atât pentru mostrele masive de $Bi_{1-x}Sb_x$, cât și pentru firele semimetalice pe bază de aliaje $Bi_{1-x}Sb_x$, ceea ce indică rolul semnificativ al stărilor de suprafață în izolatorii topologici în sistemele-1D, care conduc la noi efecte și nu sunt caracteristice altor sisteme.

Cuvinte cheie: nanofire semiconductoare, izolator topologic, efecte de confinare dimensională, oscilații Shubnikov–de Haas, magnetorezistență.

1. Introduction

$Bi_{1-x}Sb_x$ alloys are a unique material, interest in which has not faded for decades; in recent years, due to the discovery of a topological phase in condensed media [1–3], interest in semiconductor alloys has increased. A topological insulator (TI) is an insulator that is characterized by the presence of a metallic state on the surface. The conductive properties of the surface are a consequence of the spin–orbit interaction, which leads to the appearance of spin-split topological surface states with Dirac-type dispersion, i.e., a linear dependence of energy on momentum $E = hkv_F$. Surface states inside a bulk band gap with a linear dispersion law have been first observed for $Bi_{1-x}Sb_x$ semiconductor alloys using angle-resolved photoelectron spectroscopy [4]. In recent years, a large number of studies on TIs, in particular, $Bi_{1-x}Sb_x$ semiconductor alloys, have been reported [5, 6]. Most of the studies have been focused on bulk samples. $Bi_{1-x}Sb_x$ alloys are narrow-gap semiconductors with a smooth transition from the semimetallic to semiconductor state [7] and a maximum energy gap of ΔE = 21 meV near 17–18 at % Sb. A schematic rearrangement of the energy spectrum of $Bi_{1-x}Sb_x$ alloys is shown in Fig. 1.

Of particular interest are studies of the properties of TIs for objects, in which the band gap ΔE can be changed due to the quantum size effect [8–10], while changing the film thickness or the wire diameter, rather than due to a variation in the alloy composition.

These studies require single-crystal samples having different diameters and a certain crystallographic orientation. A significant change in the band gap ΔE occurs for diameters

$d < 0.5$ μm.

This paper describes studies of the magnetotransport properties of $Bi_{0.83}Sb_{0.17}$ single-crystal wires prepared by liquid-phase casting in a temperature range of 3.1–300 K at magnetic fields of up to 14 T. In these wires having different diameters, on the one hand, the size quantization effect takes place and, on the other hand, the presence of TI surface states leads to significant features of the temperature dependences of the resistance, longitudinal (LMR) and transverse magnetoresistance (TMR), their angular dependences, and Shubnikov–de Haas (SdH) oscillations.

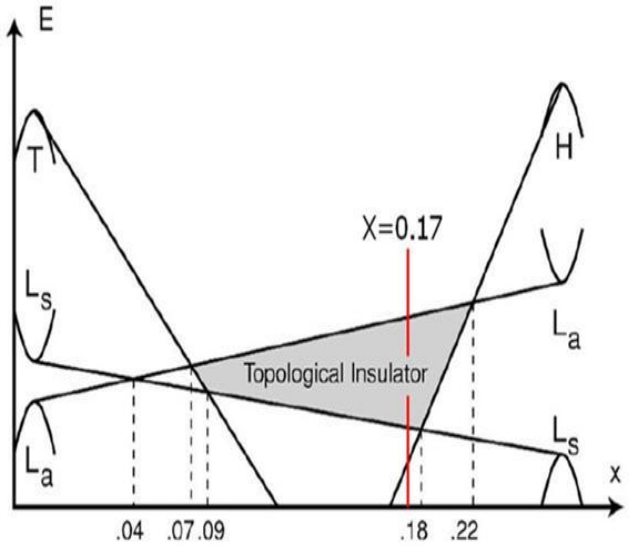

Fig. 1. Schematic rearrangement of the band structure of $Bi_{1-x}Sb_x$ as a function of x ($0 \le x \le 0.25$) at 4.2 K. The arrow shows the composition of the studied wires.

2. Experimental

Glass-insulated $Bi_{0.83}Sb_{0.17}$ wires with a thickness of 75 nm to 1 μm were prepared by liquid-phase casting in accordance with the Ulitovsky method [12–14]. Studies on a scanning electron microscope showed that the samples had a strictly cylindrical shape. The monocrystallinity and crystallographic orientation of the wires were determined using X-ray rotation diffraction patterns. Both pure Bi wires and Bi–17at%Sb wires of all studied diameters had the (1011) orientation along the wire axis (Fig. 2a) [12–14].

The C_1 bisector axis is deviated by an angle of 19° from the wire axis, while the C_2 binary axis is strictly perpendicular to the wire axis (Fig. 2), as confirmed by the rotation diagrams of TMR in a magnetic field of 14 T at 4.2 K.

The measurements were conducted by the two-probe method. The solder was the InGa eutectic; at 300 K, it is in a liquid state and readily wets the wire edges to provide the ohmicity of the contacts. Figure 3 shows a glass-insulated wire on a substrate with InGa contacts at the edges. The ohmicity of contacts at 300 and 4.2 K was controlled by measuring the current–voltage characteristics. The resistivity of the wires of all studied diameters (75–1100 nm) at 300 K was 135×10^{-6} Ω cm within the measurement error.

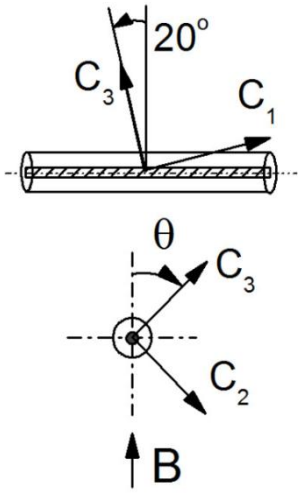

Fig. 2. (a) Schematic representation of a glass-insulated wire and the direction of the crystallographic axes with respect to the wire axis and (b) the direction of rotation of the magnetic field in a plane perpendicular to the wire axis.

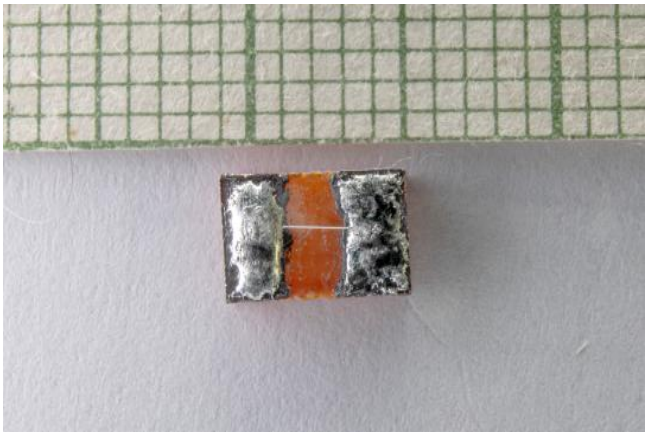

Fig. 3. A glass-insulated $Bi_{0.83}Sb_{0.17}$ wire on a substrate with two InGa eutectic contacts.

The rotation diagrams of TMR and magnetic field dependences in perpendicular ($H \perp I$) and parallel magnetic fields were studied in the field of a superconducting solenoid in magnetic fields of up to 14 T at temperatures of 4.2–300 K using a special rotary device. The device made it possible to rotate the sample in a magnetic field in different planes with respect to the wire axis, while adjusting the angle of deviation from the wire axis in certain crystallographic directions.

The rotation diagrams of TMR are identical for wires of all the diameters and coincide with the respective rotation diagrams of the TMR of bulk samples [5, 6], being different only in quantitative values; this fact confirms the same crystallographic orientation of the wires of all the studied diameters. The MR anisotropy increases with an increase in wire diameter *d*. Measurements in strong magnetic fields (up to 14 T) in a temperature range of 1.3–300 K were conducted in a superconducting solenoid. The MR of $dR/dH(H)$ derivatives of SdH oscillations in

magnetic fields of up to 14 T were studied at the International Laboratory of High Magnetic Fields and Low Temperatures (Wroclaw, Poland).

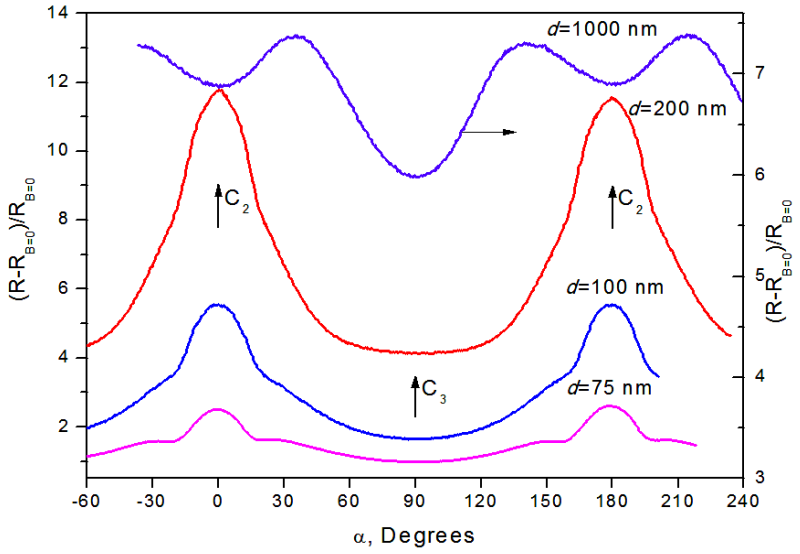

Fig. 4. Rotation diagrams of the TMR $\Delta R/R_0(\alpha)$ at T = 1.5 K and H = 14 T for $Bi_{0.83}Sb_{0.17}$ wires with the different diameters.

3. Results and Discussion

Temperature dependences of the relative resistance $R_T/R_{300}(T)$ of wires with the different diameters in a temperature range of 4.2–300 K are shown in Fig. 5. Unlike the case of pure Bi wires [11, 12], the resistance of the wires at 4.2 K increased with an increase in diameter d. The $R_{4.2}$ /$R_{300}(d^{-1})$ dependence is linear; it exhibits two slopes and an inflection point at d = 350–400 nm (inset in Fig. 5).

With a decrease in temperature from 300 to 80 K, the resistance increased with a decrease in wire diameter d. Thus, the following two regions are clearly observed in the temperature dependences of the resistance of the wires with d < 500 nm: (i) 300–80 K with a semiconductor behavior of $R(T)$, where the resistance increases with a decrease in d, and (ii) 70–4.2 K, where the resistance decreases with a decrease in wire diameter d and exhibits a "metallic" behavior of conductivity $R(T)$. The regions are separated by a maximum in $R(T)$ (Fig. 6a). The position of the maximum R_{max} linearly depends on wire diameter d (insert in Fig. 6a).

In a temperature range of 40–300 K, the $R_T/R_{300}(T)$ dependences have exponential portions with $\rho_T = \rho_0 * \exp(\Delta E/2k_0T)$ dependences, the slope of which increases with a decrease in wire diameter d. The ΔE value calculated for wires with the different diameters is shown in Fig. 6b. For the wires with d = 1000 nm, ΔE= 21 meV, which is consistent with the values obtained for bulk $Bi_{1-x}Sb_x$ samples of an identical composition. With a decrease in the wire diameter, the ΔE value increases in accordance with the following law: $\Delta E \sim 1/d$; for the wires with d = 75 nm, it is 45 meV, i.e., two times higher than that in bulk samples and in the wires with d = 1100 nm.

The $\Delta E \sim 1/d$ dependence suggests that the increase in the energy gap ΔE is attributed to

the quantum size effect [8], which is observed in both pure Bi wires and semimetallic $Bi_{1-x}Sb_x$ wires [11–13].

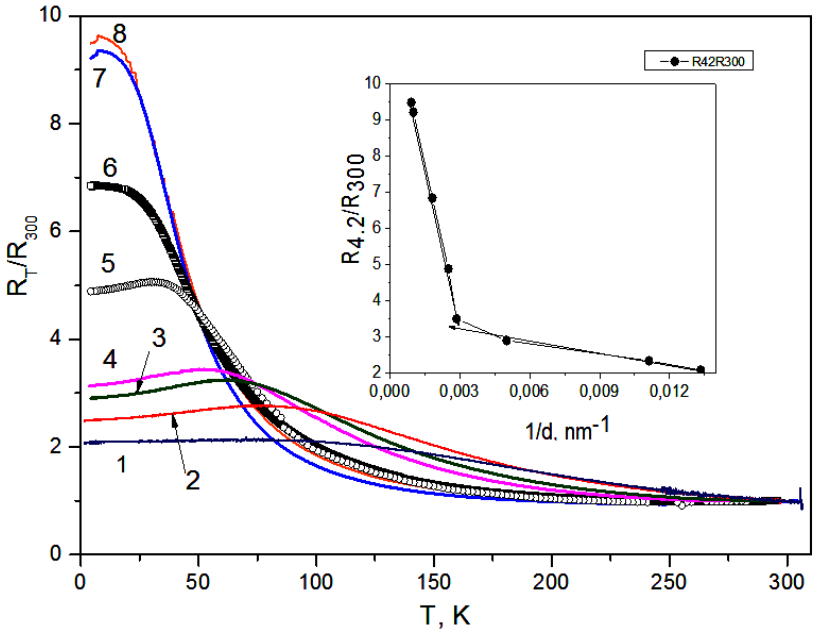

Fig. 5. Temperature dependences of relative resistance $R_T/R_{300}(T)$ for Bi–17at%Sb wires with the different diameters: d = (*1*) 75, (*2*) 100, (*3*) 200, (*4*) 350, (*5*) 450, (*6*) 550, (*7*) 900, and (*8*) 1100 nm.

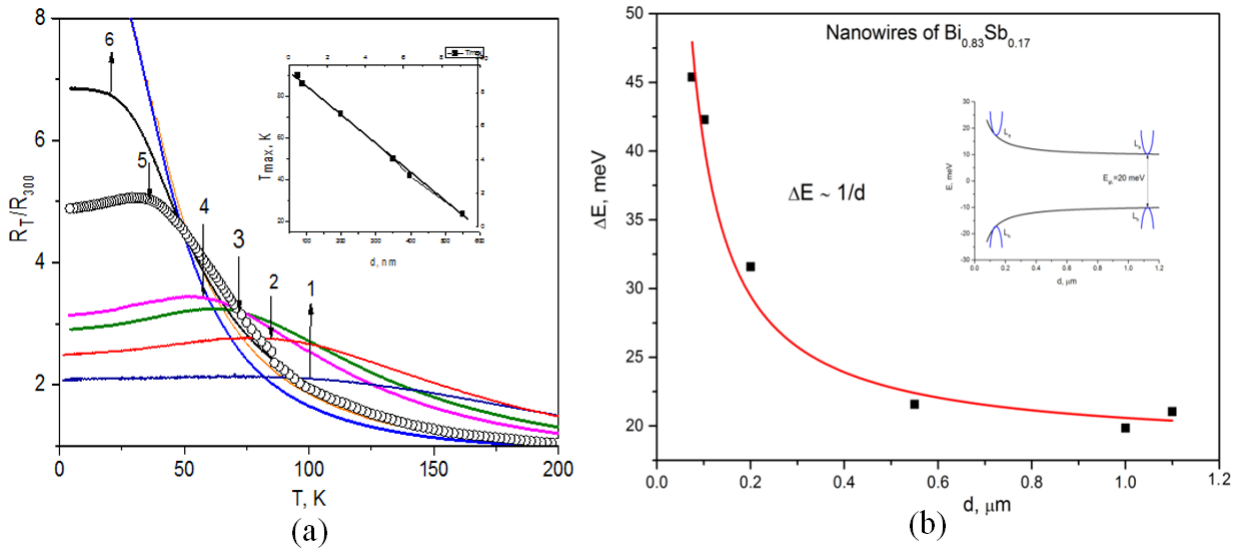

Fig. 6. Temperature dependences of relative resistance $R_T/R_{300}(T)$ in a temperature range of 50–300 K for Bi–17at%Sb wires with the different diameters: d = (*1*) 75, (*2*) 100, (*3*) 200, (*4*) 350, (*5*) 450, (*6*) 550, (*7*) 900, and (*8*) 1100 nm (vertical arrows indicate the position of maxima T_{max} in $R_T/R_{300}(T)$). Inset: (a) the dependence of the T_{max} value in the $R_T/R_{300}(T)$ temperature dependence and (b) the dependence of energy gap ΔE on wire diameter d calculated from the $R(T)$ = exp ($\Delta E/2K\,T$) dependence.

At temperatures of $T < T_{max}$, the $R(T)$ dependence of the wires with $d < 0.5$ μm undergoes

a significant change, namely, a transition from the semiconductor to metallic behavior, which represents the effect of surface states characteristic of TIs. The result is an overall increase in resistance $R_{4.2}/R_{300}(d)$ with an increase in d, which is associated with a decrease in the role of surface states in the wires with an increase in wire diameter d.

4. Magnetoresistance

The LMR ($H \parallel I$) and TMR ($H \perp I$) of Bi–17at%Sb wires with the different diameters were studied at $H \parallel C_3$ and $H \parallel C_2$ in magnetic fields of up to 14 T at temperatures of T = 4.2 K. Figure 7 shows dependences of the LMR of wires with the different diameters.

As in the case of pure Bi wires, $R_H/R_0(H)$ has a maximum followed by a region of negative MR. The H_{max} value is linearly shifted to the region of stronger magnetic fields with a decrease in wire diameter d; this fact indicates the occurrence of a galvanomagnetic size effect [15].

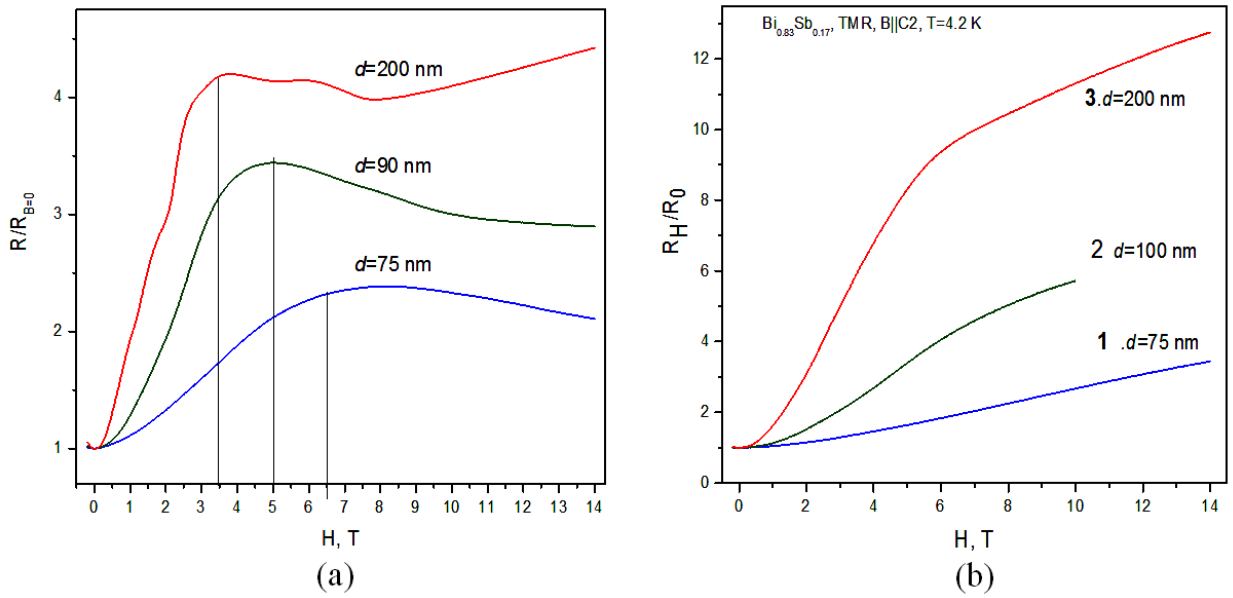

Fig. 7. Field dependences of (a) LMR ($H \parallel I$) and (b) TMR ($H \perp I$ and $H \parallel C_2$) $R_H/R_0(H)$ at 4.2 K for wires with the different diameters.

According to the galvanomagnetic size effect, $H_{max} = D_{max}\, c/ed$, where D_{max} is the maximum diameter of the extreme cross section of the Fermi surface. For pure Bi wires, $D_{max} = 2.2 \times 10^{-21}$ (T cm)/s is the maximum diameter of the extreme cross section of the Fermi surface at point L for two electron ellipsoids localized symmetrically with respect to the bisector–trigonal plane containing the wire axis. For the $Bi_{0.83}Sb_{0.17}$ semiconductor wires described in this paper, $D_{max} = 8.9 \times 10^{-21}$ (T cm/s), which is four times higher than the D_{max} value in pure bismuth and two times higher than that in Bi–8at%Sb wires [16]; this fact is apparently attributed to the presence of cross sections of the Fermi surface of surface states.

In a transverse magnetic field $H \parallel C_2$ (Fig. 7b), the MR of the wires increases with an increase in diameter d in the entire magnetic field range; for the wire with d = 200 nm at H = 14 T, it is four times higher than the value for the wire with d = 75 nm; this fact is associated

with the occurrence of the classical size effect [16].

Figure 8a shows dependences of the relative MR $R_H/R_0(H)$; dependences of the $dR/dH(H)$ derivative for the $Bi_{0.83}Sb_{0.17}$ wire with d = 200 nm at 4.2 K are shown in Fig. 8b.

In weak magnetic fields (H < 2 T), the LMR exceeds the TMR (inset in Fig. 8a); in a magnetic field of 14 T, at $H \parallel C_2$ binary axis, the TMR is four times higher than the LMR.

The $R_H/R_0(H)$ MR derivatives exhibit SdH oscillations, the amplitude of which increases with an increase in magnetic field H. To determine the SdH oscillation period, dependences of the quantum number of SdH oscillations $n(H^{-1})$ were plotted for three directions of the magnetic field (inset in Fig. 8b).

In magnetic fields of H < 1.5 T, SdH oscillations are observed at $H \parallel C_1$ (LMR) and $H \parallel C_3$ with maximum SdH periods of $\Delta_3(H^{-1}) = 0.5$ and 1 T^{-1}, respectively. In magnetic fields of H > 4 T, the calculated SdH oscillation periods for three directions of the magnetic field are minimal; they are $\Delta_1(H^{-1}) = 0.05$ T^{-1} for both $H \parallel C_1$ (LMR) and $H \parallel C_3$. Thus, the maximum SdH oscillation frequency $F = 1/\Delta$ was 18–20 T for both $H \parallel C_2$ and $H \parallel C_3$ in magnetic fields of H > 3 T. The minimum period $\Delta_1(H^{-1}) = 0.014$ T^{-1} was observed at $H \parallel C_2$ in stronger magnetic fields (H > 3 T).

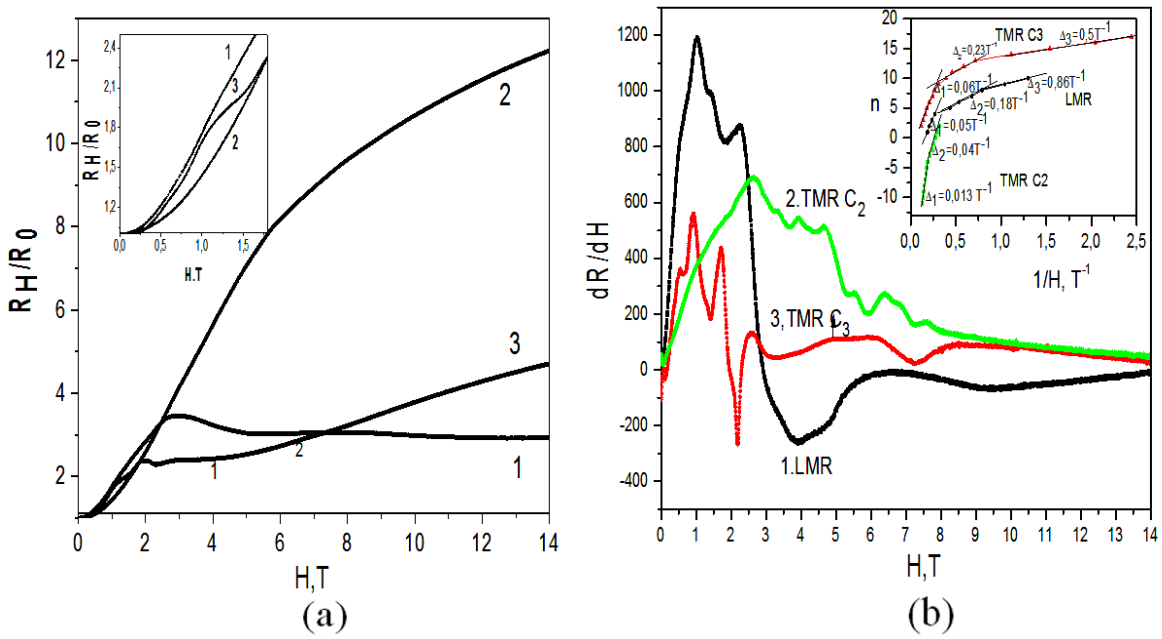

Fig. 8. (a) Field dependences of the LMR (H || I) and TMR (H ⊥ I) R_H/R_0(H) for a Bi–17at%Sb wire with d = 200 nm at 4.2 K: (1) H || I, (2) H ⊥ I, H || C_2, and (3) H || C_3; the inset shows the initial portion of the curves up to 2 T; (b) dR/dH(H) derivatives of curves (1)–(3); the inset shows the dependence of quantum number n of SdH oscillations on H^{-1}.

Comparison of the SdH oscillation periods with respective values obtained for bulk $Bi_{0.91}Sb_{0.09}$ samples [5, 6] shows a significant difference in the periods for all directions of the magnetic field. The (H^{-1}) < 0.5 T^{-1} values in bulk samples were obtained only at $H \parallel C_3$ (±30°); the maximum values of the periods of Δ = 1.7 and 1.5 T^{-1} were observed at $H \parallel C_2$ and $H \parallel C_3$, respectively. This significant difference in the SdH oscillation frequencies can be attributed to the specific features of the manifestation of surface states in low-dimensional 1D TI structures,

which lead to the appearance of new cross sections of the Fermi surface, an unambiguous interpretation of which requires further studies, in particular, those on the angular dependences of SdH oscillations and on SdH oscillations for wires with large diameters.

5. Conclusions

A comprehensive study of the thickness dependences of resistance, TMR, LMR, and SdH oscillations in $Bi_{0.83}Sb_{0.17}$ single-crystal semiconductor wires with diameters of 75–1000 nm has shown the following: the occurrence of the quantum size effect, that is, an increase in the energy gap with a decrease in wire diameter d ($\Delta E \sim 1/d$); the presence of surface states, that is, a metallic behavior of the temperature dependence of the resistance at low temperatures in thin wires; the occurrence of the classical size effect, that is, a negative LMR, a maximum in the LMR exhibiting a linear dependence on wire diameter d, and a decrease in the TMR with a decrease in the wire diameter. The considerable difference of the SdH oscillation periods from the values observed for bulk samples suggests that the surface states of TIs in low-dimensional 1D-structures play a significant role and lead to the occurrence of new effects that are not typical of bulk samples and require further studies for an unambiguous interpretation.

Acknowledgments. This work was financially supported by the State Program of the Ministry of Education, Culture, and Innovation of the Republic of Moldova (project no. 20.80009.5007.02) and the following American foundations: NSF through STC CIQM 1231319, the Boeing Company, and the Keck Foundation.

References

[1] J. E. Moore, Nature 464, 194 (2010).
[2] R. Takahashi and S. Marakami, Nature 460, 1101 (2009).
[3] D. Hsieh et al., Nature 460, 1101 (2009).
[4] D. Hsich, L. Wray, E. Xia, et al., Nature 452, 1226 (2008).
[5] A. Taskin, K. Segawa, and Y. Ando, Phys. Rev. B 82, 121302(R) (2010).
[6] A. Taskin and Y. Ando, Phys. Rev. B 80, 085303 (2009).
[7] G. F. Mironova, M. V. Sudakova, and Ya. G. Ponomarev, Zh. Eksp. Teor. Fiz. 76 (5), 1 (1980).
[8] S. Tang and M. S. Dresselhaus, Phys. Rev. B 89, 045424-1 (2014).
[9] J. E. Cornett and O. Rabin, Appl. Phys. Lett. 98, 182104-1 (2011).
[10] S. Tang and M. S. Dresselhaus, Nano Lett. 12(4), 2021 (2012).
[11] N. B. Brandt, D. V. Gitsu, A. Nikolaeva, and Ya. G. Ponomarev, Zh. Eksp. Teor. Fiz. 45(6), 1226 (1977).
[12] A. Nikolaeva, T. E. Huber, D. V. Gitsu, and L Konopko, Phys. Rev. B 77(3), 035422/1 (2008).
[13] A. Nikolaeva, L. Konopko, Ig. Gherghishan, K. Rogacki, P. Stachowiak, A. Jezowski,. V. Shepelevich, V. Prokoshin, and S. Gusakova, Semiconductors 53(5), 657 (2019).
[14] A. Nikolaeva, L. Konopko, T. E. Huber, J.-Ph. Anserment, and I. Popov, J. Nanoelectron. Optoelectron, 7(7), 671 (2012).
[15] R. G. Chambers, Proc. R. Soc. London, A 202, 378 (1950).
[16] A. Nikolaeva, I. Popov, L. Konopko, E. Moloshnik, T. E. Huber, and P. Bodiul, J. Electron. Mater. 36(2), 1 (2012). doi: 10.1007/s11664-012-2090-x

HYDROTHERMAL PREPARATION OF OXIDE (Ga_2O_3, ZnO, TiO_2) AND DERIVATIVE NANOPARTICLES

E. Rusu[1], V. Morari[1], T. Guțul[1], V. Ursaki[2], and P. Vlazan[3]

[1]National Center for Materials Study and Testing, Technical University of Moldova, 2004 Chisinau, Moldova
[1]Institute of Electronic Engineering and Nanotechnologies "D. Ghitu", 2028 Chisinau, Moldova
[1]National Center for Materials Study and Testing, Technical University of Moldova, 2004 Chisinau, Moldova
[3]National Institute for Research and Development in Electrochemistry and Condensed Matter, Timisoara, 300569, Romania

https://doi.org/10.53081/mjps.2022.21-1.06

Abstract

A brief review of our recent research on preparation and characterization of oxide nanoparticles and their derivatives by hydrothermal growth is presented. A series of Ga_2O_3, ZnO, and TiO_2 nanoparticles, as well derivative nanomaterials including GaN nanowires and ZnO/TiO_2 nanocompostes have been prepared. Ga_2O_3 and ZnO nanopowders have been produced using metal nitrate hydrates as precursors, while Titanium isopropoxide was used for preparation of TiO_2 nanopowders. GaN nanowires have been produced by nitridation of Ga_2O_3 nanomaterials. The produced nanomaterials have been characterized scanning electron microscopy (SEM), X-ray diffraction (XRD) analysis and Fourier transform infrared (FTIR) spectroscopy. Ga_2O_3 nanoparticles doped with Eu^{3+} ions have been characterized by photoluminescence spectroscopy in order to assess their prospects in developing nanophosphors materials.

Keywords: hydrothermal synthesis; precursors; nanopowders; nanowires; crystal structure; vibration modes; photoluminescence; nanophosphors.

Rezumat

A brief review of our recent research on preparation and characterization of oxide nanoparticles and their derivatives by hydrothermal growth is presented. A series of Ga_2O_3, ZnO, and TiO_2 nanoparticles, as well derivative nanomaterials including GaN nanowires and ZnO/TiO_2 nanocompostes have been prepared. Ga_2O_3 and ZnO nanopowders have been produced using metal nitrate hydrates as precursors, while Titanium isopropoxide was used for preparation of TiO_2 nanopowders. GaN nanowires have been produced by nitridation of Ga_2O_3 nanomaterials. The produced nanomaterials have been characterized scanning electron microscopy (SEM), X-ray diffraction (XRD) analysis and Fourier transform infrared (FTIR) spectroscopy. Ga_2O_3 nanoparticles doped with Eu^{3+} ions have been characterized by photoluminescence spectroscopy in order to assess their prospects in developing nanophosphors materials.

Cuvinte cheie: sinteză hidrotermală; precursori; nanopulbere; nanofire; structură cristalină; moduri de vibratie; photoluminescență; nanofosfori.

1. Introduction

Hydrothermal method is one of the most suitable techniques in the growth of a wide range on nanomaterials and nanocomposites, because it requires moderate synthesis temperature, it is low-cost, simple and environmental friendly [1]. At the same time, the hydrothermal process ensures obtaining of particles with reduced agglomeration, narrow particle size distribution, good phase homogeneity and controlled particle morphology and structure with high reproducibility [2,3]. These nanostructures parameters can be tuned by a variation of the temperature, pressure, reaction time, nature, and concentration of precursors in solutions [4].

Among nanomaterials prepared by hydrothermal method, metal oxide materials are widely present, and nitrate hydrates are among the preferred precursors used in their synthesis [5].

Metal nitrate hydrates with Zn, Mn, Fe, Ce, Y. Co, Al, Eu, Cu, etc have been employed in hydrothermal synthesis of nanomaterials [5]. Metal oxides form different compounds and crystalline structures, which properties could vary widely from insulators to superconductors, resulting in a wide variety of potential applications [6]. Particularly, $Ga(NO_3)_3 \cdot nH_2O$ and $Zn(NO_3)_3 \cdot nH_2O$ were used for the production of gallium oxide (Ga_2O_3) and zinc oxide (ZnO) nanostructures. The combination of these two metal nitrate hydrates proved to be very efficient in doping ZnO nanostructures with Ga over a broad range of concentrations [7].

Many oxide-based electrocatalysts, including Ga_2O_3 nanostructures have been used for water splitting and removal of volatile organic compounds [8-10]. Apart from that, Ga_2O_3 nanostructures have been demonstrated in applications such as gas sensors, solar cells, photodetectors and other optoelectronic applications due to their wide bandgap energy and good luminescence properties [11-13].

ZnO is another materials widely employed in nanostructures prepared by hydrothermal synthesis, which are used in photocatalysis, energy harvesting and electronics, due to unique properties including high surface to volume ratio, nontoxicity, biocompatibility, chemical and photochemical stability, optical transparency, and electrochemical activity [3,14]. Apart from that, ZnO nanoparticles are used in textiles due to their UV blocking properties, in sterilizing surroundings due to their antibacterial and antifungal activities, in cosmetics, food packaging, and biomedical applications [4,15].

ZnO material is also considered a preferred alternative to TiO_2 in some applications, including those of electron transport layer in perovskite solar cell, because it possesses energy levels and physical properties similar to those of TiO_2, but requires lower temperatures for processing from solutions to achieve structures of different morphologies [16]. TiO_2 requires high processing temperature to achieve highly crystalline layers. In spite of that, TiO_2 is an important material for applications in solar cells, ultra-thin capacitors, optical devices, gas and chemical sensors, biomedical and self-cleaning coatings, and photocatalysis [2-19]. Apart from that, TiO_2 is widely used as pigment in paints, printing inks, cosmetics, papers, plastics, rubber etc. [20,21].

Various precursors were proposed for producing TiO_2 nanostructures by hydrothermal synthesis [21], including titanium butoxide ($Ti(OBu)_4$) [2,18,22,23,24], titanium tetrachloride ($TiCl_4$) [20], titanium tetraisopropoxide (TTIP) [17], and TiO_2 powders including Degussa P25 [19,25].

Apart from monophasic nanomaterials, composite nanostructures have been recognized as

important materials for a series of applications. TiO_2 nanorods decorated with CeO_2 nanoparticles have been produced by hydrothermal synthesis with titanium butoxide precursor, and their UV filtering applications have been demonstrated [23]. A Ga_2O_3/TiO_2 nanocomposite has been prepared with Ga $(NO_3)_3 \cdot H_2O$ and $TiCl_3$ precursors as efficient photocatalyst with excelent bio-compatibility, demonstrated particularly with respect to the Human embryonic kidney. The anti-bacterial activity against bacillus subtilis and staphylococcus aureus of this composite was demonstrated [26].

In this paper, we present a brief review of our research on preparation and characterization of oxide nanoparticles and their derivatives by hydrothermal growth.

2. Experimental

Since, according to literature data, metal nitrate hydrates are the most preferred precursors in hydrothermal synthesis of nanomaterials, the research in this paper was focused on using $Ga(NO_3)_3 \cdot 9H_2O$ and $Zn(NO_3)_3 \cdot 6H_2O$ in the hydrothermal preparation of Ga_2O_3 and ZnO nanoparticles, respectively. 2.5M high purity gallium nitrate or zinc nitrate from Sigma-Aldrich was dissolved in 50 ml of distilled water, and the pH of the solution was adjusted to the value of 9 by means of the 1M NaOH solution under vigorous magnetic stirring. The solutions were subsequently transferred in a teflon autoclave with a steel shell and treated for several hours at the temperature of 220 ^oC. After autoclaving the nanopporticles were separated by settling and filtering with a subsequent drying in an oven during 2 hours at 80^oC. Titanium isopropoxide was used as precursor for the preparation of TiO_2 nanoparticles. 2 mL of this precursor was added to a solution composed of 0.2g of polyvinyl alcohol and 50 ml of ethanol. The mixture was stirred during 1 hour and introduced subsequently into an autoclave, where it was treated at 220 ^oC during 2 hours. After autoclaving the nanopporticles were separated by settling and filtering with a subsequent drying in an oven during 2 hours at 80^oC.

The morphology and chemical composition microanalysis of the produced films were studied using a TESCAN TS 5130MM scanning electron microscope equipped with tools for energy dispersive X-ray analysis (EDX). X-ray diffraction (XRD) measurements were carried out using the PANalytical X'Pert Pro MPD diffractometer with CuKα radiation (λ = 1.54 Å). Fourier transform infrared (FTIR) spectra were measured with a spectrometer from Perkin Elmer. The PL spectra were excited by the 405 nm line of a mercury lamp at room temperature, and measured with a SDL-1 spectrometer.

3. Results and Discussion

The scanning electron microscope (SEM) image of powders produced with a 5 hours hydrothermal process is shown in Fig. 1. One can see that the morphologies of the obtained powders are quite different. The TiO_2 powder is composed of spherical nanoparticles with sizes from several hundreds of nanometers to 1 μm. The morphology of the ZnO powder is more complex, it consisting of nanoparticles with sizes of (100 – 200) nm agglomerated in formations of several micrometers. The Ga_2O_3 powder represents elongated nanoparticles with the length up to 1 μm and the transversal dimensions around several hundreds of nanometers.

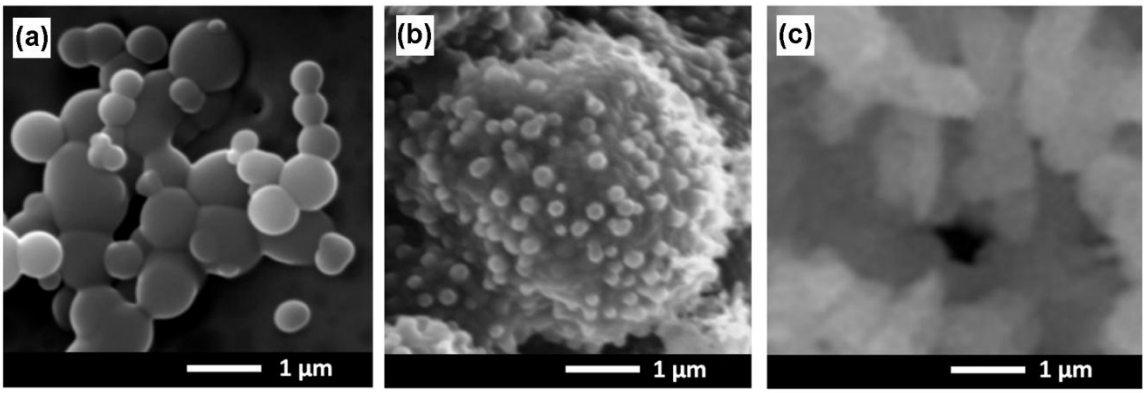

Fig. 1. SEM images of TiO_2 (a), ZnO (b), and Ga_2O_3 (c) powder produced with 5 hours hydrothermal process.

With increasing of the duration of the hydrothermal process from 5 hours to 24 hours, the elongated Ga_2O_3 nanoparticles are transformed into nanowires with the length of several tens of micrometers as illustrated in Fig. 2b.

Apart from oxide nanoparticles, derivative structures have been prepared. GaN nanowires have been produced from Ga_2O_3 nanocrystals. The transformation of the Ga_2O_3 nanowires into GaN ones was performed in a horizontal tube furnace with a quartz boat under flowing ammonia with a subsequent nitridation in a mixture of NH_3 and H_2 with flow rates of 0.35 and 2.5 l/min, respectively. The quartz boat was heated at temperature of 900-950 ^oC during 90-150 minutes, and cooling down occurred in a natural fashion after the furnace was switched off. The initial morphology of Ga_2O_3 nanowires was preserved upon their transformation into GaN, as illustrated in Fig. 2c.

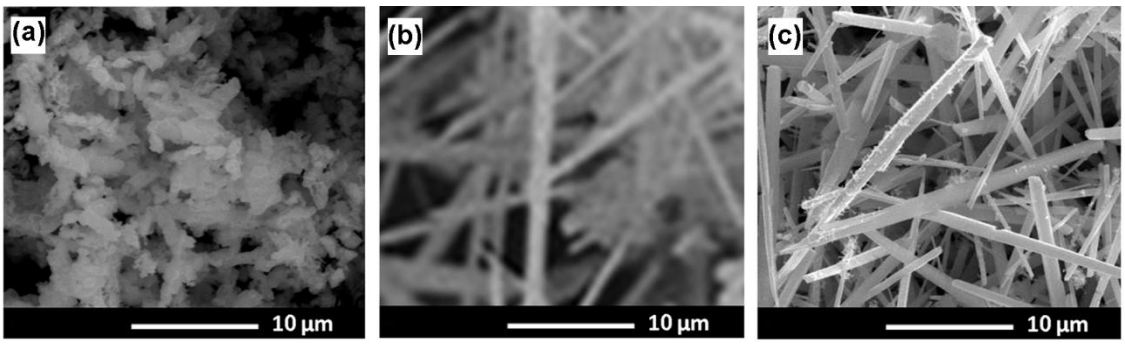

Fig. 2. SEM images of Ga_2O_3 nanoparticles produced with 5 hours (a) and 24 hours (b) hydrothermal process, as well as of GaN nanowires produced from Ga_2O_3 ones (c).

The results of XRD spectroscopy demonstrated the presence of a single β-Ga_2O_3 phase after the hydrothermal process (Fig. 3a), while the diffraction peaks observed in the XRD pattern of the material produced by nitridation correspond to a hexagonal wurtzite GaN structure (Fig. 3b). The XRD pattern indicates on the high crystallinity of GaN nanoparticles with the mean sizes around 30 nm, as deduced from the Sherrer formula. Since the length of GaN nanowires is of several tens of micrometers and their diameter is of (0.5 – 2) μm (see Fig. 2c), one can conclude that the GaN nanowires are composed of smaller crystallites.

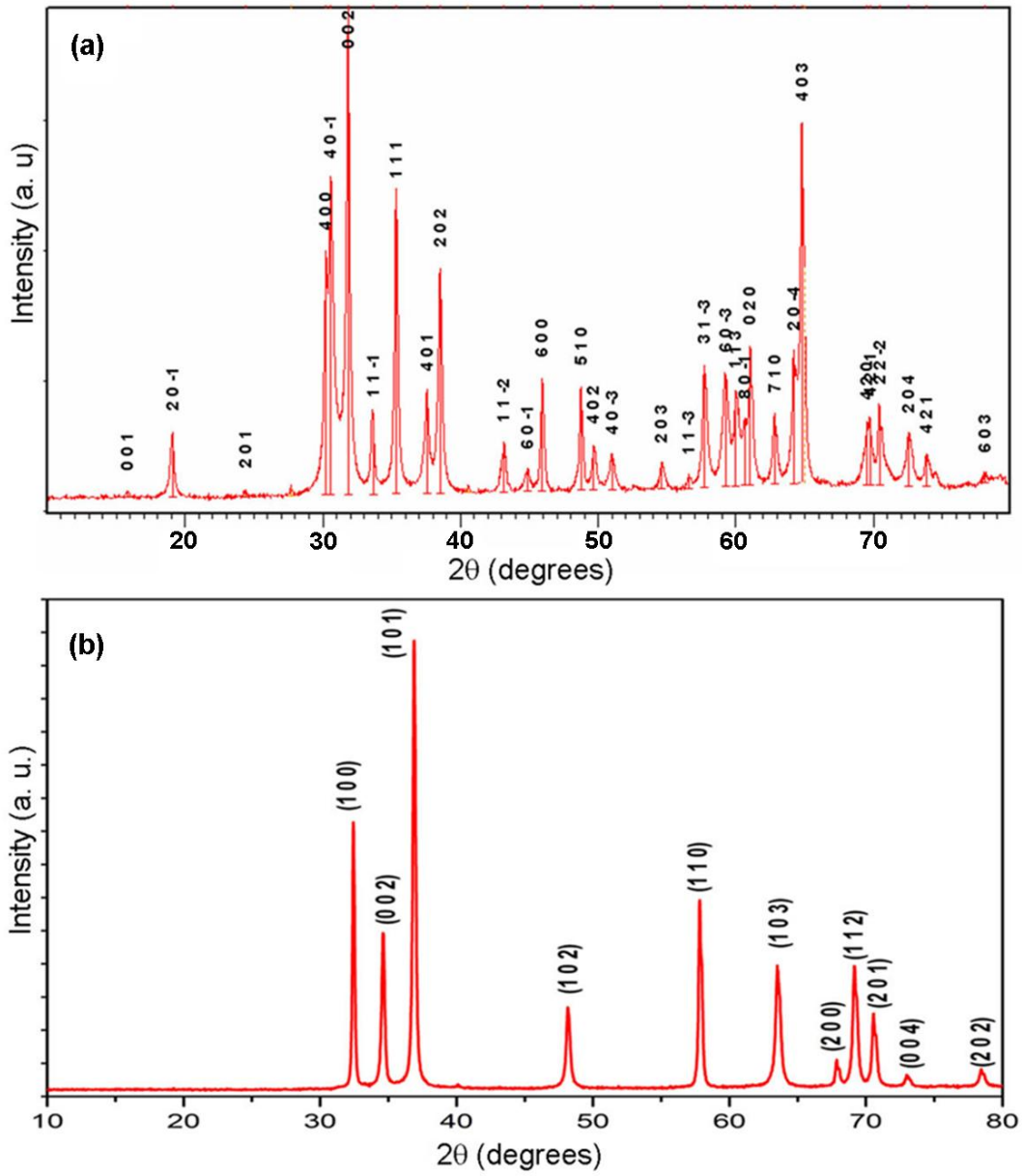

Fig. 3. XRD pattern of Ga_2O_3 nanoparticles obtaining by hydrothermal method (a) and GaN nanowires produces after nitridation (b).

Apart from TiO_2 and ZnO nanoparticles, a derivative composite material was produced according to a technological route with a 3 mM $Zn(NO_3)_2 \cdot 6H_2O$ precursor dissolved in a solution of 3 mM urea. The precipitation of the composite material was performed in a solution of 1M NaOH with the addition of 2 ml of titanium isopropoxide and 10 ml of ethylic alcohol. The obtained suspension was continuously stirred during 1 hour at 65 ^oC. The obtained precipitate was filtered, washed several times in distilled water and ethylic alcohol, dried in an oven at 80 ^oC during 2 hours, and subjected to calcination at 500 ^oC during 4 hours.

Figure 4 presents XRD spectra of the composite material as compared to spectra of pure ZnO and TiO_2 powders. The pattern of the TiO_2 powder is referenced to the anatase structure (00-001-0562 JCPDS card), with peaks at 2Θ equal to 25.5, 37.9, 48.1, 53.9, 55.3, 62.6, 68.8 and 70.5 degrees, corresponding to (101), (004), (200), (105), (211), (204), (116) and (200) reflexes, respectively, while that of the ZnO powder is indexed to a wurtzite structure (01-079-0205 JCPDS card), with peaks at 32, 35, 37, 48, 57, 63, 67, 68, and 69 degrees, correspond to the (100), (002), (101), (102), (110), (103), (200), (112), and (201), reflexes, respectively. All the observed Bragg reflections from the ZnO powder are consistent with Wurtzite's P63mc space group. Diffraction peaks related to both wurtzite ZnO and anatase TiO_2 nanocrystallites appear in the XRD pattern of ZnO/TiO_2 nanocompostes. At the same time, additional peaks associated with the rutile phase of TiO_2 are observed at $2\theta = 35.6$ and 62.0° (JCPDS no. 76- 0324). The sizes of nanoparticles composing the TiO_2 powder are in the range of 10-20 nm according to the Scherrer formula, while those of particles constituting the ZnO powder are in the range of 30-80 nm. Since the sizes of TiO_2 and of ZnO particles deduced from Figs. 1a and 1b are much larger, similarly to GaN nanowires one can conclude that these particles are composed of smaller crystallites.

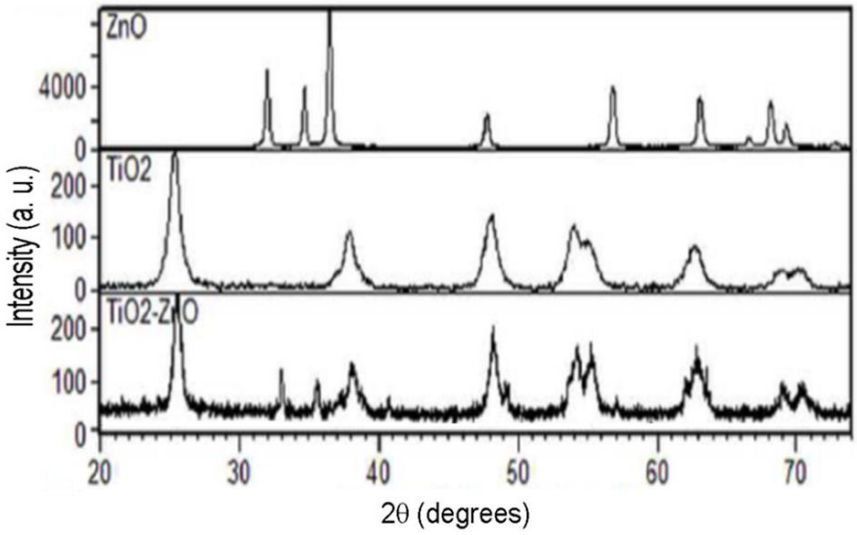

Fig. 4. XRD spectra of ZnO and TiO_2 powders as well as the ZnO/TiO_2 nanocomposite

The formation of β-Ga_2O_3 nanoparticles was also confirmed by the analysis of FTIR spectrum in Fig. 5b. It is known that the metal oxides exhibit absorption bands under 1000 cm^{-1} related to inter-atomic Me-O or Me-O-Me vibrations [27]. The spectrum is dominated by the absorption bands at 455 cm^{-1} and 684 cm^{-1}, previously assigned to vibration modes of the Ga-O bonds in the β-Ga_2O_3 structure (A_u modes) [28], while the other peaks observed at 528 cm^{-1}, 624 cm^{-1}, 748 cm^{-1} have been related to B_u modes. At the same time, no absorption bands related to the Ga_2O_3 phase are observed in the FTIR spectrum of GaN nanowires (Fig. 5a), their spectrum being dominated by two absorption bands at 565 cm^{-1} and 634 cm^{-1}. The first band has been previously attributed to the Ga–N stretching vibration in the hexagonal type GaN crystals (E_1(TO) mode) [29], while the second one may be related to a local vibration mode (LVM) attributed to nitrogen and gallium vacancies.

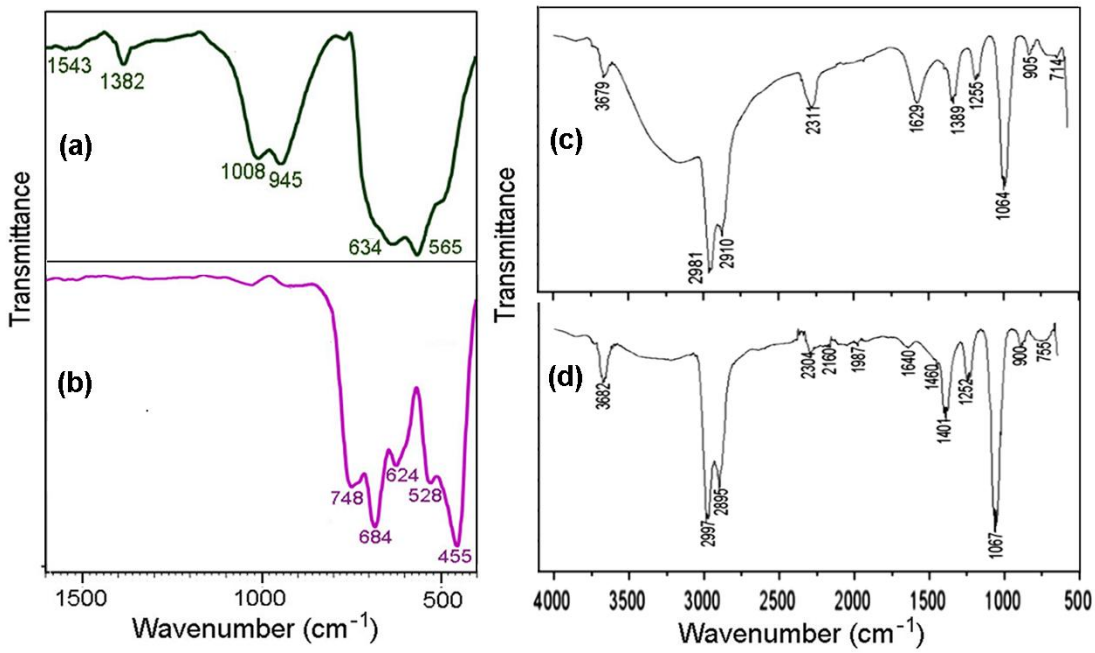

Fig. 5. FTIR spectra of GaN nanowires (a), Ga_2O_3 nanoparticle (b), TiO_2 nanoparticles (c), and TiO_2/ZnO nanocomposite (d).

In addition to Me-O vibrations, absorption band related to bonds involving C atoms in compounds adsorbed at the surface of the prepared oxide nanomaterials have been observed. The vibrations observed at 1067cm^{-1} and 1987 cm^{-1} in the TiO_2/ZnO nanocomposite (Fig. 5d) can be attributed to C=O stretching vibrations in carboxylic acids and other carboxylic compounds present on the nanocomposite surface. The absorption band at 1252 cm^{-1} may be associated with C-O stretching vibrations in alcohols or ethers, while the bands at 1401 and 1460 most probably are related to OH group bending vibrations in alcohols or carboxylic acids. The band at 1640 cm^{-1} can be attributed to C=O bending vibrations. The absorption bands observed at 2160 cm^{-1} and 2304 cm^{-1} in the TiO_2/ZnO nanocomposite, as well as the band observed at 2311 cm^{-1} in TiO_2 nanoparticles can be attributed to stretching vibrations of CO_2 absorbed from atmosphere on the materials surface. The absorption bands observed at 3895 cm^{-1} and 2997 cm^{-1} in the TiO_2/ZnO nanocomposite, as well as the bands observed 2910 cm^{-1} and 2981 cm^{-1} in TiO_2 nanoparticles are usually associated with C-H stretching vibrations in organic compounds, and their exact position depends upon the hybridization state of the carbon. The higher energy bands in the range of 3000 - 3800 cm^{-1}, including the broad bands can be attributed to vibrations of the OH group in water on the metal oxide surface [30].

The prepared nanomaterials are expected to be prospective for photocatalytic, antibacterial and antifungal applications, as well as for biosynthesis of fungal proteases and production of enzyme preparations [31-34]. With the purpose of assessing their prospects in phosphors preparation, they were doped with Eu^{3+} ions, and their luminescence properties have been investigated. For doping Ga_2O_3 nanopowder with Eu^{3+} ions, $EuCl_3$ with concentration from 0.3 to 3 at% was added to the 0.05M $Ga(NO_3)_3$ solution in the hydrothermal synthesis. The pH of the solution was adjusted to the value of 9.5 by adding 25% of NH_4OH under additional stirring for 30 minutes, before introducing the obtained suspension in the autoclave.

The PL spectrum of a Ga_2O_3 nanopowder doped with a 2% concentration of Eu is shown in Fig. 6a. Since the quantum energy of the excitation light with wavelength of 405 nm is lower than the β- Ga_2O_3 bandgap, most probably the luminescence is excited by an intra-central transition in the Eu^{3+} ions, while all the observed emission lines are consistent with the ${}^5D_0 \rightarrow {}^7F_j$ (J = 1,2,3,4) intra-central transitions, where J = 1 is for the PL band at 585 nm, J = 2 is for the lines at 606-818 nm, J = 3 is for lines around 650 nm, and J = 4 is for lines in the spectral range of (680 – 710) nm.

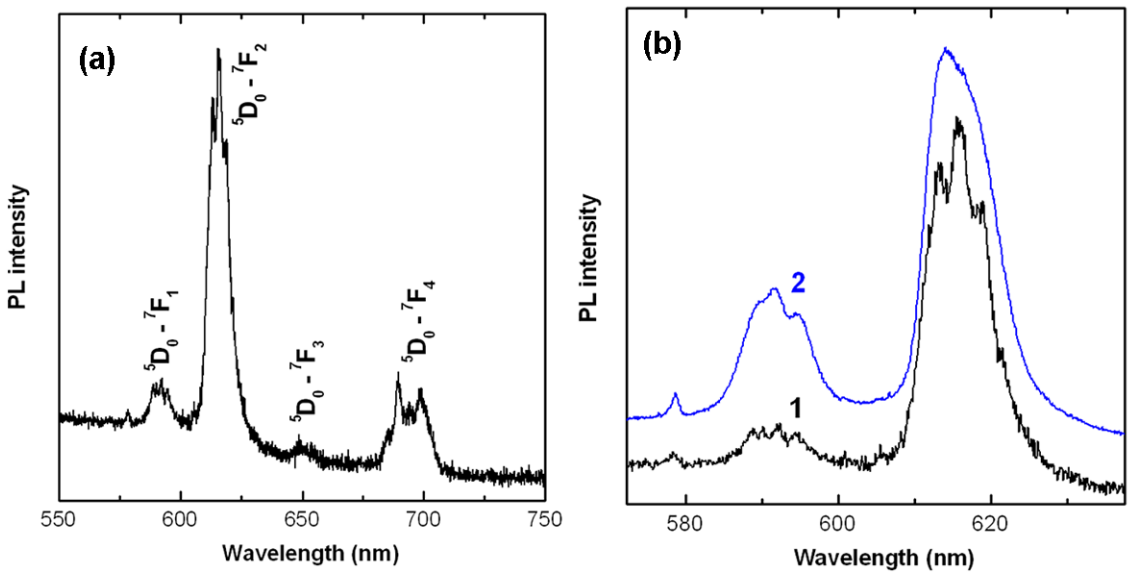

Fig. 6. (a) PL spectrum of Ga_2O_3 nanoparticles doped with Eu^{3+} ions obtaining by hydrothermal method; (b) a comparison of spectra of samples prepared by hydrothermal method (curve 1) and solid phase reactions (curve 2) [35].

The multiplets within these PL bands are determined by the local symmetry of sites where Eu^{3+} ions are incorporated into the β-Ga_2O_3 monoclinic lattice with the space group C2/m. It is supposed that the Eu^{3+} ions occupy the sites of Ga^{3+} ions with either tetrahedral or octahedral crystallographic coordination. Therefore, the local symmetry of Eu^{3+} ions should be T_d or O_h, respectively. However, since the ionic radii of the Ga^{3+} ions are 0.047 nm and 0,062 nm for the tetrahedral and octahedral coordination, respectively [36,37], and the ionic radius of Eu^{3+} ions is 0.095 nm, it is expected that the octahedral site is more suitable for Eu^{3+} ions. On the other hand, the large difference in the ionic radii of Eu^{3+} and Ga^{3+} ions implies that the octahedrons are disported, and the local symmetry of the sites where Eu^{3+} ions are incorporated should be lowered to the C_s symmetry [38]. The incorporation of Eu^{3+} ions in sites with such symmetry was previously confirmed in β-Ga_2O_3 doped with Eu and annealed at 1100 ^oC [39]. The presence of emission lines associated with crystal field levels of Eu^{3+} ions in the spectrum of the sample prepared by hydrothermal synthesis indicates on the good crystalline quality. The advantage of the hydrothermal synthesis over the solid phase reaction method is evidenced from the comparison of the PL spectra of samples prepared by these two technologies (Fig. 6b). One can see that the spectrum of the sample prepared by solid phase reaction is characterized by broader PL bands resulting from superimposing lines, which are usually observed in amorphous materials

and glasses.

The incorporation of Eu^{3+} ions was also demonstrated in the wurtzite lattice of GaN nanowires produced by nitridation of Ga_2O_3 powders prepared by hydrothermal synthesis.

4. Conclusions

The results of this study demonstrated that Ga_2O_3, ZnO, and TiO_2 nanoparticles, as well derivative nanomaterials, including GaN nanowires and ZnO/TiO_2 nanocompostes, with high crystalline quality can be produced by hydrothermal synthesis as a low cost technology. Metal nitrate hydrates and titanium isopropoxide are suitable and accessible precursors for this purpose. The morphology of the produced nanomaterial can be controlled by choosing the duration of the hydrothermal process. The luminescence characterization of Ga_2O_3 nanoparticles doped with Eu^{3+} ions demonstrated efficient incorporation of the Eu^{3+} ions into the β-Ga_2O_3 crystal lattice, therefore opening prospects for the development of nanophosphors on the basis of these nanomaterials.

Acknowledgments. This research was funded by National Agency for Research and Development of Moldova under the Grants #20.80009.5007.02.

References

[1] N. U. Saidin, T. F. Choob, and K. Y. Kokc, IOP Conf. Ser.: Mater. Sci. Eng . 298, 012016 (2018).
[2] M. Rehan, X. Lai, and G. M. Kaleb, CrystEngComm 13, 3725 (2011).
[3] A. I. B. Rovisco, R. Branquinho, J. V. Pinto, R. Martins, E. Fortunato, and P. Barquinha. In *Novel Nanomaterials*, ed. K. Krishnamoorthy, IntechOpen 2021, *C*hapter 1. http://dx.doi.org/10.5772/intechopen.94294
[4] F. Demoisson, R. Piolet, and F. Bernard, Cryst. Growth Des. 14, 5388 (2014).
[5] H. Hayashi and Y. Hakuta, Materials 3, 3794 (2010).
[6] Y. Quan, D. Fang, X. Zhang, S. Liu, and K. Huang, Mater. Chem. Phys. 121 142 (2010).
[7] P Gaffuri, E. Appert, O. Chaix-Pluchery, L. Rapenne, M. Salaün, and V. Consonni, Inorg. Chem. 58, 10269 (2019).
[8] H. Gao, M. Yang, X. Liu, X. Dai, Xi. Q. Bao, and D. Xiong. Frontiers of Optoelectronics 15, 8 (2022).
[9] S. Kim, H. Ryou, I. G. Lee, M. Shin, B. J. Cho, and W. S. Hwang, RSC Adv. 11, 7338 (2021).
[10] H. Ryou, T. H. Yoo, Y. Yoon, I. G. Lee, M. Shin, J. Cho, B. J. Cho, and W. S. Hwang, ECS J. Solid St. Sci. Technol 9, 045009 (2020).
[11] L. S. Reddy, Y. H. Ko, and J. S. Yu, Nanoscale Res. Lett. 10, 364 (2015).
[12] L. Cui, H. Wang, B. Xin, and G. Mao, Appl. Phys. A 123, 634 (2017).
[13] M. Hirano, K. Sakoda, and Y. Hirose, J Sol-Gel Sci Technol 77, 348 (2016).
[14] C. Yilmaz and U. Unal, , Appl. Surf. Sci. 368, 456 (2016).
[15] B. Bulcha, J. L. Tesfaye, D. Anatol, R. Shanmugam, L. Priyanka Dwarampudi, N. Nagaprasad, V. L. Nirmal Bhargavi, and R. Krishnaraj, J. Nanomaterials 2021, 8617290 (2021).
[16] K. Sekar, R. Nakar, J. Bouclé, R. Doineau, K. Nadaud, B. Schmaltz, and G. Poulin-Vittrant.

Nanomaterials 12, 2093 (2022).
[17] S.-P. Hong, J. Park, S. S. M. Bhat, T. H. Lee, S. A. Lee, K. Hong, M.-J. Choi, M. Shokouhimehr, and H. W. Jang, Cryst. Growth Des. 18, 11, 6504 (2018).
[18] S. Dey and S. C. Roy, Nano Ex. 2, 010028 (2021).
[19] B. G. T. Keerthana, T. Solaiyammal, S. Muniyappan, and P. Murugakoothan, Materials Lett. 220, Pages 20 (2018).
[20] E. Y. C. Yan, S. Zakaria, C. H. Chia, AIP Conf. Proc. 1614, 122 (2014).
[21] T. Gupta, Samriti, J. Cho , and J.Prakash, Mater. Today Chem. 20, 100428 (2021).
[22] M. Tang, Y. Xia, D. Yang, J. Liu, X. Zhu, R. Tang, Materials (Basel) 14, 5674 (2021).
[23] A. Morlando, J. McNamara, Y. Rehman, V. Sencadas, P. J. Barker, and K. Konstantinov, J. Mater. Sci. 55, 8095 (2020).
[24] A. Prathan, J. Sanglao, T. Wang, C. Bhoomanee, P. Ruankham, A. Gardchareon, and D. Wongratanaphisan, Sci. Rep. 10, 8065 (2020).
[25] M. A. L. Zavala, S. A. L. Morales, and M. Avila-Santos, Heliyon 3, e00456 (2017).
[26] M. Ramesha, A. Gangadhar, M. Chikkamadaiah, and S. Shivanna, J. Photochem. Photobiol. 6, 100020 (2021).
[27] H. Kumar and R. Rani, Int. Lett. Chem., Phys. Astron. 14, 26 (2013).
[28] L. Mazeina, Y. N. Picard, and S. M. Prokes, Cryst. Growth Des. 9, 1164 (2009).
[29] J. H. Boo, C. Rohr, and W. Ho, J. Crystal Growth 189/190, 439 (1998).
[30] H. Becker, W. Berger, *et.al*., *Chimie organica practica*, Ed. Stiintifica si Enciclopedica, Bucuresti, pp. 114-115, 1982.
[31] E. Rusu, V. Ursaki, S. Raevschi, P. Vlazan, *Proc. SPIE 9258, Advanced Topics in Optoelectronics, Microelectronics, and Nanotechnologies VII*, 92581U (2015), doi: 10.1117/12.2069969.
[32] E. Rusu, V. Ursaki, I. Culeac, S. Raevschi, and P. Vlazan, *5th Int. Conf. Telecommunications, Electronics and Informatics ICTEI 2015*, Chisinau, Moldova, pp. 185 (2015).
[33] E. Rusu, V. Ursaki, T. Gutul, P. Vlazan, and A. Siminel, In: 3rd Int. Conf. Nanotechnol. Biomed. Engineer. IFMBE Proceedings, eds. V. Sontea and I. Tiginyanu, vol 55. pp 93–96, Springer, Singapore (2015) doi.org/10.1007/978-981-287-736-9_22.
[34] P. Vlazan, D. H. Ursu, C. Irina-Moisescu, I. Miron, P. Sfirloaga, and E. Rusu, Mater. Character. 101, 153 (2015).
[35] E. Rusu, V. Ursaki, M. Vasile, and I. Grozescu, J.Optoelectron. Adv. Mater.-Sympozia 1, 59 (2009).
[36] W. Y. Shen, M. L. Pang, J. J. Lin, and J. Fang, J. Electrochem. Soc. 152, H25 (2005).
[37] R. D. Shannon, Acta Crystallogr. Sect. A 32, 751 (1976).
[38] S. Geller, J. Chem. Phys. 33, 676 (1960).
[39] E. Zhu, R. Li, W. Luo, and X. Chen, Phys. Chem. Chem. Phys. 13, 4411 (2011).

GENERATION OF INFRARED RADIATION WITH MODULATED AMPLITUDE AT TERAHERTZ FREQUENCIES

Iurie Nica, Leonid Pogorelischi, Serghei Zavrajnii, and Valeriu Cebotari

Ghitu Institute of Electronic Engineering and Nanotechnologies, str. Academiei 3/3, Chisinau, MD-2028 Republic of Moldova
E–mail: tehmed@nanotech.md

(Received June 28, 2022)

https://doi.org/10.53081/mjps.2022.21-1.07

Abstract

The role of infrared radiation in stimulating cellular metabolism can be dual. Firstly, the energy of light quanta is used by the cell instead of the energy of adenosine triphosphate hydrolysis. Secondly, light absorption cannot replace this hydrolysis. However, it can accelerate its rate and thus the productivity of metabolic reactions associated with it. This process is significantly enhanced by the use of terahertz modulation of infrared radiation, which is manifested, for example, in optically stimulated transport of ions through biological membranes. For therapeutic effects on the above-described processes in biological tissues, a device has been developed that generates infrared radiation with wavelengths in the range of maximum transparency of biological tissues modulated in amplitude in a frequency range of 10^{11}–10^{12} Hz. The modulation of radiation has been produced by the method of interference.

Keywords: cell metabolism, IR radiation, modulation

Rezumat

Rolul radiațiilor infraroșii în stimularea metabolismului celular poate fi dublu. În primul rând, energia cuantelor luminoase este folosită de celulă în locul energiei asociate hidrolizei adenozin trifosfatului. În al doilea rând, absorbția luminii nu poate înlocui această hidroliză; cu toate acestea, poate accelera viteza și astfel și productivitatea reacțiilor metabolice asociate. Acest proces este îmbunătățit semnificativ prin utilizarea modulării la frecvențe terahertz a radiației infraroșii, care se manifestă, de exemplu, în transportul stimulat optic al ionilor prin membranele biologice. Pentru efectele terapeutice asupra proceselor descrise mai sus în țesuturile biologice, a fost dezvoltat un dispozitiv care generează radiații infraroșii cu lungimi de undă în domeniul de transparență maximă a țesuturilor biologice modulate în amplitudine într-un interval de frecvență de 10^{11}–10^{12} Hz. Modularea radiațiilor a fost produsă prin metoda interferenței.

Cuvinte cheie: metabolism cellular, radiație IR, modulație

1. Introduction

The role of infrared radiation in stimulating cellular metabolism can be dual. First, the energy of light quanta is used by the cell instead of the energy of adenosine triphosphate (ATP) hydrolysis. Second, light absorption cannot replace this hydrolysis; however, it can accelerate its flow and thus the flow of metabolic reactions associated with it. It should be noted that this reaction is crucial for the transport of proteins between the membranes inside and outside the cell. Due to the fact that the points at which hydrolysis occurs and at which its energy is consumed are frequently separated by distances significantly exceeding the interatomic distances [1], mediation by linear protein molecules is necessary for an efficient energy transfer along the chains from peptide groups. The energy of these oscillations is 0.21 eV; for their excitation, the energy of ATP hydrolysis is sufficient (0.54 eV). The long lifespan of excitations in this system compared with the duration of their life on an isolated peptide group (10–12 s) is attributed to the formation of solitons—related states of intra peptide oscillations and chain vibrations as a whole. A soliton is a solitary form of a solitary wave propagating along a protein molecule, which is not subject to dispersion and does not lose energy [1]. Solitons can be excited not only chemically, but also optically. These solitons can come to the areas where the energy required for metabolism is consumed and thus increase their intensity. In the spectral range of the excitation of the hydrogen bond (0.165–0.3 eV), which corresponds to the wavelength range of the infrared (IR) range of 4–7.5 μm, there is the oscillation energy of linear molecules. The action of optically induced solitons, which are ideal carriers of the energy of the hydrolysis of ATP molecules along α-helical protein molecules with almost no loss, can be multiplied if the light generating them is modulated in the terahertz range of "shaking" bonds inside the radicals that constitute the protein molecules [2]. In this case, the optical excitation and transport of solitons can stimulate the removal of oxygen-containing radicals trapped in the damaged areas of protein molecules, which is of great importance for practical medicine. It should be noted that optically induced solitons can have a direct effect on the occurrence of ATP hydrolysis. In this case, optical IR radiation leads to the formation of a soliton with a subsequent increase in the probability of the "shooting" of the phosphate group:

ATP + "IR radiation" => ADP + F.

Accordingly, this process is significantly enhanced by the use of terahertz modulation of infrared radiation, which is manifested, for example, in optically stimulated transport of ions through biological membranes in the “potassium–sodium pump” mode [3]. Within the framework of the mechanisms described above, IR radiation can be used to increase the efficiency of oxygen binding in hemoglobin and myoglobin. During the optical IR irradiation of a heme, which is a porphyrin complex of a bivalent iron ion, a soliton is formed, followed by a change in the heme. As a result of this process, an intense capture of the oxygen molecule on the Fe_2 ion is stimulated, which is followed by the destruction of the soliton. Hemoglobin containing oxygen is referred to as oxyhemoglobin. The process of reversible addition of an oxygen molecule to an iron ion in a heme is referred to as oxygenation. This process, as described above, is abruptly enhanced with terahertz modulation of IR radiation, the frequency of which corresponds to the “shaking” of bonds within the porphyrin ring. It should be noted that continuous irradiation using infrared radiation leads to an abrupt increase in the concentration of oxyhemoglobin, the saturation time of which corresponds to the soliton lifetime and can reach 22.5 min. In turn, the releasing of an oxygen molecule is referred to as deoxygenation. It is of interest that the spectral ranges for optimum stimulation of the above-discussed important biochemical reactions by IR radiation correlate well with the positions of IR atmospheric windows in the transmission spectrum of the

Earth's atmosphere (Fig. 1).

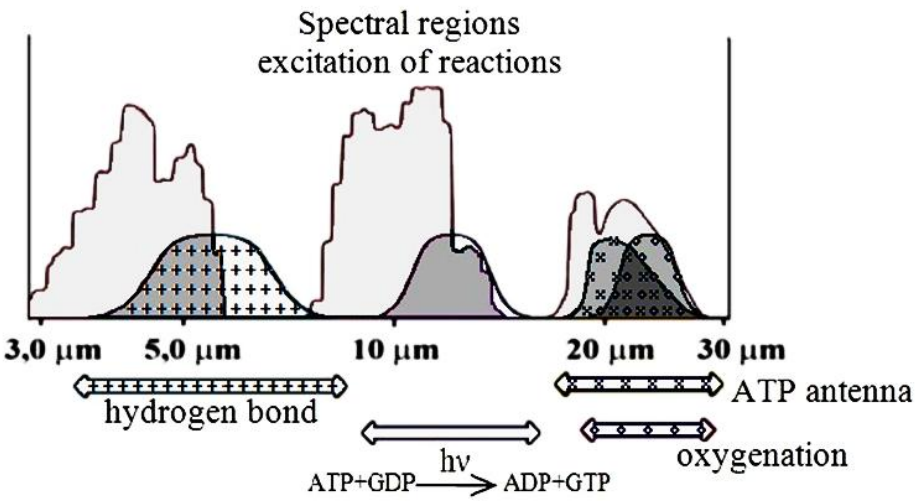

Fig. 1. Optimum excitation spectra of the most important biochemical reactions by IR radiation with terahertz modulation compared with the transmission spectra of atmospheric IR windows in the Earth's atmosphere [4].

For therapeutic initiation of the above-described processes in biological tissues, we have developed a device that generates IR radiation at wavelengths of 0.7–0.9 μm, i.e., in the range of maximum transparency of biological tissues, modulated by amplitude in a frequency range of 10^{13}–10^{14} Hz. The radiation power density of 6 mW/cm^2 is selected on the basis of safety requirements. The total radiation power with a collimator diameter of 50 mm is 100 mW.

Radiation is modulated by the interference method. Unlike the classical interference between two coherent radiation beams, in this device, it was decided to use the interaction of the radiation of two lasers. Therefore, the concept of coherence is not applicable here; the case in hand is a sliding interference pattern. The interference of two beams from ideal lasers should lead to a classical interaction with the release of harmonics referred to as heterodyning. Real lasers, even single-mode ones, emit in a certain frequency range. Therefore, the interference pattern, when they interact, will be a set that includes, in addition to frequencies f_1 and f_2 of both lasers, their half sum f_Σ and half difference f_Δ and frequencies determined by the width of the central modes Δf of each laser.

The amplitude of these frequencies will be significantly less than the amplitude of the half-sum and half-difference; this fact is associated with the shape of the amplitude-frequency characteristic of the radiation in the central mode region.

2. Optical Scheme of the Device

The optical scheme of the device consists of two lasers emitting at a wavelength of λ_1 and λ_2, respectively, and connected to an optical mixer. The result is a combination of the original signals: $f_1 = c / \lambda_1$ and $f_2 = c / \lambda_2$, their half sum is $f_\Sigma = (f_1 + f_2)/2$ and the half difference is $f_\Delta = (f_1 - f_2)/2$. The operating frequencies of the lasers are chosen so that they are suitable; their

half-difference is determined by the frequency of interference (Fig. 2).

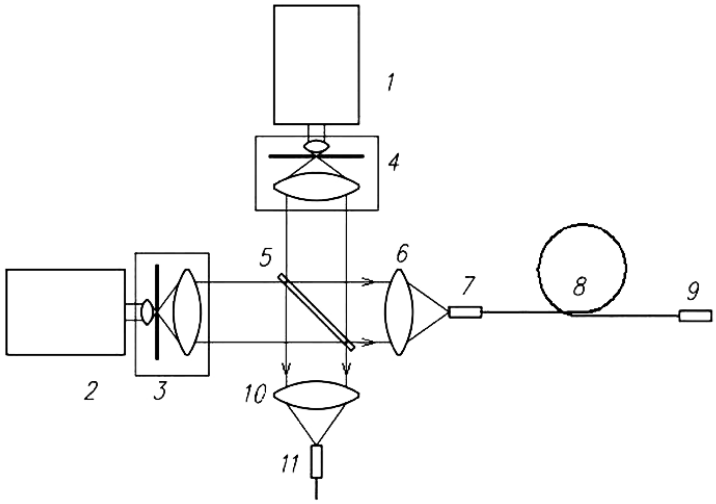

1,2 Laser diodes. 3,4 Beam cleaning systems. 5 Beam splitting plate.
6,10 Lens. 7 Fiber end. 8 Light guide. 9 Collimator. 11 Photosensor.

Fig. 2. Optical scheme of the device

A necessary condition for obtaining high-quality interferences is the equality of the amplitude vectors E_1 and E_2 of both radiations and the coincidence of their polarization planes. To provide this situation, it is necessary to control and stabilize the power of each of the lasers. Thermal stabilization of laser diodes is also required.

However, the cost of single-mode lasers makes the medical device inaccessible to a wide range of users. It is possible to use multimode lasers; however, in this case, the selection of the central mode is necessary. The easiest way to suppress transverse modes is filtering on a small hole. The beam cleaning system (3.4) consists of a micro lens, a pinhole, and a collimating lens.

The point aperture is located at the junction of the foci of both lenses. With the correct adjustment of the diaphragm, the cross section of the beam after the collimating lens is uniformly filled with radiation and has a maximum intensity. The process of adjustment is extremely difficult, especially when working in the IR region, where visual perception does not work. In addition, with uneven heating of the installation, misalignment of the beam cleaning system is possible. To stabilize the operation of the beam cleaning system, a method of auto-adjusting the diaphragm on the feedback signal is applied.

3. Beam Cleaning System

The position of the diaphragm (12) in the plane perpendicular to the beam axis is given by the piezoelectric elements *X* and *Y*, which are supplied with voltage from the controller, which receives the feedback signal from the photodiode (16), which measures the radiation intensity (Fig. 3).

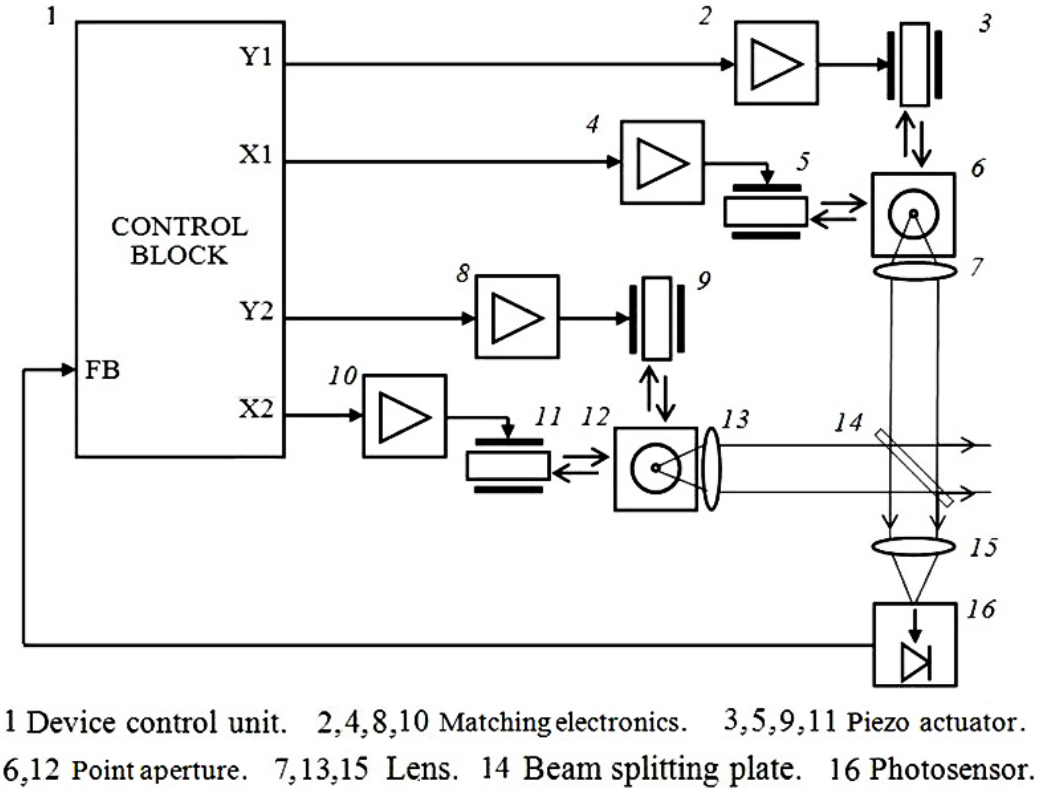

Fig. 3. Beam cleaning system

According to the alignment algorithm, the controller measures the current value of the radiation intensity, then changes the voltage across piezoelectric element *X* and repeats the measurement to find the extremum. After this, the procedure of searching for the maximum is performed with a change in voltage across piezoelectric element *Y*, and finally again across piezoelectric element *X*. This procedure completes the adjustment of the diaphragm (12). Next, the controller repeats the entire alignment cycle for the diaphragm (6). The adjustment of the device is over. To eliminate mutual influence, when adjusting one of the lasers, the other one is turned off for this time. Control adjustment can be carried out periodically without participation of an operator.

4. Design of the Device

The device is made in a 200 × 150 × 80 mm case. The device includes the following units: a 12V-4 A power supply, a control board, a radiator with forced air cooling, a Peltier element, two laser diodes of the brand with λ_1 = 785 nm and λ_2 = 830 nm, a BSW26 mixer (350–1100 nm), a connector for connecting the radiating head, a radiating head with an optical cable, and a collimator (Fig. 4).

The control board contains the following units: two Peltier elements, a temperature controller to stabilize the temperature of the lasers, two laser power stabilizers with the possibility of balancing them, and a timer for a fixed interval of 10 min.

The front panel contains the following units: a power-on indicator, a START/STOP

button, and a "RADIATION" indicator. The front panel contains an optical connector for connecting the radiating head. The rear panel contains a connector for connecting to the network cord. Laser diodes are placed on a Peltier element, which gives heat to a cooled radiator. Laser power is controlled according to classical schemes using photodiodes.

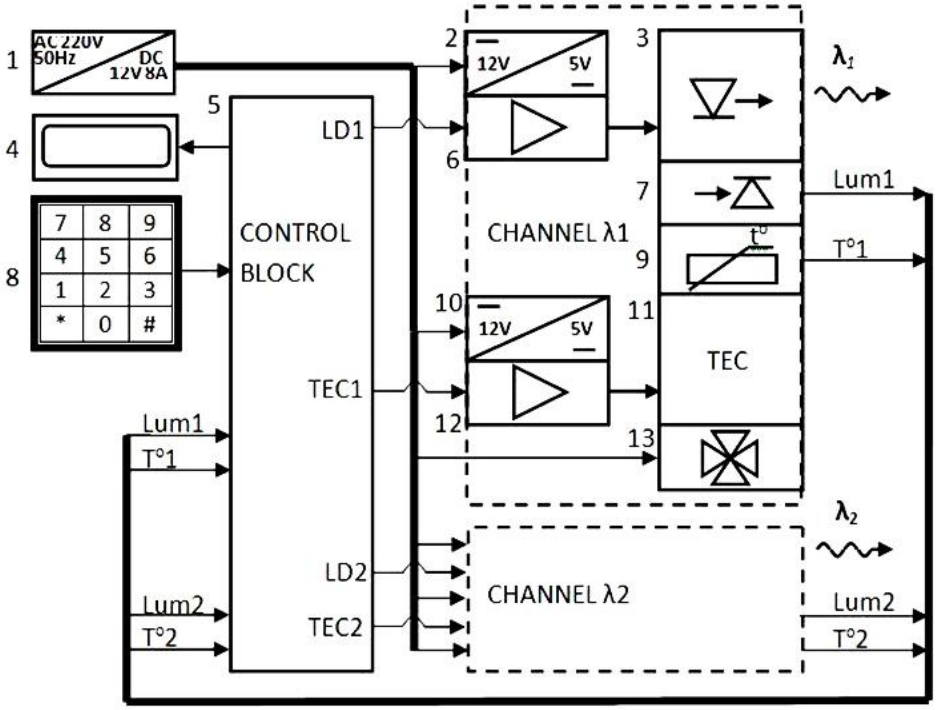

1. AC / DC converter ~220V / 12V. 2, 10. DC / DC converter 12V / 5V. 3. Laser Diode 4. Display. 5. Device control unit. 6. Laser Diode power control circuit output stage. 7. Sensor monitoring the power of the laser diode radiation. 8. Data entry panel. 9. Sensor temperature control laser diode. 11. Peltier element. 12. Peltier element power control circuit output stage. 13. Cooler

Fig. 4. Block diagram of the device

5. Conclusions

A generator of IR radiation packages in the wavelength range of maximum transparency of biological tissues is proposed. The packets follow each other in the range of natural frequencies of oscillations of the cell membranes, cytoskeleton, and cells as a whole. The radiation generated by the generator can affect not only the skin, but also deep structures of the body. However, it, having a powerful regulatory effect on the processes occurring in the body at the molecular, cellular, tissue, organ, and system levels, is not ionizing; that is, it does not cause mutations. The generator is designed for use in medical practice to improve the nervous and humoral regulation of body functions and metabolic processes.

Acknowledgments. This work was supported by the ANCD National Rescerch Program (project no. 20.80009.5007.11).

References

[1] K. Humphreys, J. P. Loughran, M. Gradziel, W. Lanigan, T. Ward, J. A. Murphy, and C. O'Sullivan, in Proc. of 26th Annual Int. Conf. on Engineering in Medicine and Biology Society, 2, 1302 (2004).
[2] R. M. Woodward, B. E. Cole, and M. Pepper, Phys. Med. Biol. 47, 3853 (2002).
[3] B. M. Fischer, M. Walther, and P. Uhd Jepsen, Phys. Med. Biol. 47, 3807 (2002).
[4] B. A. Novikov, N. T. Bagraev, L. E. Klyachkin, and A. M. Malyarenko, Innovatsii 10, 105 (2011).

SURFACE TENSION PROBLEM FOR MICRO- AND NANOWIRES

Serghei A. Baranov[1, 2]

[1]*Institute of Applied Physics, Academiei str. 5, Chisinau, MD-2028 Republic of Moldova*
[2]*Shevchenko Pridnestrov'e State University, str. 25 Oktyabrya 128, Tiraspol, Republic of Moldova*
E-mail: baranov@phys.asm.md

(Received, February, 2022)

https://doi.org/10.53081/mjps.2022.21-1.08

Abstract

An analytical solution for the Gibbs–Tolman–Koenig–Buff equation for microwire and nanowire surfaces has been obtained. Analysis has been performed for a cylindrical surface in terms of the linear and nonlinear Van der Waals theory.

Keywords: Gibbs–Tolman–Koenig–Buff theory, Tolman length, Van der Waals theory

Rezumat

A fost obținută soluția analitică a ecuației Gibbs–Tolman–Koenig–Buff pentru suprafața microfirelor și nanofirelor. Analiza a fost efectuată pentru suprafața cilidrică în cadrul teoriei liniare și neliniare Van der Waals.

Cuvinte cheie: teoria Gibbs–Tolman–Koenig–Buff, lungimea Tolman, teoria Van der Waals

1. Introduction

In this paper, the surface tension in microwires prepared by the Taylor–Ulitovsky method is studied. Surface tension is a fundamental thermodynamic parameter that significantly affects the formation of micro- and nanowires.

The chemical and physical properties of interphase boundaries in micro- and nanowires, as well as for micro- and nanoparticles, have been studied by many authors (see fundamental monographs [1–5], papers [6–20], and reports of S.A. Baranov [21–24]). The following theoretical approaches should be mentioned: the Gibbs–Tolman–Koenig–Buff equation method and the linear and nonlinear Van der Waals theory [22–27].

The study aims at derivation and detailed analysis of expressions for the surface tension of microwires in thermodynamic equilibrium in terms of the Gibbs–Tolman–Koenig–Buff equation method and the Van der Waals theory.

The given theory can find application in microwire production technology.

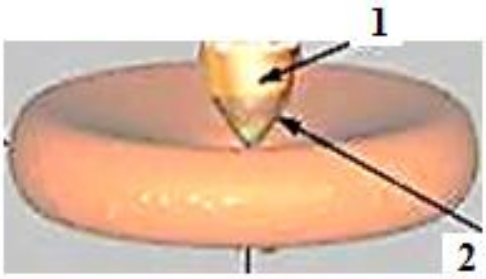

Fig. 1. Process of casting glass-coated amorphous magnetic micro- and nanowires: (*1*) the cylindrical zone and (*2*) the cone zone.

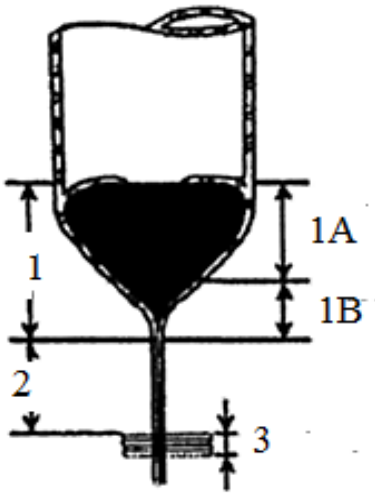

Fig. 2. Schematic micro- and nanowire formation process by the Taylor–Ulitovsky method: (*1*) the microbath: (1A) the primary cone of the microbath and (1B) the secondary cone of the microbath; (*2*) the extension zone; and (*3*) the crystallizer.

It is evident from the figures that cylindrical and conical surfaces should be studied.

2. Modeling of Surface Energy for Microwires in Terms of the Gibbs–Tolman–Konig–Buff Theory

The Gibbs–Tolman–Koenig–Buff differential equation (for a cylinder) [2–6] will be used to describe the surface tensions (σ_i) of micro- and nanowires [1]:

$$\frac{d\ln\sigma_i}{d\ln R_i}=\frac{\frac{2\delta_i}{R_i}+\left(\frac{\delta_i}{R_i}\right)^2}{2+\frac{2\delta_i}{R_i}+\left(\frac{\delta_i}{R_i}\right)^2}, \tag{1}$$

where R_i are the radii of micro- and nanowires (metallic kernel radius R_m or the total radius of glass R_g).

Non-negative parameters (δ_i) characterize the thickness of the interfacial layer (for example, between the glass and the metal).

In surface thermodynamics, Tolman length is used as a parameter that is equal to the distance between the surface of tension and the equimolar surface. The numerical values of the parameter—"Tolman length" analog—for micro and nanowires lie in a range of 0.1–1 μm.

The integral in (1) (if δ_i = const) can be taken exactly. The final result is as follows [11]:

$$\sigma/\sigma^{(\infty)}=\frac{R}{\delta}\sqrt{\frac{2}{2(R/\delta)^2+2R/\delta+1}}\exp\left(-\mathrm{arctg}\left(\frac{1}{1+2R/\delta}\right)\right). \tag{2}$$

The well-known Tolman`s formula (for a cylinder) is in a special case of $R >> \delta$ for formula (2):

$$\sigma/\sigma^{(\infty)}\sim\frac{1}{1+\frac{\delta}{R}}. \tag{3a}$$

In the case of $R << \delta$:

$$\sigma/\sigma^{(\infty)}\sim 0.645(R/\delta). \tag{3b}$$

We get the Rusanov`s linear formula (3b) for the cylindrical surface (see [5, 11]).

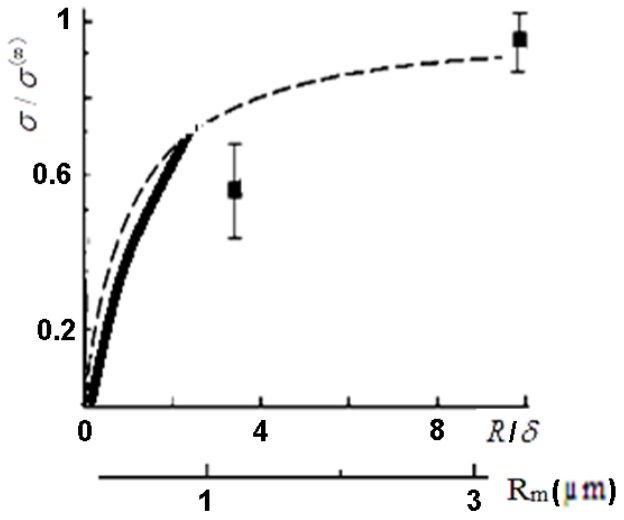

Fig. 3. Function graphs of (dashed line) solutions (3) and (bold line) solutions (10)–(14). Experimental data for the surface tension of metal–glass as a function of metallic kernel radius R_m.

3. Modeling of Surface Energy for Micro- and Nanowires

The basic equation of the linear Van der Waals theory of an inhomogeneous medium (see [1–3, 11, 27] for details) can be written as follows:

$$n'' + \frac{n'}{r} - \frac{1}{\delta^2}(n - n_{1,2}) = 0\,, \tag{4}$$

where n (x) is the function proportional to the volume density $N(x)$ ($x = r/\delta$, n_o = const)**,** r is the radial variable measured from the center of a nanoparticle, and δ is the Tolman length [1–3, 11, 27].

The general solution to Eq. (4) has the form

$$n(r) = n_{1,2} + A I_0(r/\delta) + B K_0(r/\delta)\,, \tag{5}$$

where $I_0(r/\delta), K_0(r/\delta)$ are modified Bessel and Hankel functions.

$$n(0) = n(R) = n_1\,, \quad n(+\infty) = n_2\,. \tag{6}$$

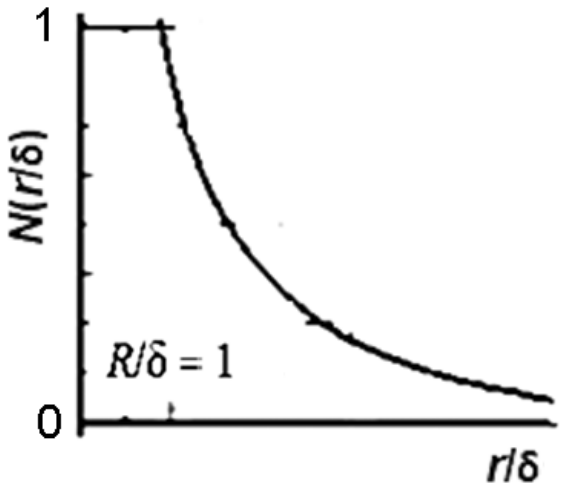

Fig. 4. Function graph of volume density function $N(r/\delta)$ [11, 27].

We will accept for the volume density function $N(r/\delta)$:

$$N(r/\delta) \to n(0) \equiv n(R) = 1\,,\ N\left(+\infty\right) \to n(+\infty) = 0\,. \tag{7}$$

Substituting solution (5) into expression (7) and integrating, we obtain [11, 27]:

$$N(r/\delta)=\begin{cases}1, & r\le R,\\ \dfrac{K_0(r/\delta)}{K_0(R/\delta)}, & r>R,\end{cases} \tag{8}$$

Solution (8) can be used for calculating adsorption, which is defined as the excess number of atoms or molecules in the surface layer of the nanoparticle per unit area:

$$\Gamma \to \delta\,\frac{K_1(x)}{K_0(x_0)}, \tag{9}$$

($x = r/\delta$, $x_0 = R/\delta$).

Taking into account adsorption (9), we obtain the differential equation [11, 27]

$$\frac{d\,\ln\sigma}{d\,\ln x}=\frac{1}{x\{K_0(x)/K_1(x_0)\}+1}. \tag{10}$$

At $x >> 1$

$$\frac{K_0(x)}{K_1(x_0)}\to 1, \tag{11}$$

we obtain

$$\frac{d\,\ln\sigma}{d\,\ln x}=\frac{1}{x+1}, \tag{12}$$

(see Eqs. (2) and (3a));

At $x << 1$

$$\frac{K_0(x)}{K_1(x)}\approx x\ln\frac{2}{\gamma x}, \tag{13}$$

where $\gamma = 1.781$ is the Euler constant, we obtain

$$\frac{d\,\ln\sigma}{d\,\ln x}=\frac{1}{x\ln\dfrac{2}{\gamma x}+1}. \tag{14}$$

This equation is integrated numerically.

4. Modeling of Surface Energy for Micro- and Nanowires in Terms of the Nonlinear Theory

The nonlinear equation can be written as follows [27]:

$$n_1'' + \frac{1}{r}n_1' + \frac{1}{\delta_1^{\,2}}\exp\{-n_1\}=0, \tag{15}$$

Simple volume density function N can be determined as follows [27]:

$$N_1 = 1 + 2\ln[1 - X_1^{\,2}]\,, \tag{16}$$

$$X_1 = \mathrm{r}/(2\sqrt{2}\delta_1)\,. \tag{17}$$

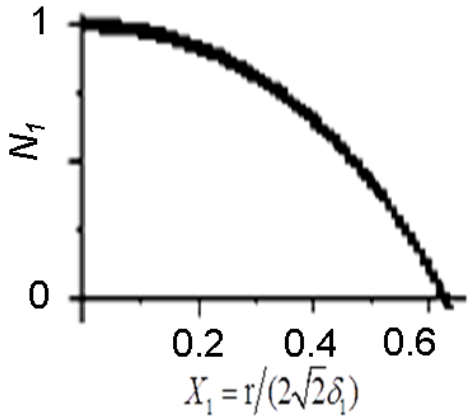

Fig. 5. Function graph of solution (16) [27].

The results obtained have a physical meaning only as long as function N_1 is positive.

The resulting density profile (see Fig. 5 and (16), (17)) significantly differs from the results of the linear theory (see Fig. 4 and (8)) and, therefore, the Gibbs–Tolman–Koenig–Buff theory (see (2), (3a), (3b)).

Micro- and nanowires will be produced with a limited metallic kernel R_{m} [27].

5. Modeling of Surface Energy of Micro- and Nanowires for a Particular Case of the Theory

The equation can be written (for a particular case of the theory) as follows

$$\mathrm{n}_2'' + \frac{1}{r}\mathrm{n}_2' = 0\,. \tag{18}$$

A particular solution to Eq. (18) can have the form

$$n_2 = c\ln(\mathrm{R}/\delta)\,. \tag{19}$$

We will accept the initial values

$$\mathrm{N}_{2,0} = 1\,, \tag{20}$$

and obtain

$$N_2 = 1 + \ln(\mathrm{R}/\delta)\,. \tag{20a}$$

The function graph of N_2 is shown in Fig. 6.

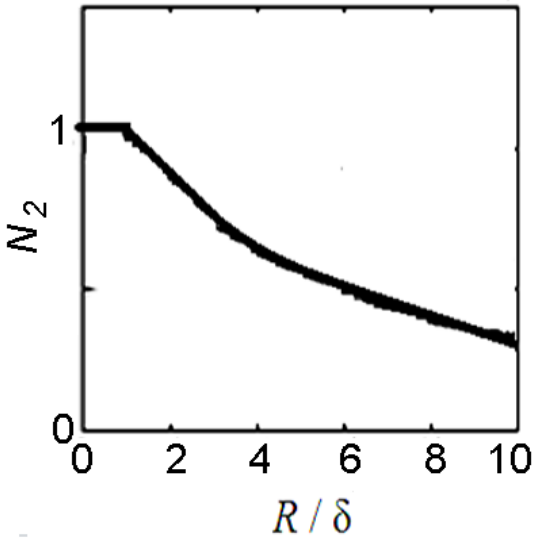

Fig. 6. Function graph of solutions (20) and (20a).

6. Conclusions

A feature of micro- and nanowires is that these objects consist of an amorphous alloy core (metal conductor) with a diameter of 0.1–50 μm, which is covered with a Pyrex-like coating with a thickness of 0.5–20 μm. Therefore, the main technological parameter for the preparation of glass-isolated micro- and nanowires is the surface tension of micro- and nanowires.

According to the previous analysis [1], the geometry of this microwire is most significantly affected by the glass properties. Microwire radius R_g (outer radius of the glass shell) is estimated as follows [1]:

$$Rg \sim \frac{\eta^{2-k}}{V_d^k \sigma_s^{1-k}} \tag{21}$$

where k is a parameter dependent on a casting rate ($0 < k < 1$), V_d is the casting rate, and σ_s is the surface tension.

The metallic radius R_m can be estimated approximately:

$$R_m \sim \frac{\sigma_{sm}}{V_d^{2-k_m}} \tag{22}$$

σ_{sm} is the surface tension of metal–glass($0 < k_m < 1$).

Thus, it has been confirmed that surface tension, which is defined as excess free energy per unit surface area, determines the radius of micro- and nanowires.

Acknowledgments. This work was supported by a Moldavian national project.

References

[1] S. A. Baranov, V. S. Larin, and A. V. Torcunov, Crystals 7, 136 (2017).
[2] S. Ono and S. Kondo, Molecular Theory of Surface Tension in Liquids, in Structure of Liquids, Ser. Encyclopedia of Physics, Springer, Berlin, Heidelberg, vol. 3/10, pp. 134–280, 1960.
[3] J. S. Rowlinson and B. Widom, Molecular Theory of Capillarity, Oxford University Press, Oxford, 1989.
[4] M. J. Jaycock and G. D. Parfitt, Chemistry of Interfaces, Halstead Press, John Wiley & Sons, New York, 1981.
[5] A. I. Rusanov and V. A. Prokhorov, Interfacial Tensiometry, Elsevier, Amsterdam, 1996.
[6] R. C. J. Tolman, Chem. Phys. 17 (3), 333 (1949).
[7] S. Sh. Rekhviashvili and E. V. Kishtikova, Tech. Phys. 56 (1), 143 (2011).
[8] S. Sh. Rekhviashvili, Colloid J. 82 (3), 342 (2020)
[9] A. A. Sokurov, Vestnik KRAUNC, Ser. Fiz.-Mat. Nauk 23 (3), 140 (2018).
[10] S. Sh. Rekhviashvili and A. A. Sokurov, Turk. J. Phys. 42, 699 (2018).
[11] S. Sh. Rekhviashvili, Razmernye yavleniya v fizike kondensirovannogo sostoyaniya i nanotekhnologiakh, Kabardino-Balkarian Sci. Center, Russ. Acad. Sci., Nalchik, 2014.
[12] T. V. Bykov and X. C. Zeng, J. Chem. Phys. 105 (47), 11586 (2001).
[13] I. A. Hadjiagapiou, J. Phys.: Condens. Matter 7, 547 (1995).
[14] V. I. Kalikmanov, J. Chem. Phys. 121, 8916 (2004).
[15] J. W. P. Schmelzer, G. Ropke, and V. B. Priezzhev, Nucleation Theory and Applications, JINR Publishing House, Dubna, 1999.
[16] J. W. P. Schmelzer, V. G. Baidakov, and G. Sh. Boltachev, J. Chem. Phys. 119, 6166 (2003).
[17] V. G. Baidakov and G. Sh. Boltachev, Phys. Rev. E 59 (1), 5648 (1997).
[18] V. G. Baidakov and G. Sh. Boltachev, Phys. Rev. E 59, 469 (1999).
[19] V. G. Baidakov, S. P. Protsenko, G. G. Chernykh, and G. Sh. Boltachev, Phys. Rev. E. 65, 047601 (2002).
[20] P. E. L'vov and V. V. Svetukhin, Phys. Stat. Sol. 57 (6), 1213 (2015).
[21] S. A. Baranov, in Handbook of Nanoelectrochemistry: Electrochemical Synthesis Methods, Properties and Characterization Techniques, Springer, International Publishing, Switzerland, 2015, pp. 1057–1069.
[22] S. A. Baranov, S. Sh. Rekhviashvili, and A. A. Sokurov, Surf. Eng. Appl. Electrochem. 55 (3), 286 (2019).
[23] S. A. Baranov, Surf. Eng. Appl. Electrochem. 53 (2), 124 (2017).
[24] S. A. Baranov, Mold. J. Phys. Sci. 19 (1–2), 182 (2020).
[25] S. A. Baranov, Mold. J. Phys. Sci. 20 (1–2), 44 (2021).
[26] S. A. Baranov, J. Anal. Tech. Res. 3 (2) 28, (2021).
[27] S. A. Baranov, J. Anal. Tech. Res. 3 (2) 39, (2021).